日本磁気学会
ISSN 2432-0250
Journal of the Magnetics Society of Japan
Electronic Journal URL: https://www.jstage.jst.go.jp/browse/msjmag

Vol.42 No.2 2018

Journal

JOURNAL OF THE MAGNETICS SOCIETY OF JAPAN

Vol.42 No.2 2018

日本磁気学会

ISSN 2432-0250

HP: http://www.magnetics.jp/ e-mail: msj@bj.wakwak.com

Electronic Journal: http://www.jstage.jst.go.jp/browse/msjmag

Journal of the Magnetics Society of Japan
Vol. 42, No. 2

Electronic Journal URL: https://www.jstage.jst.go.jp/browse/msjmag

CONTENTS

J. Magn. Soc. Jpn., **42**, 11-14 (2018)

<LETTER>

Basic Study of Electric Field Induced Magnetization Reversal of Multiferroic $(Bi_{1-x}Ba_x)FeO_3$ Thin Films at Room Temperature for Magnetic Recording Technology

S. Yoshimura[1,2], Y. Sugawara[1], G. Egawa[1], and H. Saito[1]

[1]Research Center for Engineering Science, Graduate School of Engineering & Resource Science, Akita University, *1-1 TegataGakuen-machi Akita, Akita 010-8502, Japan*

[2]PRESTO, Japan Science and Technology Agency (JST), *Honcho Kawaguchi, Saitama 332-0012, Japan*

$(Bi_{1-x}Ba_x)FeO_3$ multiferroic thin films with ferromagnetism and ferroelectricity were fabricated and applied to create magnetic recordings using an electric field. The (001)-oriented $(Bi_{1-x}Ba_x)FeO_3$ thin films of which electric polarization direction is perpendicular to the film plane were fabricated onto a non-single-crystalline substrate with a Ta seedlayer / (111)-oriented Pt underlayer at a low substrate temperature of 500 ℃. A very high frequency plasma irradiation was applied during sputtering deposition of $(Bi_{1-x}Ba_x)FeO_3$ to accelerate the crystallization at the low substrate temperature. The fabricated $(Bi_{0.6}Ba_{0.4})FeO_3$ film exhibited hysteresis curves indicating ferromagnetic and ferroelectric behavior. The saturation magnetization of the film was approximately 60 emu/cm^3 and the coercivity was approximately 2.5 kOe, respectively. Magnetic Force Microscopy analysis of the $(Bi_{0.6}Ba_{0.4})FeO_3$ film confirmed that the magnetization was reversed by applying only a local electric field. The multiferroic film described here is expected to be useful for electric field-driven magnetic devices.

Key words: Multiferroic thin film, control of magnetization direction, application of local electric field

1. Introduction

Magnetic recording using an electric field is a promising technology for future recording devices due to its lower power consumption and ease of recording. For example, magnetic field writing in hard disk drives (HDDs) will gradually become more difficult due to increased magnetic field required as the switching field of the bits in order to prevent thermal agitation of the recording media. Recently, energy-assisted magnetic recording technologies for next-generation HDDs, such as thermally-assisted magnetic recording[1] and microwave-assisted magnetic recording[2], have been widely studied in order to decrease the switching field. However, energy-assisted magnetic recording devices consume a large amount of power and the structure of the magnetic field writing head is complex due to the additional elements (a plasmon antenna for thermally-assisted magnetic recording or a spin-torque oscillator for microwave-assisted magnetic recording). On the other hand, electric field writing can be used for HDDs with multiferroic recording media. The power requirement for switching the magnetization direction by this process is very low, the structure of the writing head is simple (involving a needle-shaped conductive element), and a very high electric field can be easily applied to the multiferroic layer because it is thin.

Therefore, the control of magnetization using electric fields is now being widely studied and several techniques have been reported. (1) The magnetoelectric effect has been used on piezoelectric and magnetostrictive laminate composites[3] or multilayer structures[4]. (2) An electric field can be used to control the magnetic anisotropy of a thin metallic magnetic layer in magnetic tunnel junctions with three layers: a thin metallic magnetic layer, a thin insulating layer, and a metallic magnetic layer[5),6]. (3) α-Cr_2O_3 has both dielectric and antiferromagnetic properties so a notable exchange interaction occurs between layers of α-Cr_2O_3 and a ferromagnetic material at room temperature[7] and magnetization switching occurs in the ferromagnetic layer when an electric field is applied due to antiferromagnetic coupling[8]. (4) $BiFeO_3$ is a multiferroic material with a high ferroelectric Curie temperature of 1120 K and a high antiferromagnetic Neel temperature of 640 K. Thus, magnetization switching occurs in ferromagnetic layers fabricated on $BiFeO_3$ layers when an electric field is applied at room temperature due to antiferromagnetic coupling[9),10),11]. (5) $(Dy,Tb)FeO_3$ is a multiferroic material that exhibits ferromagnetism and ferroelectricity and undergoes magnetization switching when an electric field is applied[12].

However, there are problems associated with the application of these systems to magnetic devices. In system (1), rapid operation of magnetization is difficult to achieve due to the use of a mechanical strain on the piezoelectric and magnetostrictive materials. Thus, the application of this system to magnetic devices that require a high-speed operation and high durability will be difficult. In system (2), unique and accurate electric field frequencies and DC magnetic field of several hundred oersteds have to be applied to reverse the magnetization of the thin metallic magnetic layer. Moreover, effective reversal of the magnetization can only be achieved with very thin metallic magnetic layers due to the interface effect between the metallic magnetic layer and the insulating layer. As a result, the application of this system to magnetic devices that

require large magnetization switching and a low error rate without a magnetic field will be difficult. In system (3), the antiferromagnetic Neel temperature of α-Cr_2O_3 is not high (307 K) and not only an electric field but also a magnetic field are needed for magnetization switching. Further, the magnetization reversal can only be achieved with a very thin metallic ferromagnetic layer due to interface effect between the α-Cr_2O_3 and ferromagnetic layer. Therefore, the application of this system to magnetic devices that must withstand high temperatures and require large magnetization switching without a magnetic field will be difficult. In system (4), the exchange interaction between the $BiFeO_3$ and ferromagnetic layer is small so the application of this system to magnetic devices that encounter large external fields and thus require large magnetization switching will be difficult. In system (5), the magnetic Curie temperature of almost multiferroic materials are very low, making the application of this system to practical magnetic devices difficult.

Therefore, a new system that can undergo magnetic switching in a single phase with ferromagnetism and ferroelectricity and with a high Curie temperature is needed for the magnetic recording via electric field writing. Several suitable multiferroic materials with ferromagnetism and ferroelectricity at room temperature, such as $(Bi_{1-x}Ba_x)FeO_3$[13] and $Bi(Fe_{1-x}Co_x)O_3$[14),15], have been reported. In this study, we propose a novel magnetic recording technology based on electric field writing with a $(Bi_{1-x}Ba_x)FeO_3$ thin film that can be used to develop new magnetic recording devices with low power consumption In HDDs with multiferroic recording media, the proposed system offers low power consumption for writing, a simple structure for the writing head, and a very high electric field for writing. The standard fabrication method for multiferroic films is pulsed-laser deposition onto single-crystalline substrates at a high temperature of more than 600℃ [16,17]. However, this method is not suitable for device manufacturing. In this study, we fabricated (001)-oriented $(Bi_{1-x}Ba_x)FeO_3$ thin films onto non-single-crystalline substrates at a relatively low substrate temperature of less than 500℃ by magnetron sputtering. The obtained thin film had electric polarization direction perpendicular to the film plane and was suitable for device applications. Moreover, we demonstrated the control of the magnetization direction on the micrometer scale by applying a local electric field on a scanning probe microscope (SPM) with a Co-Zr-Nb coated conductive tip.

2. Experimental Procedure

Three layers were deposited onto a thermally oxidized Si wafer using a ultra-high-vacuum (UHV) sputtering system: 5 nm Ta, 100 nm Pt, and 100 nm $(Bi_{1-x}Ba_x)FeO_3$, in which the Ba concentration, x, was varied to 0, 0.1, 0.2, and 0.4. The layers were deposited at room temperature, 300 ℃, and 400 - 500 ℃, respectively. The film thicknesses and the deposition temperatures for the Ta seedlayer and Pt underlayer were optimized to obtain strong (111) orientation in the Pt underlayer[18]. Very-high-frequency (VHF) (40.68 MHz) plasma irradiation with an electric power of 5 W was applied during the radio-frequency (RF) (13.56 MHz) sputter deposition of the $(Bi_{1-x}Ba_x)FeO_3$ film; VHF plasma irradiation with a low power density has previously been reported to accelerate the crystallization of the film[19]. The crystallographic orientations and the crystalline structures of the fabricated $(Bi_{1-x}Ba_x)FeO_3$ films were analyzed by X-ray diffraction (XRD). The surface morphology of the $BiFeO_3$ films was examined by SPM with a Si tip. The magnetization curves of $(Bi_{1-x}Ba_x)FeO_3$ films and the Curie temperature T_c of the $(Bi_{0.6}Ba_{0.4})FeO_3$ film were measured using a vibrating sample magnetometer (VSM) with application of a magnetic field perpendicular to the film surface. The ferroelectric hysteresis loops of the $(Bi_{1-x}Ba_x)FeO_3$ films were measured using a ferroelectric tester. The local electric field was applied to the $(Bi_{0.6}Ba_{0.4})FeO_3$ film using an SPM with a conductive, magnetic Co-Zr-Nb tip. The electric and magnetic domain structures of the $(Bi_{0.6}Ba_{0.4})FeO_3$ film were analyzed by electric force microscopy (EFM) and magnetic force microscopy (MFM), respectively, with a conductive, magnetic Co-Zr-Nb tip.

3. Results and Discussions

Fig. 1 shows the XRD profiles of Bi-Fe-O films fabricated with various sputtering conditions on a thermally oxidized Si substrate with a Ta/Pt layer (the XRD profile of Ta/Pt layer is also illustrated). The Pt underlayer was found to have a strong (111) orientation and the full width at half maximum of the rocking curve for the Pt(111) diffraction was 2.0 degrees. The Bi-Fe-O film fabricated on the (111)-oriented Pt underlayer at a substrate temperature of 400℃ was found to have a (001) orientation. Moreover, the Bi-Fe-O film fabricated

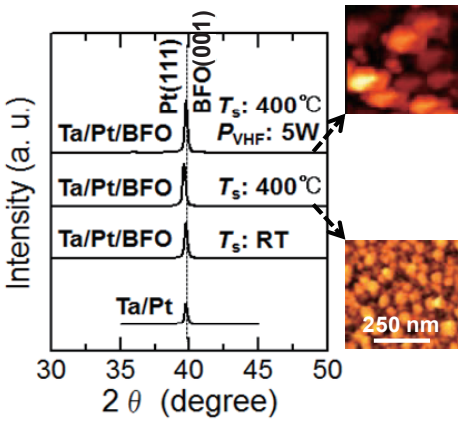

Fig. 1 XRD profiles of Ta seedlayer /Pt underlayer and Bi-Fe-O films on Ta/Pt layer fabricated with various sputtering conditions.

on a (111)-oriented Pt underlayer at a substrate temperature of 400℃ with a VHF plasma irradiation power of 5 W was found to exhibit a strong (001) diffraction peak. The atomic force microscopy (AFM) images of the Bi-Fe-O films are also shown in this figure. The grain size of the Bi-Fe-O film fabricated in the presence of VHF plasma irradiation was found to be larger than that of the Bi-Fe-O film fabricated in the absence of VHF plasma irradiation. These results indicate that the use of a highly-oriented (111) Pt underlayer and VHF plasma irradiation are the key to obtaining strong (001) orientation and crystal grain growth in $BiFeO_3$ thin films at a relatively low substrate temperature.

Fig. 2 depicts the dependence of the saturation magnetization M_s and electric polarization at 750 kV/cm $P_{750kV/cm}$ on the Ba concentration in the (001)-oriented $(Bi_{1-x}Ba_x)FeO_3$ film fabricated on an amorphous Ta seedlayer on a highly (111)-oriented Pt underlayer in the presence of VHF plasma irradiation. The maximum electric field used to measure the electric polarization was 750 kV/cm due to the insulating destruction. The magnetization hysteresis curve (major loop) and the ferroelectric hysteresis curve (minor loop) of the $(Bi_{0.6}Ba_{0.4})FeO_3$ (x=0.4) film are also illustrated in this figure. As the Ba concentration is increased, M_s increased. Based on the clear hysteresis in the magnetization curve and ferroelectric loops of $(Bi_{0.6}Ba_{0.4})FeO_3$ film, the M_s was found to be about 60 emu/cm^3; this is approximately the same as that of $(Bi_{1-x}Ba_x)FeO_3$ films fabricated by pulsed-laser deposition on single-crystalline substrates at a temperature above 600℃. The coercivity H_c of the $(Bi_{0.6}Ba_{0.4})FeO_3$ film was about 2.5 kOe and the squareness ratio M_r/M_s was 0.6. Based on the minor loop of the magnetic hysteresis loop (not shown), the magnetization reversal is thought to be dominated by a nucleation process. The relationship between the magnetic and electric properties will be discussed in a future study because only the minor loop of the electric property was measured here.

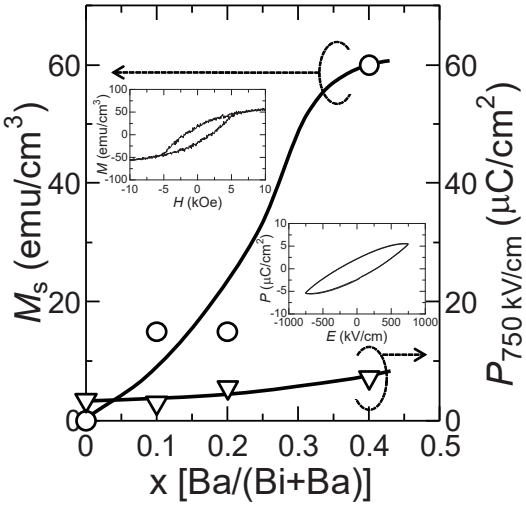

Fig. 2 Dependence of saturation magnetization and electric polarization at 750 kV/cm on Ba concentration for $(Bi_{1-x}Ba_x)FeO_3$ films.

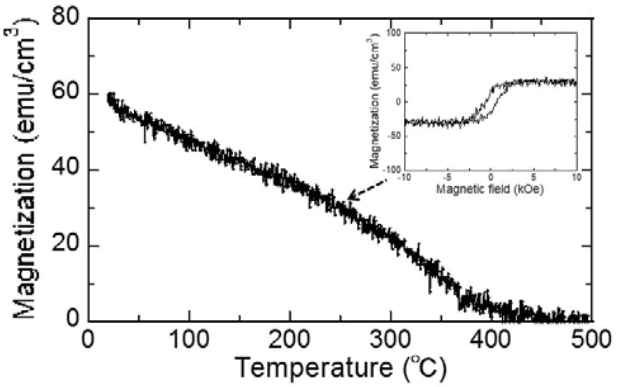

Fig. 3 Dependence of saturation magnetization on measuring temperature and the magnetization curve at the measuring temperature of 250 ℃ for $(Bi_{0.6}Ba_{0.4})FeO_3$ film.

Fig. 3 shows the temperature dependence of M_s and the magnetization curve obtained at a temperature of 250℃ for the $(Bi_{0.6}Ba_{0.4})FeO_3$ film. A clear hysteresis was observed and T_c was estimated to be approximately 400 ℃, which is useful for application to practical magnetic devices.

Figs. 4 (a), (b), and (c) show topographic, EFM, and MFM images, respectively, of the $(Bi_{0.6}Ba_{0.4})FeO_3$ film prior to the application of a DC voltage to the film. The MFM images were captured with a Co-Zr-Nb magnetic tip that was magnetized to saturation at the end of the tip such that the magnetization direction would be perpendicular to the sample surface and the direction of the detected magnetic field from the sample would also be vertical to the sample surface. For the EFM imaging, the Pt underlayer was grounded and a DC voltage of -1.0 V (-100 kV/cm) was applied to the Co-Zr-Nb conductive tip. Because this DC electric field was smaller than the coercive electric field of the $(Bi_{0.6}Ba_{0.4})FeO_3$ film, as depicted in Fig. 2, polarization reversal did not occur during this imaging. The MFM image shows the demagnetized domain structure, and the EFM image shows similar domain structure.

While writing on the $(Bi_{0.6}Ba_{0.4})FeO_3$ film using a local electric field, the surrounding area (3 μm square region) was scanned by the Co-Zr-Nb conductive tip on which a DC voltage of +6.5 V was applied and the center area (1 μm square region) was scanned by the Co-Zr-Nb conductive tip on which a DC voltage of -6.5 V was applied. The DC voltage of ±6.5 V (±650 kV/cm) for the local electric field used for writing was larger than the coercive electric field of the $(Bi_{0.6}Ba_{0.4})FeO_3$ film so it was sufficient to reverse the electric polarization direction of the film. Figs. 4 (d), (e), and (f) show topographic, EFM, and MFM images of the $(Bi_{0.6}Ba_{0.4})FeO_3$ film after a DC voltage of ±6.5 V was applied. In the EFM image obtained with a with the tip voltage of -1.0 V, an attractive force between tip and sample was observed in the center of the ferroelectric

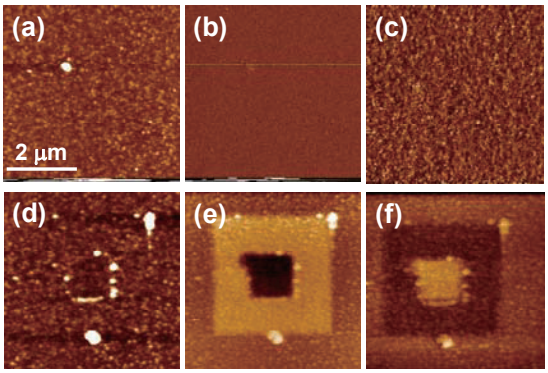

Fig. 4 (a) topographic, (b) EFM, and (c) MFM images of $(Bi_{0.6}Ba_{0.4})FeO_3$ film before applying DC voltage, and (d) topographic, (e) EFM, and (f) MFM images of that film after applying DC voltage.

domain structure, which indicates a positive electric charge in this area. Conversely, in the surrounding area, a repulsive force between tip and sample was seen in the ferroelectric domain structure, indicating a negative electric charge. In an EFM image obtained with a tip voltage of +1.0 V (not shown here), the attractive force and repulsive force in the center area and the surrounding area were reversed. These images show that clear micrometer-scale ferroelectric domains were formed upon application of the local electric field. In the MFM image obtained with the tip magnetized at the end, a repulsive force between the tip and the sample was observed in the center of the ferromagnetic domain structure, indicating that the magnetization direction in this area was upward from the film surface. However, in the surrounding area, an attractive force between the tip and the sample was observed in the ferromagnetic domain structure, indicating that the magnetization direction was downward toward film surface. In an MFM image obtained with a tip voltage of 0 V, the relationship between the attraction and repulsion in the center area and the surrounding area did not change regardless of both before and after EFM measurements with tip voltages of -1.0 V and +1.0 V. Therefore, it can be concluded that micrometer-scale magnetization reversal was achieved by applying a local electric field and that the directions of P and M are parallel. Thus, the proposed multiferroic films are expected to be useful in novel magnetic recording devices driven by electric field writing.

4. Conclusion

In this study, we fabricated $(Bi_{1-x}Ba_x)FeO_3$ multiferroic thin films and demonstrated local magnetization reversal by the application of an electric field. The Ta seedlayer on the (111)-oriented Pt underlayer enabled successful fabrication of (001)-oriented $(Bi_{1-x}Ba_x)FeO_3$ thin films with electric polarization perpendicular to the film plane on a non-single-crystalline substrate. Further, sputtering deposition with VHF plasma irradiation was found to facilitate the crystallization of the $(Bi_{1-x}Ba_x)FeO_3$ thin films at a relatively low substrate temperature (compared to the standard method) of 500 ℃. The $(Bi_{0.6}Ba_{0.4})FeO_3$ film, in which the Ba concentration was optimized, was found to have a high saturation magnetization of about 60 emu/cm^3, a high coercivity of about 2.5 kOe, and a high Curie temperature of about 400℃. MFM images revealed that the magnetization direction in the $(Bi_{0.6}Ba_{0.4})FeO_3$ film could be controlled on a micrometer scale by simply applying an electric field. Based on these results, the proposed multiferroic film is expected to be useful for applications in electric field-driven magnetic devices.

Acknowledgements This work was partially supported by Iketani Science and Technology Foundation, Yazaki Memorial Foundation for Science and Technology, and JST/PRESTO (No. JPMJPR152C, ID: 15655293).

References

1) J. U. Thiele, S. Maat, and E. E. Fullerton: *Appl. Phys. Lett.*, **82**, 2859 (2003).
2) J. G. Zhu, X. Zhu, and Y. Tang: *IEEE Trans. Magn.*, **44**, 125 (2008).
3) J. Ryu, A. V. Carazo, K. Uchino, and H.-E. Kim: *Japanese J. Appl. Phys.*, **40-1-8**, 4948 (2001).
4) G. Srinivasan, E. Rasmussen, J. Gallegos, R. Srinivasan, Y. Bokhan, and V. Laletin: *Phys. Rev. B*, **66**, 029902 (2002).
5) M. Weisheit, S. Fähler, A. Marty, Y. Souche, C. Poinsignon, and D. Givord: *Science*, **315-5810**, 349 (2007).
6) T. Maruyama, Y. Shiota, T. Nozaki, K. Ohta, N. Toda, M. Mizuguchi, A. Tulapurkar, T. Shinjo, M. Shiraishi, S. Mizukami, Y. Ando, and Y. Suzuki: *Nature Nanotechnology* **4**, 158 (2009).
7) Y. Shiratsuchi, T. Fujita, H. Oikawa, H. Noutomi, and R. Nakatani: *Applied Physics Express*, **3-11**, 113001 (2010).
8) T. Ashida, M. Oida, N. Shimomura, T. Nozaki, T. Shibata, and M. Sahashi: *Appl. Phys. Lett.*, **104**, 152409 (2014).
9) X. Qi, H. Kim, and M. G. Blamire: *Philosophical Mag. Lett.*, **87**, 175 (2007).
10) Y. Chu, L. Martin, M. Holcomb, M. Gajek, A. Han, Q. He, N. Balke, C. Yang, D. Lee, W. Hu, Q. Zhan, P. Yang, A. Rodriguez, A. Scol, S. Wang, and R. Ramesh: *Nature Materials*, **7**, 478 (2008).
11) K. Sone, H. Naganuma, M. Ito, T. Miyazaki, T. Nakajima, and S. Okamura: *SCIENTIFIC REPORTS*, **5**, 9348 (2015).
12) Y. Tokunaga, Y. Taguchi, T. Arima, and Y. Tokura: *Nature Physics*, **8**, 838–844 (2012).
13) D. H. Wang, W. C. Goh, M. Ning, and C. K. Ong: *Appl. Phys. Lett.*, **88**, 212907 (2006).
14) D. G. Barrionuevo, S. P. Singh, R. S. Katiyar, and M. S. Tomar: *MRS Proceedings*, **1256** (2010).
15) H. Hojo, R. Kawabe, H. Yamamoto, K. Mibu, and M. Azuma: 1st Seminar of Ferroic-ordering and their manipulation D-1, Campus Innovation Center Tokyo, (2016).
16) G. W. Pabst, L. W. Martin, Y. H. Chu, and R. Ramesh: Appl. Phys. Lett., 90, 072902 (2007).
17) X. Q. Zhao, W. Wang, C. Zheng, Q. X. Zhu, X. M. Li, and R. K. Zheng: *J. Mater. Sci.: Mater. Elec.*, **24**, 1677 (2013).
18) Y. Takeda, S. Yoshimura, M. Takano, H. Asano, and M. Matsui: J. Appl. Phys., 101, 09J514 (2007).
19) S. Yoshimura, H. Kobayashi, G. Egawa, H. Saito, and S. Ishida: J. Appl. Phys., 109, 07B751 (2011).

Received Aug. 08, 2017; Accepted Jan. 18, 2018

J. Magn. Soc. Jpn., **42**, 15-19 (2018)

<Paper>

Writing Field Amplitude in Heat-Assisted Magnetic Recording

T. Kobayashi, Y. Nakatani*, K. Enomoto, and Y. Fujiwara

Graduate School of Engineering, Mie Univ., *1577 Kurimamachiya-cho, Tsu 514-8507, Japan*

*Graduate School of Informatics and Engineering, Univ. of Electro-Communications, *1-5-1 Chofugaoka, Chofu 182-8585, Japan*

We discuss the writing field amplitude in heat-assisted magnetic recording (HAMR) employing a new model calculation. The grain magnetization direction is calculated using the magnetization reversal probability P for each attempt period, whose inverse is the attempt frequency. When the writing field H_w is low, P_- and P_+, where the magnetization and H_w change from antiparallel to parallel and vice versa, respectively, are close. Therefore, there are many grains whose magnetization turns in the direction opposite to the recording direction for a low H_w. The temperature dependence of the attempt frequency is calculated by employing the conventionally used micromagnetic calculation, and the attempt frequency decreases monotonically as the temperature increases and becomes zero at the Curie temperature T_c. Therefore, writing is difficult just below T_c since there is almost no opportunity for writing. Although the coercivity can be reduced by any amount during writing in HAMR, a relatively high writing field is necessary.

Key words: heat-assisted magnetic recording, writing field, grain magnetization reversal probability, attempt frequency, attempt period

1. Introduction

Heat-assisted magnetic recording (HAMR) is a promising candidate for the next generation magnetic recording method beyond the trilemma limit[1]. Since HAMR is a writing method in which the medium is heated to reduce coercivity at the time of writing, the coercivity of the medium can be reduced by any amount. However, micromagnetic simulation has shown that a relatively high writing field is necessary[2].

We have already proposed a new HAMR model calculation[3,4]. The grain magnetization reversal probability and the attempt period, whose inverse is the attempt frequency f_0, are key physical quantities in our new model calculation. We used a fixed f_0 value in our previous model calculation.

In this study, we calculate the temperature dependence of f_0 employing the conventionally used micromagnetic calculation, and then we discuss the writing field amplitude employing our new model calculation in HAMR. It can be explained using the temperature dependences of the grain magnetization reversal probability and the attempt frequency why a relatively high writing field is necessary.

2. Calculation Method

2.1 Calculation conditions

The medium was assumed to be granular. The writing field switching timing and the calculation conditions are summarized in Fig. 1 (a). The mean grain size D_m, the standard deviations of the grain size σ_D/D_m, and the grain height h were 4.9 nm, 10 %, and 8 nm, respectively, and so the grain volume V_m for D_m was $D_m \times D_m \times h$ = 193 nm^3. The bit pitch D_{BP} was 6.8 nm. The Gilbert damping constant α, the Curie temperature T_c, the standard deviation of the Curie temperature σ_{Tc}/T_c, and the anisotropy constant ratio K_u/K_{bulk} of the medium were 0.1, 700 K, 0 %, and 0.4, respectively, where K_u/K_{bulk} is the intrinsic ratio of the medium anisotropy constant K_u to bulk Fe-Pt K_u[5].

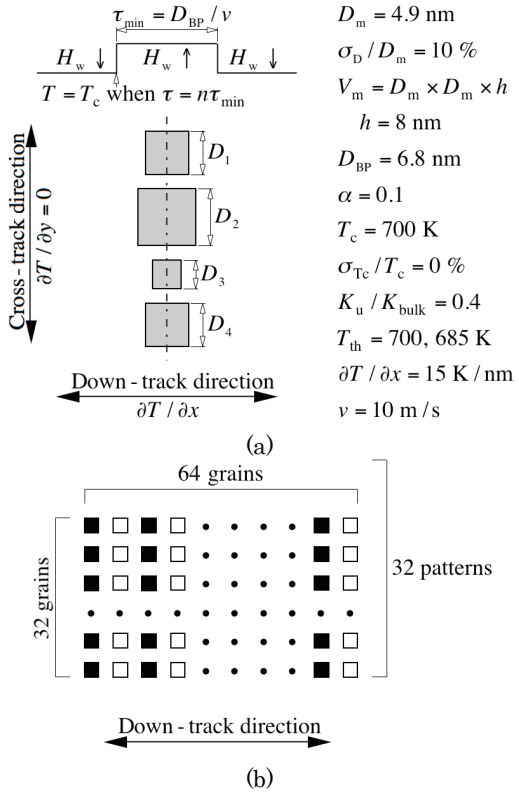

Fig. 1 (a) Writing field switching timing and calculation conditions, and (b) grain arrangement for signal-to-noise ratio calculation.

The writing threshold temperature T_{th} is the calculation starting temperature. The thermal gradient $\partial T/\partial x$ for the down-track direction, the thermal gradient $\partial T/\partial y$ for the cross-track direction, and the linear velocity v were assumed to be 15 K/nm, 0 K/nm, and 10 m/s, respectively.

H_w and $\tau_{min} = D_{BP}/v$ are the writing field and the minimum magnetization transition window, respectively. The H_w direction is upward when time τ is $2n\tau_{min} \le \tau < (2n+1)\tau_{min}$, and downward when $(2n+1)\tau_{min} \le \tau < (2n+2)\tau_{min}$ where n is an integer. There are fluctuations in the switching timing $\Delta\tau$ and position Δx in a granular medium[4]. However, we assumed $\Delta\tau$ = 0 and Δx = 0 in our discussion of the intrinsic phenomenon. When $\tau = n\tau_{min}$, the writing grain temperature T becomes T_c.

Figure 1 (b) shows the grain arrangement for the signal-to-noise ratio (SNR) calculation. We used a pattern of 32 grains for the cross-track direction and 64 grains for the down-track direction, and we used 32 patterns for the SNR calculation. One bit consisted of 32 × 1 grains, namely one column of arranged grains.

2.2 Model calculation

The magnetization M_s direction of the grains was calculated using the magnetization reversal probability P for each attempt period τ_{AP} in our new model calculation[3,4].

The probability P_- for each attempt where M_s and the writing field H_w change from antiparallel to parallel is expressed as

$$P_- = \exp\left(-K_{\beta-}\right). \tag{1}$$

On the other hand,

$$P_+ = \exp\left(-K_{\beta+}\right) \tag{2}$$

is the probability for each attempt where M_s and H_w change from parallel to antiparallel. In these equations,

$$K_{\beta-}(T, H_w) = \frac{K_u(T)V}{kT}\left(1 - \frac{H_w}{H_k(T)}\right)^2 \quad \left(H_w \le H_k(T)\right),$$

$$K_{\beta-}(T, H_w) = 0 \quad \left(H_k(T) < H_w\right), \tag{3}$$

and

$$K_{\beta+}(T, H_w) = \frac{K_u(T)V}{kT}\left(1 + \frac{H_w}{H_k(T)}\right)^2, \tag{4}$$

where K_u, V, k, T, and $H_k = 2K_u/M_s$ are the anisotropy constant, the grain volume, the Boltzmann constant, temperature, and the anisotropy field, respectively.

The temperature dependence of M_s was determined by a mean field analysis[6], and that of K_u was assumed to be proportional to $M_s{}^2$ [7]. T_c can be adjusted by the Cu simple dilution of $(Fe_{0.5}Pt_{0.5})_{1-z}Cu_z$. $M_s(T_c, T)$ is a function of T_c and T, and $M_s(T_c = 770\ \mathrm{K}, T = 300\ \mathrm{K}) = 1000$ emu/cm^3 was assumed. On the other hand, $K_u(T_c, K_u/K_{bulk}, T)$ is a function of T_c, K_u/K_{bulk}, and T, and $K_u(T_c = 770\ \mathrm{K}, K_u/K_{bulk} = 1, T = 300\ \mathrm{K}) = 70$ Merg/cm^3 was assumed. We used $M_s(T_c = 700\ \mathrm{K}, T)$ and $K_u(T_c = 700\ \mathrm{K}, K_u/K_{bulk} = 0.4, T)$ for the calculation in this paper.

The writing field was assumed to be spatially uniform, the direction was perpendicular to the medium plane, and the rise time was zero. Neither the demagnetizing nor the magnetostatic fields were considered during writing since they are negligibly small. The output signal, media noise, and media signal-to-noise ratio (SNR) were calculated using the sensitivity function[8] of a magnetoresistive head with an element width of 218 nm, a shield-to-shield distance of 15 nm, and a 4.0 nm head-medium spacing. The element width is the same as the cross-track width of the simulation region.

The calculation procedure is described below. First, the medium was determined by T_c and K_u/K_{bulk}. The grain temperature fell from T_c according to the thermal gradient $\partial T/\partial x$ for the down-track direction and according to v during the writing process. The magnetic property and then $P_\pm$ were calculated by undertaking a mean field analysis for each τ_{AP}. The magnetization direction can be determined by the Monte Carlo method for each τ_{AP}. The SNR was obtained from the magnetization patterns as shown in Fig. 1 (b).

2.3 Micromagnetic calculation

We calculated the temperature dependence of the attempt frequency f_0, whose inverse is the attempt period $\tau_{AP} = 1/f_0$, employing a conventional micromagnetic calculation using the Landau-Lifshitz-Gilbert (LLG) equation[9] where we calculated the temperature dependence of the magnetic properties used in the calculation with a mean field analysis.

We also calculated the SNR employing the micromagnetic calculation, and compared the results with those obtained using our model calculation. The calculation conditions for the model calculation and the micromagnetic calculation were the same.

3. Calculation Results

3.1 Grain magnetization reversal probability

The grain magnetization reversal probability $P_\pm$ is a function of the anisotropy constant K_u and the anisotropy field H_k as shown in Eqs. (3) and (4). Figure 2 shows the temperature dependence of (a) K_u and (b) normalized $H_k/H_k(300\ \mathrm{K})$. The solid lines are calculated using a mean field analysis and the filled circles are the experimental results for Fe-Pt film[7]. T_c = 770 K is used instead of 700 K to compare with the experimental results. The experimental results can be represented using a mean field analysis. However, if T_c

is low, for example 580 K, the temperature dependence of the experimental H_k values of Fe-Ni-Pt film[7] cannot be represented by a mean field analysis[10]. Since the T_c of 700 K used in this paper is sufficiently high, the use of a mean field analysis is valid.

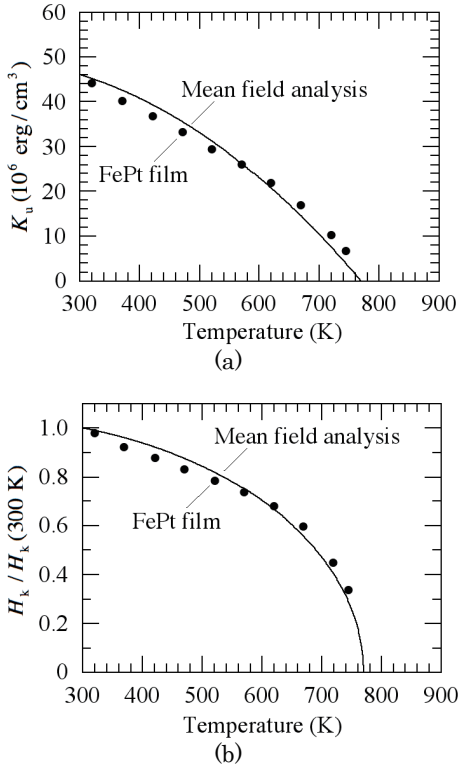

Fig. 2 Temperature dependence of (a) anisotropy constant K_u and (b) normalized anisotropy field $H_k / H_k(300\ \mathrm{K})$ where the solid lines are calculated by a mean field analysis and the filled circles are experimental results for Fe-Pt film[7].

3.2 Attempt frequency

Next, we calculated the temperature dependence of the attempt frequency f_0 for media with α = 1 instead of 0.1, T_c = 700 K, and K_u / K_{bulk} = 0.4 since α = 0.1 is too small to calculate in a short time when employing the micromagnetic calculation. Figure 3 (a) shows the result using filled circles for the grain volume $V = V_m = D_m \times D_m \times h$ = 193 nm^3. Since V = 193 nm^3 is also too large to calculate, the f_0 values for $V = 0.8D_m \times 0.8D_m \times 0.8h$ = 99.0 nm^3 and $V = 0.6D_m \times 0.6D_m \times 0.6h$ = 41.8 nm^3 were also calculated as shown in Figs. 3 (b) and (c), respectively. These results can be fitted using

$$f_0(T) = \frac{2\alpha}{1+\alpha^2} f_1 \sqrt{\frac{V}{V_m}} \sqrt{\frac{600}{T}} \frac{K_u(T)}{K_u(600\ \mathrm{K})} \quad (5)$$

in consideration of a reference 11) where $f_1 = 500 \times 10^9$ s^{-1} and $K_u(600\ \mathrm{K})$ = 8.0 Merg/cm^3.

Since f_0 decreases monotonically as the temperature increases, and becomes zero at T_c, writing in HAMR is difficult just below T_c since there is almost no opportunity for writing.

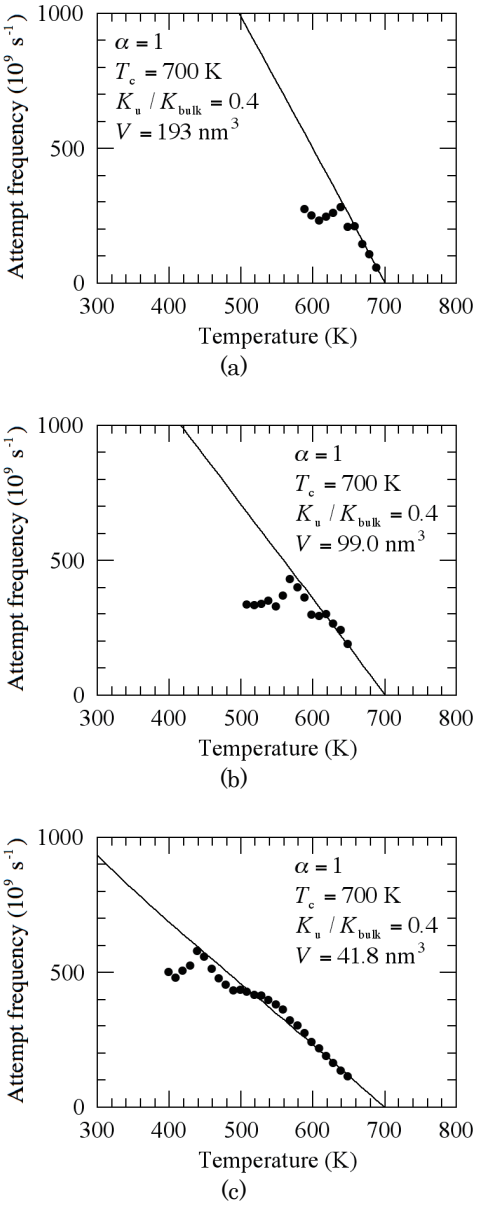

Fig. 3 Temperature dependence of attempt frequency for (a) grain volumes V of 193 nm^3, (b) 99.0 nm^3, and (c) 41.8 nm^3.

3.3 Signal-to-noise ratio

Figure 4 shows the time dependence of the grain magnetization reversal probability. Solid lines show the probabilities, and filled circles indicate calculation timings for each attempt period τ_{AP}. The minimum magnetization transition window $\tau_{min} = D_{BP} / v$ is 0.68 ns. In this paper, a fixed f_0 value of 50×10^9 s^{-1} is used for α = 0.1, $V = V_m$ = 193 nm^3, and T = 650 K. The temperature of 650 K corresponds to time τ = 0.33 ns. Then, $\tau_{AP} = 1 / f_0$ becomes 0.020 ns. Figure 4 (a) also shows the time dependence of the anisotropy field H_k. Since the H_k value exceeds 10 kOe within 0.1 ns, the recording time is estimated to be of the order of 0.1 ns under the conditions used here.

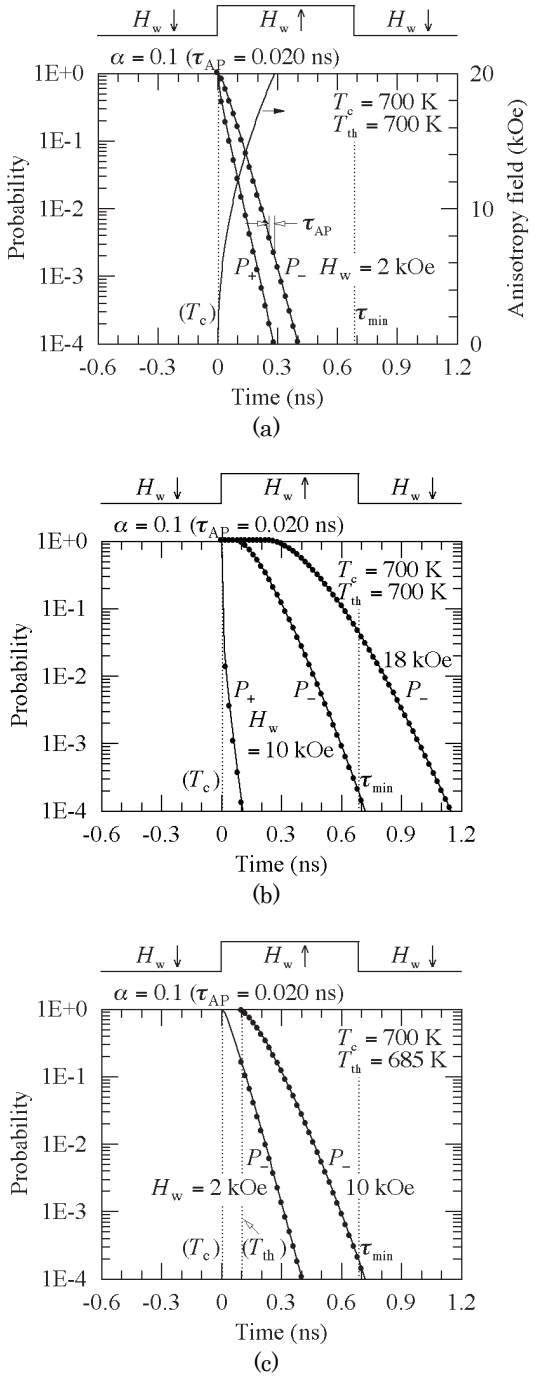

Fig. 4 Time dependence of grain magnetization reversal probability $P_{\pm}$ for (a) Curie temperature T_c = 700K, writing threshold temperature T_{th} = 700K, and writing field H_w = 2 kOe, (b) T_c = T_{th} = 700K, and H_w = 10, 18 kOe, (c) T_c = 700K, T_{th} = 685 K, and H_w = 2, 10 kOe where the filled circles indicate calculation timings.

When the Curie temperature T_c, the writing threshold temperature T_{th}, and the writing field H_w were 700 K, 700K, and 2 kOe, respectively, the probability P_- where the magnetization M_s and H_w changed from antiparallel to parallel and P_+ from parallel to antiparallel were close as shown in Fig. 4 (a). T_{th} = T_c means that the model calculation starts at 0 ns, and the filled circles are plotted from 0 ns since we assumed that the grain temperature becomes T_c at 0 ns. Since the switching probability from the recording direction to the opposite direction was not sufficiently low, there are many grains whose magnetization turned in the direction opposite to the recording direction for a low H_w.

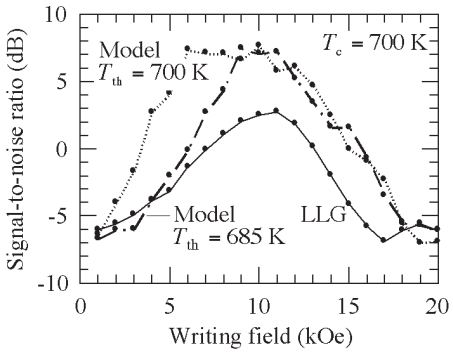

Fig. 5 Dependence of signal-to-noise ratio on writing field for LLG calculation and model calculation with writing threshold temperatures T_{th} of 700 and 685 K.

The dependence of the signal-to-noise ratio (SNR) on H_w employing the model calculation is shown in Fig. 5. As expected, the SNR indicated by Model of T_{th} = 700 K was low at H_w = 2 kOe, and an H_w of 5 or 6 kOe is necessary for a high SNR.

On the other hand, when H_w = 10 kOe, P_+ was sufficiently low and P_- was sufficiently high during writing as shown in Fig. 4 (b). Therefore, the SNR indicated by Model of T_{th} = 700 K was high at H_w = 10 kOe as shown in Fig. 5.

In Fig. 5, the SNR decreases as H_w increases when H_w > 10 kOe, and this phenomenon is caused by erasure-after-write (EAW)[3]. EAW occurred after writing ($\tau \geq \tau_{min}$), and the grain magnetization reversed in the opposite direction to the recording direction when we changed the H_w direction at τ_{min} since P_- for $\tau \geq \tau_{min}$ was not sufficiently low, for example, P_- for H_w = 18 kOe as shown in Fig. 4 (b).

The model calculation (Model of T_{th} = 700 K) and the micromagnetic calculation (LLG) are compared in Fig. 5. The SNR values are almost the same for H_w > 10 kOe. However, the SNR of the model calculation is somewhat higher than that of the LLG calculation for H_w < 10 kOe. As mentioned above, f_0 was low, and so writing was difficult just below T_c, that is, just after 0 ns. Therefore, we examined the SNR for T_{th} = 685 K instead of 700 K where the model calculation starts at 685 K. τ_{AP} was about 0.07 ns at 685 K from Fig. 3 (a). The temperature of 685 K corresponded to τ = 0.1 ns, and the model calculation started at τ = 0.1 ns as shown in Fig. 4 (c). The filled circles are plotted from 0.1 ns as shown in Fig. 4 (c). The result of the SNR indicated by Model of T_{th} = 685 K is also shown in Fig. 5. The SNR values were almost the same for LLG, Model of T_{th} = 700 K, and 685 K when H_w > 10 kOe

since EAW for H_w > 10 kOe is determined by P_- after τ_{min}. On the other hand, in the H_w < 10 kOe range, the SNR value for Model of T_{th} = 685 K was almost the same as that for LLG. Therefore, it is reasonable that writing is difficult just below T_c.

4. Conclusions

We considered the writing field amplitude in heat-assisted magnetic recording (HAMR) employing our new model calculation.

(1) When the writing field is low, the grain magnetization reversal probability from the recording direction to the opposite direction is not sufficiently low during writing. There are many grains whose magnetization turns in the direction opposite to the recording direction, and the signal-to-noise ratio is low.

(2) The attempt frequency is low, and then writing is difficult just below the Curie temperature since there is almost no opportunity for writing.

Therefore, although the coercivity of the medium can be reduced by any amount during writing in HAMR, a relatively high writing field is necessary.

When the damping constant α is 0.1, the writing field of about 10 kOe is necessary. The writing field for α = 0.01 will be published elsewhere.

Acknowledgements We acknowledge the support of the Advanced Storage Research Consortium (ASRC), Japan.

References

1) S. H. Charap, P. -L. Lu, and Y. He: *IEEE Trans. Magn.*, **33**, 978 (1997).
2) J. -G. Zhu and H. Li: *IEEE Trans. Magn.*, **49**, 765 (2013).
3) T. Kobayashi, F. Inukai, K. Enomoto, and Y. Fujiwara: *J. Magn. Soc. Jpn.*, **41**, 1 (2017).
4) T. Kobayashi, Y. Nakatani, F. Inukai, K. Enomoto, and Y. Fujiwara: *J. Magn. Soc. Jpn.*, **41**, 52 (2017).
5) T. Kobayashi, Y. Isowaki, and Y. Fujiwara: *J. Magn. Soc. Jpn.*, **39**, 8 (2015).
6) M. Mansuripur, and M. F. Ruane: *IEEE Trans. Magn.*, **MAG-22**, 33 (1986).
7) J. -U. Thiele, K. R. Coffey, M. F. Toney, J. A. Hedstrom, and A. J. Kellock: *J. Appl. Phys.*, **91**, 6595 (2002).
8) Y. Kanai, Y. Jinbo, T. Tsukamoto, S. J. Greaves, K. Yoshida, and H. Muraoka: *IEEE. Trans. Magn.*, **46**, 715 (2010).
9) Y. Nakatani, Y. Uesaka, N. Hayashi, and H. Fukushima: *J. Magn. Magn. Mat.*, **168**, 347 (1997).
10) T. Kobayashi, Y. Isowaki, and Y. Fujiwara: *J. Magn. Soc. Jpn.*, **40**, 28 (2016).
11) E. D. Boerner and H. N. Bertram: *IEEE Trans. Magn.*, **34**, 1678 (1998).

Received Aug. 24, 2017; Revised Oct. 16, 2017; Accepted Jan. 5, 2018

J. Magn. Soc. Jpn., **42**, 20-23 (2018)

<LETTER>

Relationship between bulk coercivity and coercivity of surface layer in Nd-Fe-B-based sintered magnet

T. Maki, R. Ishii, M. Natsumeda, and T. Nishiuchi

Magnetic Materials Research Laboratory, Magnetic Materials Company, Hitachi Metals, Ltd., *2-15-17 Egawa, Shimamoto-cho, Mishima-gun, Osaka 618-0013, Japan*

The bulk coercivity and coercivity of the polished surface layer of a Nd-Fe-B-based sintered magnet were measured systematically in order to discuss the effectiveness of observing the magnetic domain on the surface of the magnet. It was revealed that the bulk coercivity and coercivity of the polished surface layer were in a proportional relationship even though the coercivity of the surface layer was much smaller than the bulk coercivity. This suggests that the magnetization reversal that occurred in the surface layer has a mechanism similar to that inside of the magnet. The relationship between the bulk coercivity and coercivity of the surface layer was not proportional when the degree of alignment decreased, which can be explained by the increase in the local demagnetizing field on the surface of the magnet.

Key words: Nd-Fe-B magnet, coercivity, surface layer, degree of alignment, demagnetizing field

1. Introduction

The coercivity of a Nd-Fe-B-based magnet is an important property, especially for high temperature use, and partially substituting Nd with heavy rare earth elements such as Dy and Tb is an effective way to improve the coercivity. However, decrease in the usage of Dy and Tb has been required recently because of their limited production. The coercivity of a Nd-Fe-B -based magnet is greatly changed not only by the addition of Dy and Tb but also by the microstructure. To understand directly the relationship between the microstructure and magnetic domain structure in the magnet, several methods for evaluating the magnetic domain structure on the surface of the magnet are studied, such as the magneto-optical Kerr microscope[1, 2], magnetic force microscope (MFM)[3, 4] and spin-polarized scanning electron microscope (spin-SEM)[5, 6]. However, on a polished surface of a Nd-Fe-B-based magnet, magnetization reversal progresses with a clearly smaller magnetic field than the bulk coercivity. For this reason, a method for suppressing the reduction in surface coercivity was studied recently by using fractured surface[7]. If we could identify the similarities and differences in the magnetic reversal process between the surface and inside of a magnet, it would be very useful for discussing the coercivity. In this study, to clarify the correlation between the surface and inside of the Nd-Fe-B-based sintered magnet, the bulk coercivity and coercivity of the polished surface layer were measured, and the influence of the Dy content, annealing condition, and degree of alignment on these coercivities was investigated.

2. Experimental method

Highly aligned (HA) and moderately aligned (MA) sintered magnets that had compositions of (30.2-x)Nd-xDy-67.6Fe-1.0B-0.9Co-0.1Al-0.1Cu-0.1Ga (mass%) (x = 0, 1.0, 2.0, 5.0) were prepared by using an ordinary process except for pressing, which applied a different magnitude of magnetic field. Degree of alignment α was defined as the following formula[8, 9],

$$\alpha = B_r / J_s \quad (1)$$

where B_r and J_s are the remanence and saturation magnetization of each sample. For example, the degree of alignment of HA and MA magnets for x = 0 was α = 0.97 and 0.90, respectively. The annealing temperature after sintering was changed from 460 to 540°C. Each sample was set to 7 × 7 × 7 mm under the same grinding condition by using a surface grinder and the demagnetization curve was measured by using a BH tracer. The coercivity of the surface layer was obtained from the differential value of the step appearing in the second quadrant of the demagnetization curve, as shown in Fig. 1. It is supposed that this step in the demagnetization curve is derived from a-b planes:

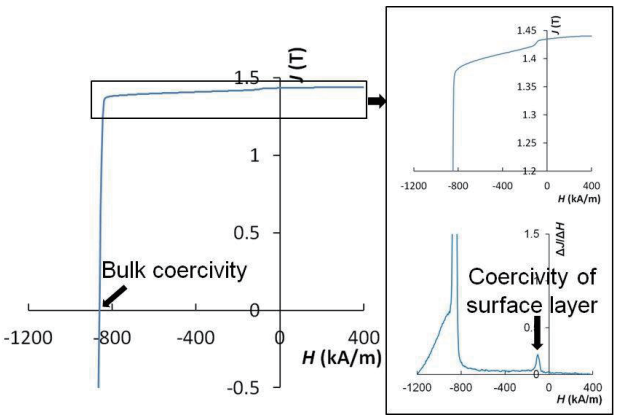

Fig. 1 Illustration of bulk coercivity and coercivity of surface layer.

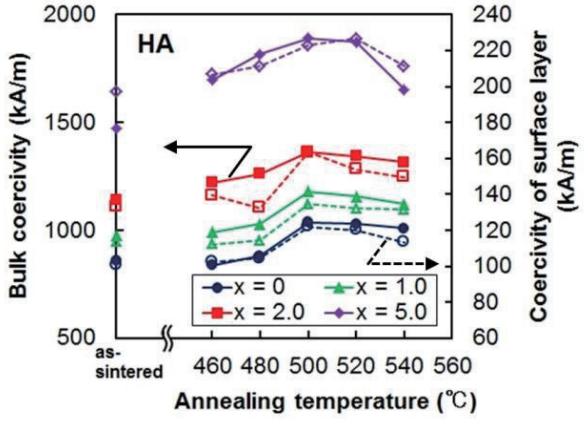

Fig. 2 Bulk coercivity and coercivity of surface layer of highly aligned (HA) magnets when changing annealing temperature. Solid lines are bulk coercivity and dashed lines are coercivity of surface layer.

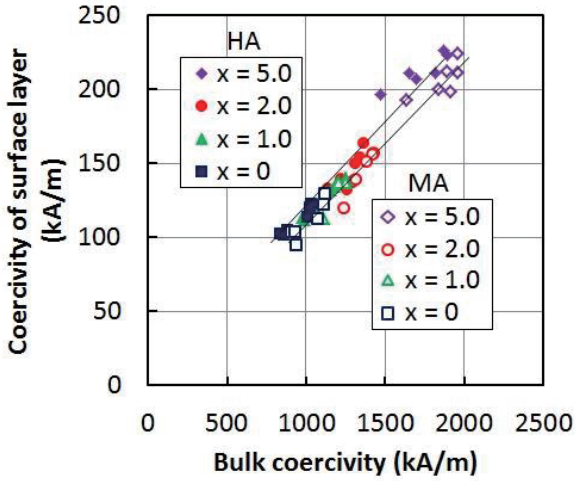

Fig. 3 Relationships between bulk coercivity and coercivity of surface layer of highly aligned (HA) and moderately aligned (MA) magnets.

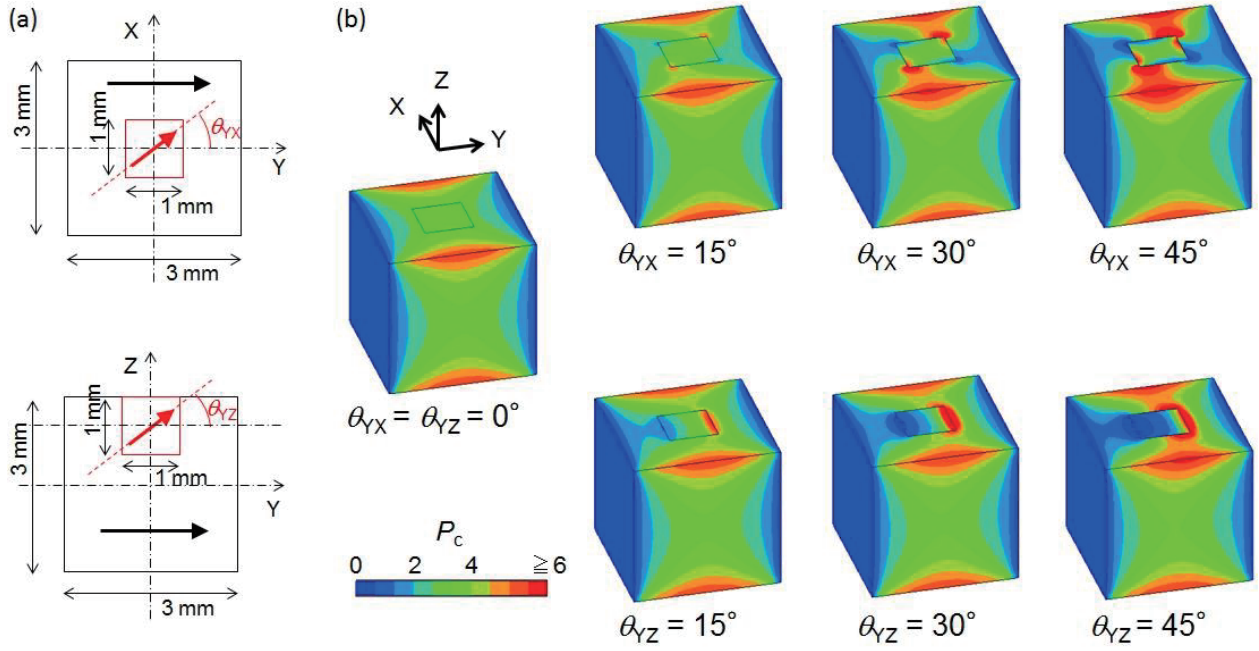

Fig. 4 (a) Model of Nd-Fe-B sintered magnet for calculation with 3D-FEM and (b) distribution of permeance coefficient P_c when θ_{YX} and θ_{YZ} were changed from 0 to 45°.

surface planes located parallel to the orientation direction, which demagnetized independently of the interior of the magnet[10]. When the coercivity was 1600 kA/m or higher, the bulk coercivity was measured by using a pulsed BH tracer. To understand the influence of the demagnetizing field on the magnet surface, a three-dimensional finite element method (3D-FEM) was used to simulate the distribution of the permeance coefficient.

3. Result and discussion

Figure 2 shows the bulk coercivity and coercivity of the surface layer of the HA magnets when changing the Dy content and annealing temperature. The bulk coercivity increased as the Dy content increased and reached the maximum value when the annealing temperature was 500°C or 520°C in each composition. It was found that the coercivity of the surface layer also varied depending on these conditions with the same tendency as the bulk coercivity, even though the

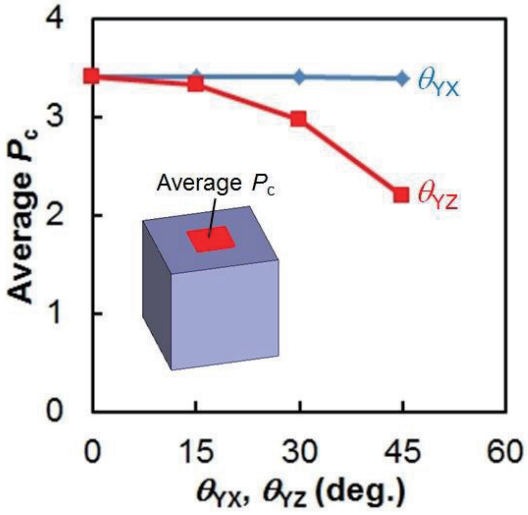

Fig. 5 Average permeance coefficient P_c on surface of 1 × 1 × 1 mm particle when θ_{YX} and θ_{YZ} were changed from 0 to 45°.

coercivity of the surface layer was much smaller than the bulk coercivity. Figure 3 shows the relationship between the bulk coercivity and the coercivity of the surface layer when the degree of alignment, the Dy content, and the annealing temperature were changed. The coercivity of the surface layer changed in proportion to the change in the bulk coercivity depending on the Dy content and the annealing temperature under the same degree of alignment. This suggests that the coercivity of the surface layer also depends on the magnetocrystalline anisotropy of the $(Nd,Dy)_2Fe_{14}B$ main phase and the microstructure, especially around the grain boundary. This result means that the magnetization reversal occurring in the polished surface layer has a similar mechanism to the inside of the magnet. Comparing each HA magnet and MA magnet under the same composition and annealing condition, the coercivity of the surface layer had about the same value, even though the bulk coercivity in the MA magnet was larger than that in the HA magnet. When the degree of alignment decreases, it is expected that the number of grains that incline its easy axis of magnetization in the out-of-plane direction increases on the magnet surface. This may lead to an increase in the local demagnetizing field and induce magnetization reversal in the magnet surface.

To clarify the change in the demagnetizing field due to the inclination of the easy axis of magnetization on the magnet surface, we assumed the simple model shown in Fig. 4(a) and calculated the demagnetizing field by 3D-FEM. First, a 3 × 3 × 3 mm of cubic Nd-Fe-B magnet that was fully magnetized in the Y direction was created. The mesh size had a 0.1 mm pitch, and the total number of units was 27000. Each unit was affected by the static magnetic field from the surrounding units, but there was no exchange interaction among units. Next, we focused on a 1 × 1 × 1 mm of cubic Nd-Fe-B particle that existed in one plane that was parallel to the easy magnetization direction in the 3 × 3 × 3 mm of cubic Nd-Fe-B magnet. The direction of the magnetization of this particle changed independently in the in-plane direction (Y to X) and out-of-plane direction (Y to Z) at angles of θ_{YX} and θ_{YZ}, respectively. Figure 4(b) shows distributions of permeance coefficient P_c when θ_{YX} and θ_{YZ} were changed from 0 to 45°. When θ_{YX} = θ_{YZ} = 0, the distribution of P_c in a surface area of 1 mm square, indicated by a square line in Fig. 4(b), was relatively even. When θ_{YZ} was increased, the distribution of P_c in the area changed greatly compared with the case in which θ_{YX} was increased. Figure 5 shows the change in average P_c in the area with respect to θ_{YX} and θ_{YZ}. The average P_c decreased as θ_{YZ} increased, whereas it hardly changed when θ_{YX} varied. From the relation of $N = 1 / (1 + P_c)$, where N is a demagnetizing factor, it is suggested that the local demagnetizing field becomes large when the easy axis of magnetization is tilted in the out-of-plane direction on the magnet surface. Therefore, the increase in the local demagnetizing field promotes magnetization reversal and may decrease the coercivity on the magnet surface, which is the reason for the non-proportional relationship between the bulk coercivity and the surface layer coercivity when comparing HA and MA magnets.

4. Conclusion

To clarify the correlation between the surface and the inside of a Nd-Fe-B-based sintered magnet, the bulk coercivity and coercivity of the polished surface layer were measured systematically. It was revealed that the bulk coercivity and coercivity of the surface layer were in a proportional relationship, which suggests that the magnetization reversal occurring in the surface layer has a mechanism similar to the inside of the magnet. The relationship between the bulk coercivity and coercivity of the surface layer was not proportional when the degree of alignment decreased, which can be explained as the increase in the local demagnetizing field due to the low degree of alignment promoting the magnetization reversal and decreasing the coercivity on the magnet surface.

References

1) D. Li and K. J. Strnat: *J. Appl. Phys.*, **57**, 4143 (1985).
2) A. Fukuno and R. C. O'Handley: *J. Appl. Phys.*, **65**, 4959 (1989).
3) T. Yamaoka, H. Tsujikawa, R. Hirose, A. Ito, H. Kawamura, and T. Sakon: *J. Magn. Soc. Jpn.*, **35**, 60 (2011) [in Japanese].
4) J. Thielsch, T.G. Woodcock, L. Schultz, and O. Gutfleisch: *J. Appl. Phys.*, **111**, 103901 (2012).
5) T. Kohashi, K. Motai, T. Nishiuchi, T. Maki, and S. Hirosawa: *J. Magn. Soc. Jpn.*, **33**, 374 (2009).
6) H. Suzuki, Y. Satsu, T. Kohashi, K. Motai, and M. Komuro: *J. Appl. Phys.*, **109**, 07A746 (2011).

7) K. Toyoki, Y. Kotani, Y. Senba, D. Billington, H. Okazaki, A. Yasui, W. Ueno, H. Ohashi, Y. Shiratsuchi, S. Hirosawa, K. Hono, and T. Nakamura: Proc. 24th Int. Workshop on Rare-Earth and Future Permanent Magnets and their Applications, Darmstadt, 2016, 129 (2016).
8) D. Harimoto, Y. Matsuura, and S. Hosokawa: *J. Jpn. Soc. Powder Powder Metallurgy*, **53**, 282 (2006) [in Japanese].
9) Y. Matsuura, J. Hoshijima, and R. Ishii: *J. Magn. Magn. Mater.*, **336**, 88 (2013).
10) K. Kobayashi, M. Nakamura, and K. Urushibara: *J. Appl. Phys.,* **117**, 173909 (2015).

Received Oct. 17, 2017; Revised Nov. 27, 2017; Accepted Dec. 29, 2017

J. Magn. Soc. Jpn., **42**, 24-29 (2018)

<Paper>

Influence of misorientation angle between adjacent grains on magnetization reversal in Nd-Fe-B-based sintered magnet

T. Maki, R. Uchikoshi*, R. Ishii, M. Natsumeda, T. Nishiuchi, and M. Takezawa*

Magnetic Materials Research Laboratory, Magnetic Materials Company, Hitachi Metals, Ltd., *2-15-17 Egawa, Shimamoto-cho, Mishima-gun, Osaka 618-0013, Japan*

*Department of Applied Science for Integrated System Engineering, Kyushu Institute of Technology, *1-1 Sensui-cho, Tobata-ku, Kitakyushu-shi, Fukuoka 804-8550, Japan*

To clarify the difference between the degree of alignment dependence of coercivity and the angular dependence of coercivity, the crystal orientation distribution and demagnetization curve of Nd-Fe-B-based sintered magnets with different degrees of alignment were compared. It is suggested that the increase in coercivity due to a low degree of alignment cannot be explained only by the angular dependence of coercivity. A crystal orientation analysis and in-situ observation of magnetic domains that were performed in the same area clarified that the ratio of the grain boundary where the magnetization reversal stopped became larger when the misorientation angle between adjacent grains became larger. This suggests that a grain boundary having a larger misorientation angle is one of the factors that suppresses magnetization reversal.

Key words: Nd-Fe-B magnet, coercivity, degree of alignment, Kerr microscope, magnetic domain

1. Introduction

Nd-Fe-B-based magnets used in motors for electric vehicles (EV) and hybrid electric vehicles (HEV) are required to have a high coercivity for maintaining thermal stability. Generally, heavy rare earth elements such as Dy and Tb are added to increase the magnetocrystalline anisotropy of the $Nd_2Fe_{14}B$ compound to obtain a high coercivity. However, these elements are recognized as materials with a high supply risk, and there is a strong demand for Nd-Fe-B -based magnets to achieve a high coercivity with a lower amount of heavy rare earth elements.

The coercivity of the Nd-Fe-B-based magnet is greatly changed not only by the addition of heavy rare earth elements but also by the microstructure. It was pointed out that Nd-rich phases existing at the grain boundary play an important role in coercivity[1)-3)], and it was observed that a Nd-rich phase inhibited propagating magnetic domains[4,5)]. The coercivity of the Nd-Fe-B-based sintered magnet also strongly depends on the degree of alignment of the $Nd_2Fe_{14}B$ phase, and it is experientially known that the coercivity increases as the degree of alignment decreases[6,7)]. It was also reported that the coercivity increases when the angle Θ between the easy magnetization direction of the Nd-Fe-B sintered magnet and the direction of the applied magnetic field becomes large, which is referred to as the angular dependence of coercivity[8)]. This dependency is explained by the magnetic domain wall motion model, which shows that the coercivity increases at a rate of $1/\cos\Theta$. Attempts have been made to explain the dependence of the coercivity on the degree of alignment by combining the angular dependence and orientation distribution[7)], but it is not fully understood. When the degree of alignment decreases, it is easy to expect that the distribution of the orientation angle θ between the applied magnetic field H and the easy axis of magnetization of each $Nd_2Fe_{14}B$ grain broadens as shown in Fig. 1. However the distribution of the misorientation angle ϕ between the easy axis of magnetization of adjacent grains will change at the same time. There is a possibility that this change in the distribution of ϕ may be related to magnetic domain wall motion and coercivity, but no example has been reported experimentally.

To understand directly the relationship between the microstructure and magnetic domain structure in the Nd-Fe-B-based magnet, various methods for evaluating the magnetic domain structure on the surface of the magnet are studied, such as the magneto-optical Kerr microscope[9),10)], Lorentz transmission electron microscope (Lorentz-TEM)[4),5)], electronic holography[11)], magnetic force microscope

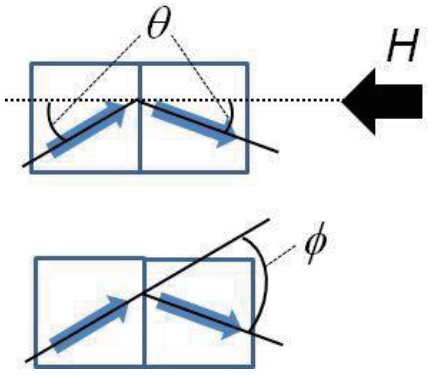

Fig. 1 Schematic images of orientation angle θ between easy axis of magnetization of each grain and applied magnetic field H and misorientation angle ϕ between easy axis of adjacent grains.

(MFM)[12),13)], and spin-polarized scanning electron microscope (spin-SEM)[14),15)]. Among them, the magneto-optical Kerr microscope can perform in-situ observation in a high magnetic field, so it is an effective method for directly observing the magnetization behavior of the Nd-Fe-B magnet[16)]. Takezawa *et al.* reported the in-situ magnetic domain observation of a Nd-Fe-B-based sintered magnet in a magnetic field. Several grains were simultaneously reversed along the direction of the easy axis of magnetization, and when the applied magnetic field increased, the magnetization reversal propagated[17),18)]. It is important to observe a wide area to understand the propagation of magnetization reversal across multiple grain groups, and the magneto-optical Kerr microscope is also suitable in this respect.

In this study, first, to clarify the difference between the degree of alignment dependence of coercivity and the angular dependence of coercivity, we investigated the θ distribution and ϕ distribution of Nd-Fe-B-based sintered magnets with different degrees of alignment. The coercivity was measured by changing the angle between the magnetic field and sample. Subsequently, the magnetization process was analyzed by using recoil curves[20)]. Next, to experimentally evaluate the relationship between the difference in the misorientation angle between adjacent grains and the magnetic domain structure in the Nd-Fe-B-based sintered magnet, a scanning electron microscope with an electron backscatter diffraction (SEM/EBSD) analysis and the in-situ magnetic domain observation in the magnetic field by using a magneto-optical Kerr microscope were conducted in the same observed area.

2. Experimental method

Highly aligned (HA) and moderately aligned (MA) sintered magnets that had a composition of 30.2Nd-67.6Fe-1.0B-0.9Co-0.1Al-0.1Cu-0.1Ga (mass%) were prepared by using an ordinary process except for pressing, which applied a different magnitude of magnetic field. The remanence B_r and the coercivity H_{cJ} of the HA and MA magnets were B_r = 1.44 T, H_{cJ} = 1038 kA/m, B_r = 1.33 T, and H_{cJ} = 1126 kA/m, respectively. The distribution of the degree of grain alignment was analyzed by observing the polished surface plane that was parallel to the easy magnetization direction of the magnet with SEM/EBSD. The sintered magnets were shaped into spheres for magnetic measurement. After magnetization with a pulse magnetic field of 5.6 MA/m, the demagnetization curves were measured in the range of 1.6 to −1.6 MA/m with a vibrating sample magnetometer (VSM). In the case of changing the angle of the applied magnetic field with respect to the easy magnetization direction of the sample, the electromagnet of the VSM was rotated at a 1° pitch with respect to the sample. Each demagnetization curve was corrected by setting the demagnetizing factor N of the sphere to N = 0.33. The recoil curve measurement was repeated by increasing the demagnetization field by 40 kA/m in the second and third quadrants of the demagnetization curve and returning to 0 kA/m, as described in the previous paper[20)].

The sintered magnets used for magnetic domain observations had two compositions (30.2-x)Nd-xDy -67.6Fe-1.0B-0.9Co-0.1Al-0.1Cu-0.1Ga (x = 0, 5.0) with different Dy content, and the MA magnets were used. The magnetic property of a Dy doped (x = 5.0) magnet was B_r = 1.24 T and H_{cJ} = 1958 kA/m. Each sample was cut into 3 × 3 × 3 mm, and the plane that was polished was parallel to the easy magnetization direction for an observation surface. First, SEM/EBSD analyses were performed at the center of the polished plane, and the magnetic domain was then observed with the magneto-optical Kerr microscope. An SiO film was deposited on the surface of each sample by vacuum evaporation for antireflection[17)]. Each sample was magnetized in the orientation direction with a pulsed magnetic field of 4.0 MA/m and then set in the magneto-optical Kerr microscope. A DC magnetic field was applied to the samples in the range of 1.6 to −1.6 MA/m. Magnetization reversal was detected from the change in contrast in an observation image, and the reversed area was extracted by image processing[18)]. To obtain the effective magnetic field in the observation area, the demagnetizing field at the center of the plane that is parallel to the easy magnetization direction of the cubic Nd-Fe-B magnet was calculated by using a three-dimensional finite element method (3D-FEM). The effective magnetic field H_{eff} was obtained from the relationship of $H_{eff} = H_{ex} - H_d$, where H_{ex} and H_d are the external magnetic field and the demagnetizing field from a sample, respectively. For example, in the case of x = 0, H_{eff} = −250 kA/m when H_{ex} = 0 kA/m.

3. Results and discussion

3.1 Distribution of θ and ϕ

Figure 2 shows inverse pole figure maps of the MA and HA magnets with the horizontal direction as an orientation direction. Compared with the HA magnet, the MA magnet had a large dispersion of crystal orientation. The orientation angle θ between the direction of the applied magnetic field H and the direction of the easy axis of magnetization in each grain was calculated from the direction cosine of the RD direction and <001> direction of each grain. The misorientation angle ϕ between the easy axis of adjacent grains that was defined regardless of the relative position of adjacent grains was calculated from the direction cosine of <001> directions of adjacent grains. Figures 3(a)-(d) show the distribution of θ and ϕ in each sample. Compared with the HA magnet, both of the distributions of θ and ϕ in the MA magnet were broad, and the frequencies on the higher angle were large. It was found that not only the orientation angles

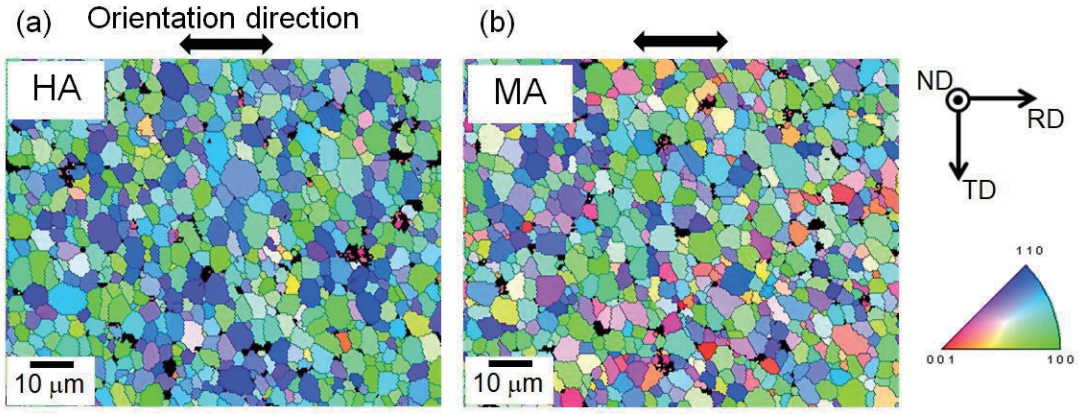

Fig. 2 Inverse pole figure maps of $Nd_2Fe_{14}B$ phases of (a) highly aligned (HA) magnet and (b) moderately aligned (MA) magnet.

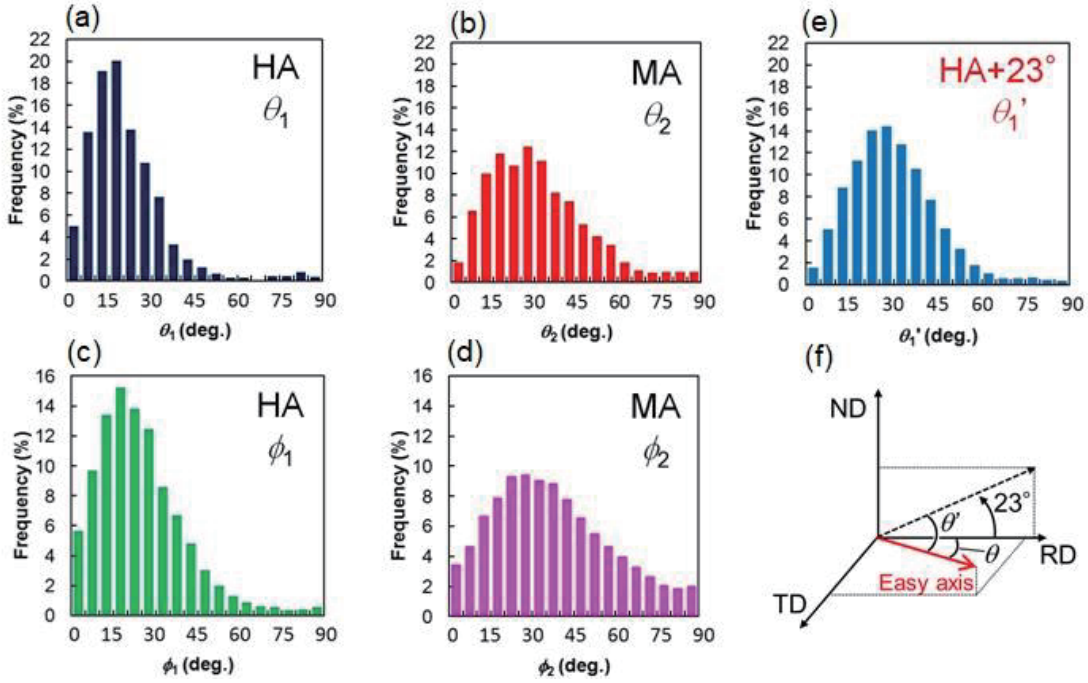

Fig. 3 (a) to (d) Distributions of θ and ϕ of HA and MA magnets, (e) distribution of θ' of MA magnet calculated from direction tilted 23° from orientation direction, and (f) schematic image of θ and θ'.

but also the misorientation angles between adjacent grains had a wide distribution when the degree of alignment decreased.

3.2 Relationships between distribution of θ, ϕ, and coercivity

Figure 4 shows demagnetization curves of the HA magnet, MA magnet, and HA magnets that were inclined at 23° and 48° with respect to the direction of the applied magnetic field. When the HA magnet was tilted at an angle of 23°, the coercivity was clearly lower than that of the MA magnet, whereas the squareness J_r/J_s of each sample was almost the same. When trying to obtain the same coercivity as the MA magnet, the HA magnet must be tilted up to 48° with respect to the applied magnetic field. Figure 3(e) shows the distribution of θ', which was obtained by calculating the angle θ' between the direction of the easy axis of magnetization in each grain and the direction that was intentionally deviated 23° from the RD direction. The distribution of θ' was similar to the distribution of θ of the MA magnet. Therefore, the MA magnet and HA magnet tilted at 23° had approximately the same orientation distribution as the direction of the applied field, which was consistent with the fact that J_r/J_s was the same in the demagnetization curve. These results suggest that the large increase in coercivity due to the low degree of alignment cannot be explained only by the angular dependence of coercivity.

Figure 5(a) shows whole recoil curves of the MA

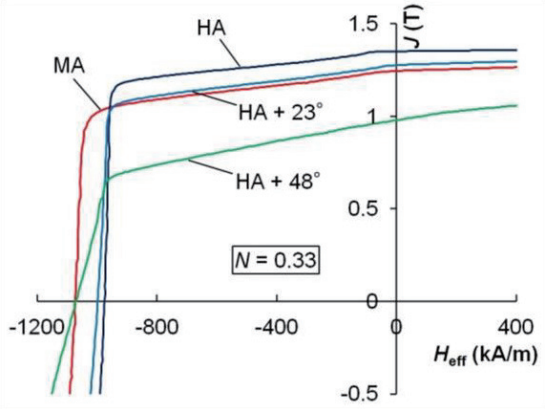

Fig. 4 Demagnetization curves measured for HA magnet, MA magnet, and HA magnet inclined at 23° and 48° with respect to magnetic field direction (spherical sample, demagnetizing factor $N = 0.33$).

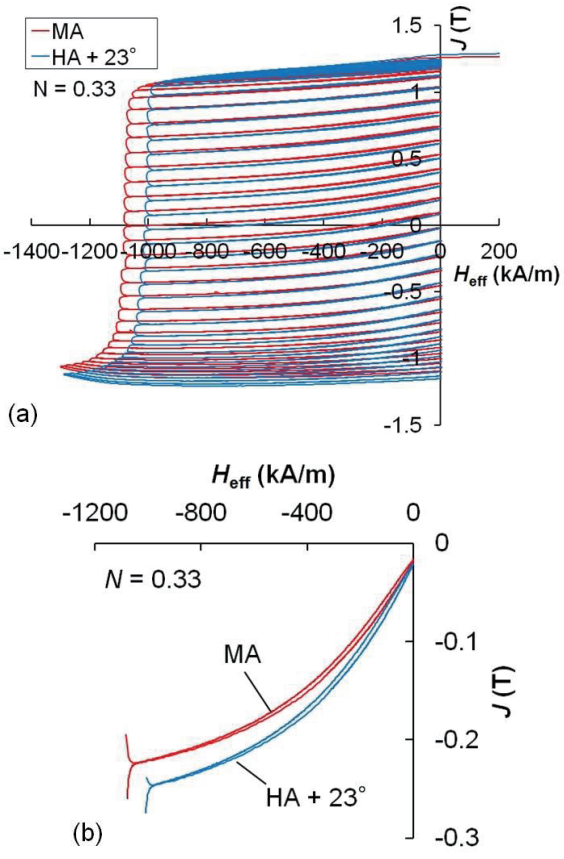

Fig. 5 (a) Recoil curves of MA magnet and HA magnet measured by tilting 23° with respect to magnetic field direction and (b) comparison of two recoil curves returning to near origin position.

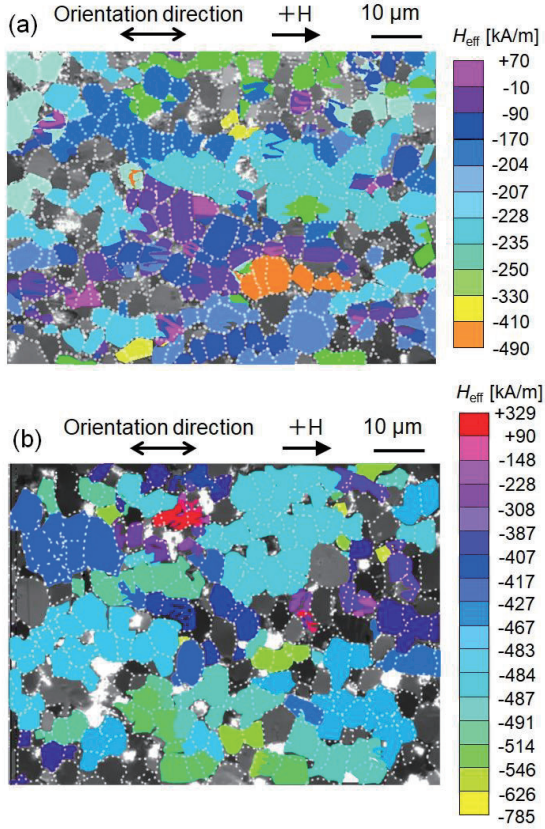

Fig. 6 Reversed region in each effective magnetic field H_{eff} extracted from Kerr microscope image in demagnetization process of (a) Dy undoped ($x = 0$) and (b) Dy doped ($x = 5.0$) MA magnets.

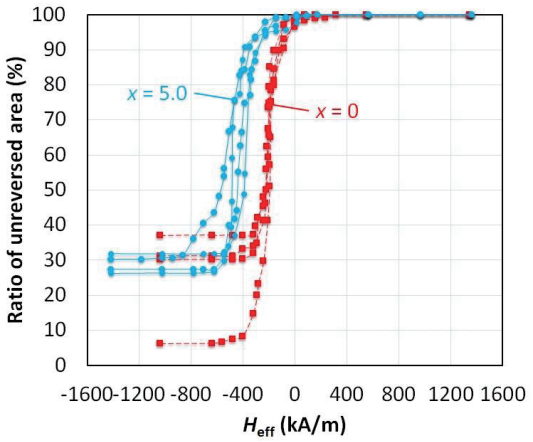

Fig. 7 Changes in ratio of unreversed area with regards to H_{eff} in demagnetization process of each of four observed fields for $x = 0$ and $x = 5.0$ samples extracted from Kerr microscope image.

magnet and HA magnet tilted at 23°, and Fig. 5(b) shows recoil curves of both samples that returned to near the origin. The curvature of the recoil curve of the MA magnet was smaller than that of the tilted HA magnet. In the previous paper[20], it was pointed out that the recoil curve of a Nd-Fe-B sintered magnet that has an average grain size of several μm contains domain wall motion in its magnetization process. The small curvature of the recoil curve suggests that the magnetic domain wall motion in the MA magnet was small. As shown in Fig. 3(d), the MA magnet had a large distribution of ϕ, which may be related to the

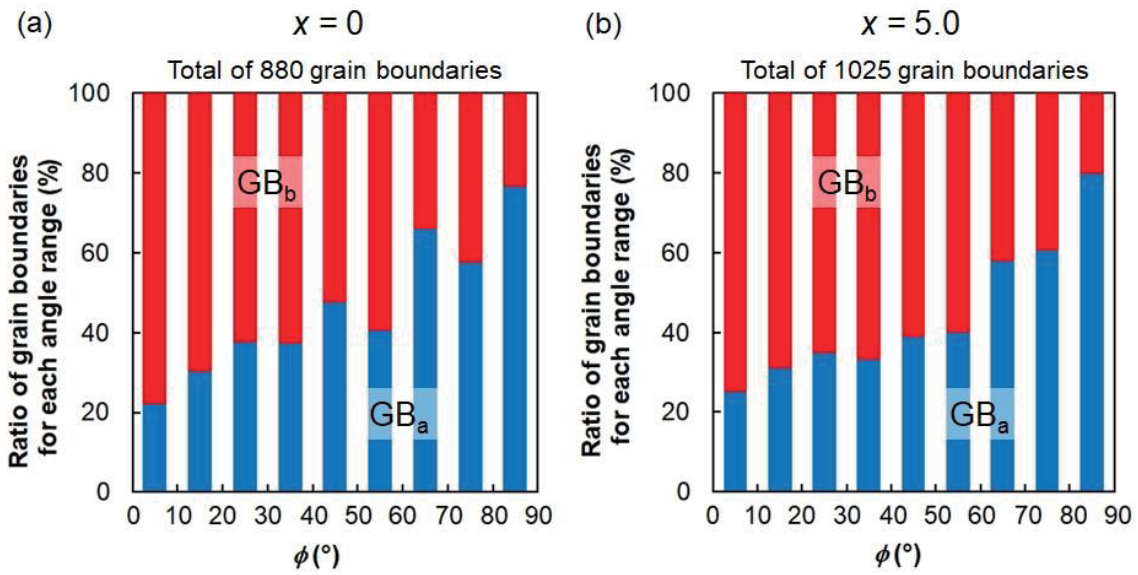

Fig. 8 Ratio of GB_a and GB_b with respect to misorientation angle of adjacent grains in (a) Dy undoped magnet ($x = 0$) and (b) Dy doped magnet ($x = 5.0$).

suppression of the domain wall motion.

3.3 Relationship between propagation of magnetization reversal and misorientation angle ϕ

Figure 6 shows magnetically inversed areas in each magnetic field H_{eff} extracted from the magnetic domain observation results for the demagnetization process of the Dy undoped ($x = 0$) and Dy doped ($x = 5.0$) MA magnets. These samples had almost the same distribution of θ and ϕ. Grain boundaries in the sample are indicated by white dotted lines to facilitate recognition. The unreversed areas were considered to be undetected areas because of a significantly weak change in contrast and were excluded from the evaluation. Several grains were reversed simultaneously along the magnetic easy axis direction, which is similar to the case of highly aligned Nd-Fe-B sintered magnets[17]. To estimate the repeatability of the demagnetization process in the same H_{eff}, we prepared four samples for both $x = 0$ and $x = 5.0$ under the same condition and observed these samples at the center of each polished plane with the same method discussed above. Figure 7 shows changes in the ratio of the unreversed area with respect to H_{eff} in the demagnetization process of each of the four observed fields with $x = 0$ and $x = 5.0$. In the surface layer for $x = 5.0$, which had a large amount of Dy, the magnetization reversal propagated at a higher magnetic field. It is thought that the magnetization reversal on the surface depended on the magnitude of magnetocrystalline anisotropy of the $(Nd,Dy)_2Fe_{14}B$ phase, even though the coercivity of the polished surface layer was lower than the interior of the magnet due to the deterioration and lack of a Nd-rich grain boundary phase. When a group of grains was reversed in a certain applied magnetic field, positions where the magnetization reversal stopped often existed along the grain boundary. To clarify how the misorientation angle ϕ between two grains on both sides of the grain boundary affects the magnetization reversal, the grain boundaries were divided into two groups: GB_a and GB_b. GB_a is a grain boundary where the magnetization reversal stopped, which is indicated by the borders of the different colored regions in Fig. 6. GB_b is a grain boundary where the magnetization reversal did not stop that is located inside the colored region. In this study, the relationship between GB_a and H_{eff}, as well as GB_b and H_{eff}, was not considered. The grain boundaries that were clearly separated by a large Nd-rich phase were excluded from the evaluation. Figure 8(a) shows the result of dividing about 900 grain boundaries into GB_a and GB_b for the $x = 0$ samples and the ratio of GB_a and GB_b in each angular range of ϕ. It was found that the ratio of GB_a became larger when ϕ became larger. This tendency was similar when about 1000 grain boundaries were analyzed in the samples with $x = 5.0$, as shown in Fig. 8(b). These results experimentally suggest that a grain boundary with a larger misorientation angle of adjacent grains ϕ has the ability to suppress magnetization reversal. It is also considered that the influence of the misorientation angle on suppressing magnetization reversal does not differ much even when the saturation magnetization and magnetocrystalline anisotropy of the main phase are different.

4. Conclusion

To clarify the difference between the degree of alignment dependence of coercivity and angular dependence of coercivity, the crystal orientation

distribution and demagnetization curve of Nd-Fe-B based sintered magnets with different degrees of alignment were compared. It was shown that an increase in coercivity due to a low degree of alignment cannot be explained only by the angular dependence of coercivity and that domain wall movement is small in a magnet that has a low degree of alignment. A crystal orientation analysis and in-situ magneto-optical Kerr microscope observation performed in the same area clarified that the ratio of the grain boundary where the magnetization reversal stopped became larger when the misorientation angle between adjacent grains became larger. This suggests that a grain boundary having a larger misorientation angle is one of the factors that suppresses magnetization reversal. From the above results, it can be said that the increase in coercivity by the decrease in the degree of alignment is caused by the suppression of magnetization reversal at the grain boundary due to the increase in the misorientation angle between adjacent grains. The reason that the misorientation angle suppresses magnetization reversal is considered to be the reduction in magnetic interaction between grains or a change in the microstructural relationship between the main phase and grain boundary phase. Further understanding of the grain boundary structure and magnetization process is necessary in the future.

References

1) K. Hiraga, M. Hirabayashi, M. Sagawa, and Y. Matsuura: *Jpn. J. Appl. Phys.*, **24**, L30 (1985).
2) R. K. Mishra, J. K. Chen, and G. Thomas: *J. Appl. Phys.*, **59**, 2244 (1986).
3) F. Vial, F. Joly, E. Nevalainen, M. Sagawa, K. Hiraga, and K. T. Park: *J. Magn. Magn. Mater.*, **242-245**, 1329 (2002).
4) Y. Shinba, T. J. Konno, K. Ishikawa, and K. Hiraga: *J. Appl. Phys.*, **97**, 053504 (2005).
5) H. Sepehri-Amin, T. Ohkubo, T. Shima, and K. Hono: *Acta. Mater.*, **60**, 819 (2012).
6) A. Handstein, K. -H. Muller, D. Eckert, and P. Northnagel: *J. Magn. Magn. Mater.*, **101**, 382 (1991).
7) Y. Matsuura, J. Hoshijima, and R. Ishii: *J. Magn. Magn. Mater.*, **336**, 88 (2013).
8) D. Givord, P. Tenaud, and T. Viadieu: *J. Magn. Magn. Mater.*, **72**, 247 (1988).
9) D. Li and K. J. Strnat: *J. Appl. Phys.*, **57**, 4143 (1985).
10) A. Fukuno and R. C. O'Handley: *J. Appl. Phys.*, **65**, 4959 (1989).
11) Y. -G. Park and D. Shindo: *J. Magn. Magn. Mater.*, **238**, 68 (2002).
12) T. Yamaoka, H. Tsujikawa, R. Hirose, A. Ito, H. Kawamura, and T. Sakon: *J. Magn. Soc. Jpn.*, **35**, 60 (2011) [in Japanese].
13) J. Thielsch, T.G. Woodcock, L. Schultz, and O. Gutfleisch: *J. Appl. Phys.*, **111**, 103901 (2012).
14) T. Kohashi, K. Motai, T. Nishiuchi, T. Maki, and S. Hirosawa: *J. Magn. Soc. Jpn.*, **33**, 374 (2009).
15) H. Suzuki, Y. Satsu, T. Kohashi, K. Motai, and M. Komuro: *J. Appl. Phys.*, **109**, 07A746 (2011).
16) M. Takezawa, T. Shimada, S. Kondo, S. Mimura, Y. Morimoto, T. Hidaka, and J. Yamasaki: *J. Appl. Phys.*, **101**, 09K106 (2007).
17) M. Takezawa, Y. Kimura, Y. Morimoto, and J. Yamasaki: *IEEE Trans. Magn.*, **49**, 3262 (2013).
18) M. Takezawa, H. Ogimoto, Y. Kimura and Y. Morimoto: *J. Appl. Phys.*, **115**, 17A733 (2014).
19) K. Toyoki, Y. Kotani, Y. Senba, D. Billington, H. Okazaki, A. Yasui, W. Ueno, H. Ohashi, Y. Shiratsuchi, S. Hirosawa, K. Hono, and T. Nakamura: Proc. 24th Int. Workshop on Rare-Earth and Future Permanent Magnets and their Applications, Darmstadt, 2016, 129 (2016).
20) T. Maki and S. Hirosawa: *J. Appl. Phys.*, **103**, 043904 (2008).

Received Oct. 2, 2017; Accepted Jan. 18, 2018

J. Magn. Soc. Jpn., **42**, 30-36 (2018)

<Paper>

Structure Characterization of Fe, Co, and Ni Thin Films Epitaxially Grown on GaAs(111) Substrate

Takahiro Soda[1], Shigeyuki Minakawa[1], Masaaki Futamoto[1], Mitsuru Ohtake[1,2], and Nobuyuki Inaba[3]

[1]Faculty of Science and Engineering, Chuo University, *1-13-27 Kasuga, Bunkyo-ku, Tokyo 112-8551, Japan*
[2]Faculty of Engineering, Kogakuin University, *2665-1 Nakano, Hachioji, Tokyo 192-0015, Japan*
[3]Faculty of Engineering, Yamagata University, *4-3-16 Jyonan, Yonezawa, Yamagata 992-8510, Japan*

Fe, Co, and Ni films of 40 nm thickness are prepared on GaAs(111) single-crystal substrates at room temperature by using a radio-frequency magnetron sputtering system. The film growth behavior and the crystallographic properties are investigated by *in-situ* reflection high-energy electron diffraction and pole-figure X-ray diffraction. bcc single-crystals of (111) orientation are formed on the substrates for all the film materials, though the bcc structure is metastable for Co and Ni materials. The metastable structure is stabilized through hetero-epitaxial growth. Fe films possess bcc structure for the investigated thickness range. On the contrary, the bcc-Co and the bcc-Ni crystals, respectively, start to transform into hcp and fcc structures, as the thickness is increased beyond 2 nm. The phase transformations occur through atomic displacements from the close-packed planes of bcc(1$\bar{1}$0), bcc($\bar{1}$01), and bcc(01$\bar{1}$), which are perpendicular to the substrate surface, to hcp(0001) and fcc(111) close-packed planes. The crystallographic orientation relationships of hcp and fcc crystals with respect to bcc crystal are similar to the Kurdjumov-Sachs relationship.

Key words: 3*d* transition metals, epitaxial growth, thin films, GaAs(111) substrate, metastable bcc structure, phase transformation

1. Introduction

Hybrid structure of ferromagnetic metal and semiconductor materials has been investigated for spin electronics applications like spin-dependent field effect transistors, etc. bcc phase is stable for Fe, whereas that is metastable for Co and Ni at room temperature (RT). It has been reported that magnetic tunnel junction elements prepared by using Co films with metastable bcc structure show high tunnel magnetoresistance ratios[1,2]. The magnetic and electronic properties vary depending on the crystal structure. It is thus important to understand the formation conditions of magnetic films with metastable bcc structure.

Metastable bcc phase formation has been recognized for very thin Co[3–5] and Ni[6] films on GaAs single-crystal substrates of (100) and (110) orientations around RT deposited by molecular beam epitaxy (MBE). With increasing the thickness, most of the bcc-Co and the bcc-Ni crystals transformed into more stable hcp or fcc structure and the resulting films involved large volumes of hcp or fcc crystals. Recently, we succeeded in the formation of Co and Ni films with bcc structure on GaAs(100)[7,8] and GaAs(110)[9] substrates by sputtering, which is more suitable than MBE for mass-production applications. The thickness stability of bcc phase and the transformation process to hcp or fcc structure were investigated. With increasing the thickness beyond 2 nm, the bcc crystals formed on GaAs(100) and GaAs(110) substrates, respectively, started to transform into stable structures through atomic displacements parallel to the six bcc{110} close-packed planes and the four bcc(10$\bar{1}$), bcc(01$\bar{1}$), bcc(011), and bcc(101) planes which are 60° inclined from the substrate surface. The slide planes, where the phase transformation occurs, differ depending on the substrate orientation.

In our previous study[10], Co films were prepared on GaAs(111) substrates by varying the substrate temperature from RT to 600 °C. The film structure was investigated by reflection high-energy electron diffraction (RHEED), where the incident electron beam was parallel to only GaAs[1$\bar{1}$0]. In the early stage of film growth at temperatures lower than 200 °C, Co(111) crystals with bcc structure were formed. With increasing the thickness, the bcc(111) crystals started to transform into the stable phase, similar to the cases of Co films formed on GaAs(100)[7,8] and GaAs(110)[9] substrates. When the substrate temperature was higher than 400 °C, Ga atoms of substrate seemed to diffuse into the Co films and an ordered alloy with bcc-based *B*2 structure was formed.

In the present study, Fe, Co, and Ni films are prepared on GaAs(111) substrates at RT under similar deposition conditions. The detailed growth behaviors are studied by RHEED using two kinds of incident electron beam, GaAs[1$\bar{1}$0] and GaAs[11$\bar{2}$]. The resulting structure is characterized by out-of-plane, in-plane, and pole-figure X-ray diffractions (XRDs). The influences of film material and thickness on the crystallographic properties are systematically investigated.

2. Experimental Procedure

A radio frequency (RF) magnetron sputtering system equipped with an RHEED facility was employed. The base pressure was lower than 4×10^{-7} Pa. GaAs(111) substrates were heated at 600 °C before deposition to obtain clean surfaces. Figures 1(a) and 2(a) show the RHEED patterns observed for a GaAs substrate after annealing. The incident electron beam is parallel to GaAs[1$\bar{1}$0] in Fig. 1(a), whereas that is parallel to GaAs[11$\bar{2}$] in Fig. 2(a). Diffraction patterns consisting of spots are observed, which may suggest that the substrate surface involves an atomic level roughness. Figures 1(b) and 2(b) show the schematic diagrams of diffraction patterns of a *B*3(111) single-crystal surface calculated by using the two kinds of electron beam direction. The experimental data of Figs. 1(a) and 2(a)

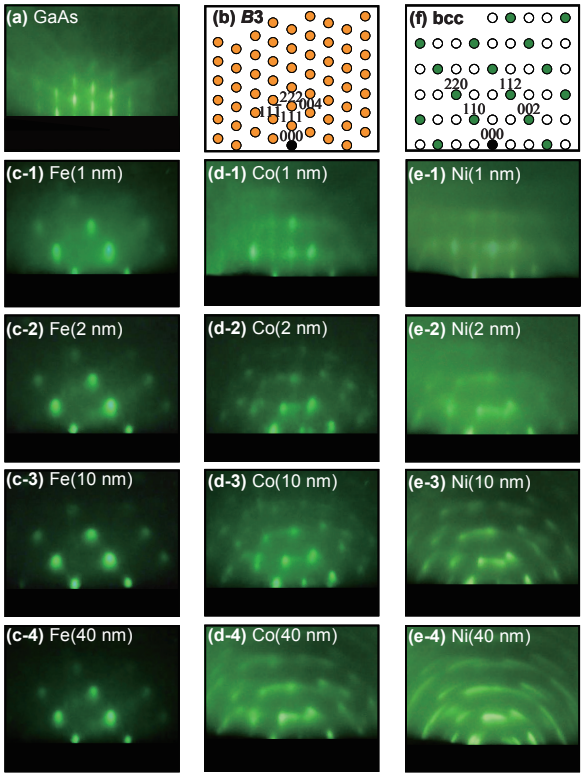

Fig. 1 (a) RHEED pattern observed for a GaAs(111) substrate. (b) Schematic diagram of RHEED pattern simulated for a *B*3(111) substrate. (c)–(e) RHEED patterns observed for (c) Fe, (d) Co, and (e) Ni films deposited on GaAs substrates at RT. The film thicknesses are (c-1)–(e-1) 1, (c-2)–(e-2) 2, (c-3)–(e-3) 10, and (c-4)–(e-4) 40 nm. (f) Schematic diagram of a bcc(111) single-crystal with reconstructed surface of $p(3\times3)$. The incident electron beam is parallel to $[1\bar{1}0]$.

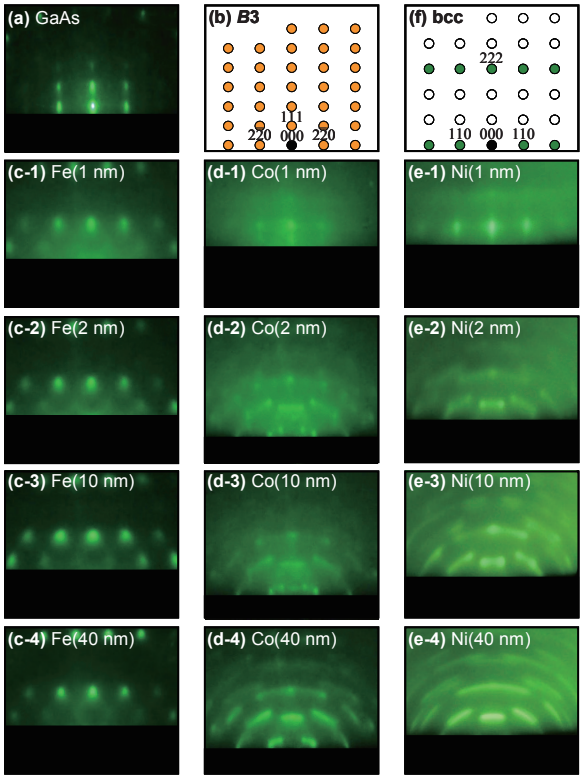

Fig. 2 (a) RHEED pattern observed for a GaAs(111) substrate. (b) Schematic diagram of RHEED pattern simulated for a *B*3(111) substrate. (c)–(e) RHEED patterns observed for (c) Fe, (d) Co, and (e) Ni films deposited on GaAs substrates at RT. The film thicknesses are (c-1)–(e-1) 1, (c-2)–(e-2) 2, (c-3)–(e-3) 10, and (c-4)–(e-4) 40 nm. (f) Schematic diagram of a bcc(111) single-crystal with reconstructed surface of $p(3\times3)$. The incident electron beam is parallel to $[11\bar{2}]$.

agree with the simulation results of Figs. 1(b) and 2(b), respectively. A clean GaAs(111) surface with *B*3 structure is thus obtained. A chemical analysis is necessary to determine the kind of atom terminated at the surface.

Fe, Co, and Ni films were prepared on the substrates at RT by varying the thickness in a range from 1 to 40 nm. The distance between target and substrate was fixed at 150 mm. The Ar gas pressure was kept constant at 0.67 Pa. Fe, Co, and Ni targets of 3 inch diameter were employed and the respective RF powers were fixed at 48, 54, and 50 W, where the deposition rate was 0.02 nm/s for all the materials.

The surface structure was studied by RHEED. The resulting film structure was investigated by XRDs with Cu-Kα radiation (λ = 0.15418 nm). The magnetization curves were measured by vibrating sample magnetometry.

3. Results and Discussion

Figures 1(c-1)–(e-1) and 2(c-1)–(e-1) show the RHEED patterns observed for Fe, Co, and Ni films of 1 nm thickness prepared on GaAs(111) substrates. Clear RHEED patterns are recognized for all the film materials. The films grow epitaxially on the substrates. Figures 1(f) and 2(f) show the schematic diagrams of RHEED patterns simulated for a bcc(111) single-crystal, where the open circle spots correspond to the reflections from reconstructed surface of $p(3\times3)$. The RHEED patterns observed for Fe film are in agreement with the simulated patterns without open circle spots, whereas those observed for Co and Ni films are matching with the simulated patterns involving open circle spots. bcc structure is thus stabilized not only for the Fe film but also for the Co and the Ni films through hetero-epitaxial growth on GaAs(111) substrate, similar to the cases of films prepared on GaAs(100)[7,8] and GaAs(110)[9] substrates. The epitaxial relationship is determined by RHEED as

$$\mathrm{bcc}(111)[1\bar{1}0] \parallel \mathrm{GaAs}(111)[1\bar{1}0].$$

Figures 1(c-2)–(c-4) and 2(c-2)–(c-4) show the RHEED patterns observed for Fe films thicker than 2 nm. RHEED patterns corresponding to the diffraction patterns simulated for bcc(111) surface remain unchanged till the end of 40-nm-thick film formation. Figures 1(d-2)–(e-4) and 2(d-2)–(e-4) show the RHEED patterns observed for Co and Ni films thicker than 2 nm. As the thickness increases, the RHEED spots become broader and diffraction spots different from those of bcc(111) surface appear. The result indicates that a phase transformation is taking place.

When a bulk bcc material transforms into fcc

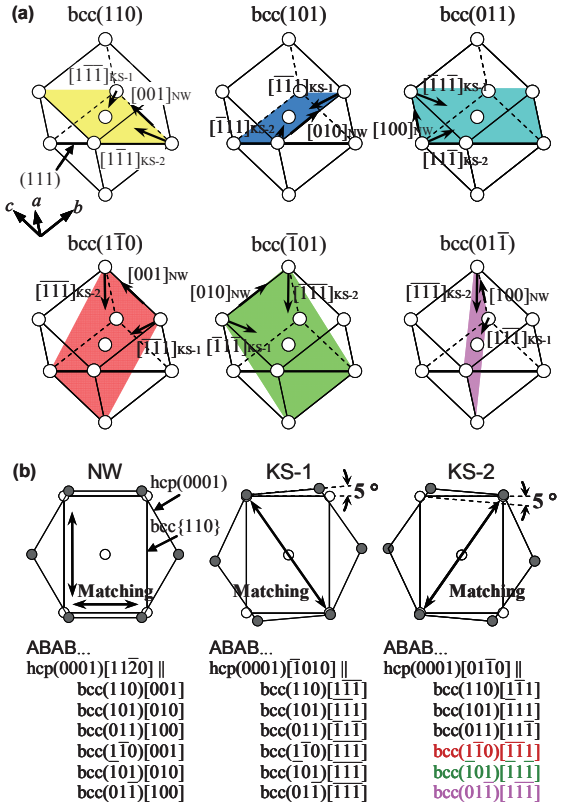

Fig. 3 (a) Configuration of bcc{110} close-packed planes in bcc crystal with the (111) plane parallel to the substrate surface. (b) Crystallographic orientation relationships of bcc-hcp phase transformation.

structure, there are two possibilities in the crystallographic orientation relationship, Nishiyama-Wasserman (NW)[11,12] and Kurdjumov-Sachs (KS)[13]. The phase transformation occurs through atomic displacements from six bcc{110} close-packed planes to fcc(111) close-packed plane. The crystallographic orientation relationship of bcc-hcp phase transformation seems similar to that of bcc-fcc transformation, as shown in Fig. 3. The phase transformation in Co film is considered to occur through atomic displacements from all the six {110} close-packed planes, from the three close-packed planes of bcc(110), bcc(101), and bcc(011) which are 35° canted from the substrate surface, or from the three close-packed planes of bcc(1$\bar{1}$0), bcc($\bar{1}$01), and bcc(01$\bar{1}$) which are perpendicular to the substrate surface. Figures 4(a) and 5(a) show the schematic diagrams of RHEED patterns calculated for hcp crystals transformed through atomic displacements from the bcc(110), bcc(101), and bcc(011) planes. Figures 4(b) and 5(b) show the schematic diagrams of RHEED patterns simulated for hcp crystals transformed through atomic displacements from the bcc(1$\bar{1}$0), bcc($\bar{1}$01), and bcc(01$\bar{1}$) planes. The RHEED patterns observed for Co films thicker than 2 nm [Figs. 1(d-2)–(d-4), 2(d-2)–(d-4)] agree with the simulated patterns of Figs. 4(b-3) and 5(b-3), as shown in Fig. 6. The result shows that the phase transformation is not taking place through atomic displacements from the six bcc{110} planes but from the three close-packed planes of bcc(1$\bar{1}$0), bcc($\bar{1}$01), and bcc(01$\bar{1}$) in the KS-2

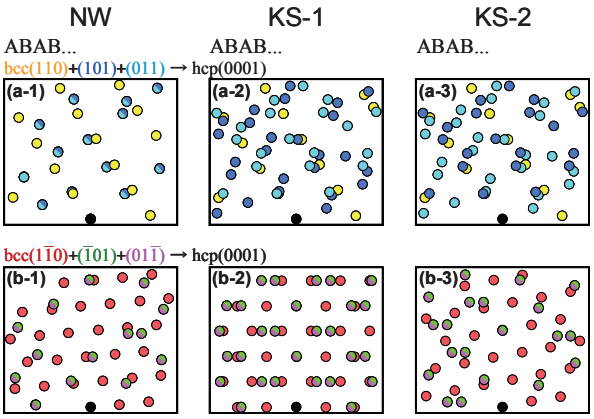

Fig. 4 Schematic diagrams of RHEED patterns simulated for hcp crystals with the atomic stacking sequence of ABAB… along hcp[0001] transformed from a bcc(111) crystal epitaxially grown on GaAs(111) substrate through atomic displacements (a) from bcc(110), bcc($\bar{1}$01), and bcc(011) close-packed planes and (b) from bcc(1$\bar{1}$0), bcc($\bar{1}$01), and bcc(01$\bar{1}$) planes in [(a-1), (b-1)] the NW, [(a-2), (b-2)] the KS-1, and [(a-3), (b-3)] KS-2 relationships. The incident electron beam is parallel to GaAs[1$\bar{1}$0].

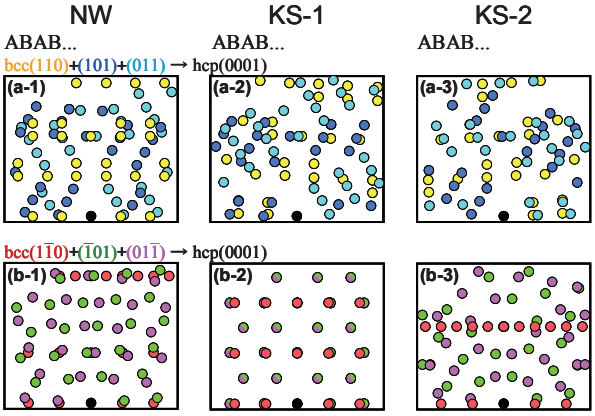

Fig. 5 Schematic diagrams of RHEED patterns simulated for hcp crystals with the atomic stacking sequence of ABAB… along hcp[0001] transformed from a bcc(111) crystal epitaxially grown on GaAs(111) substrate through atomic displacements (a) from bcc(110), bcc($\bar{1}$01), and bcc(011) close-packed planes and (b) from bcc(1$\bar{1}$0), bcc($\bar{1}$01), and bcc(01$\bar{1}$) planes in [(a-1), (b-1)] the NW, [(a-2), (b-2)] the KS-1, and [(a-3), (b-3)] KS-2 relationships. The incident electron beam is parallel to GaAs[11$\bar{2}$].

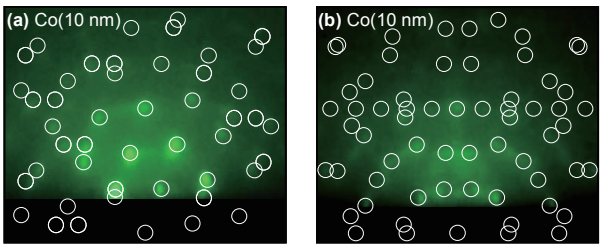

Fig. 6 RHEED patterns observed for a 10-nm-thick Co film prepared on GaAs(111) substrate [Figs. 1(d-3), 2(d-3)] overlapped with reflection spots simulated for hcp crystals transformed through atomic displacements from bcc(1$\bar{1}$0), bcc($\bar{1}$01), and bcc(01$\bar{1}$) planes in the KS-2 relationship [Figs. 4(b-3), 5(b-3)]. The incident electron beam is parallel to (a) GaAs[1$\bar{1}$0] or (b) GaAs[11$\bar{2}$].

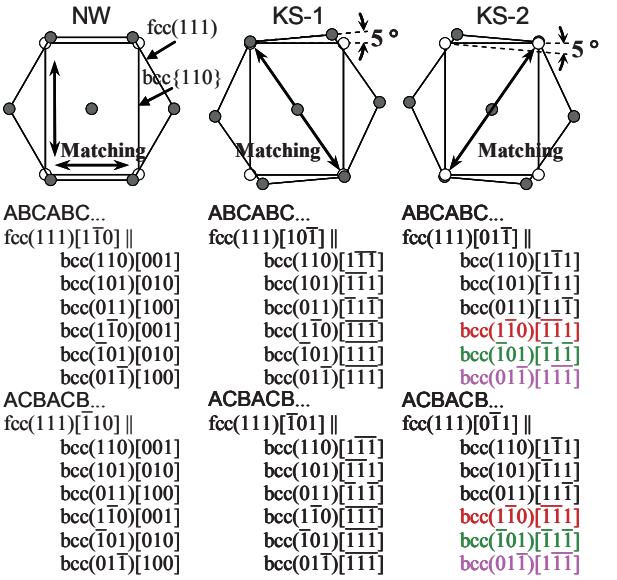

Fig. 7 Crystallographic orientation relationships of bcc-fcc phase transformation.

relationship. Therefore, the Co films thicker than 2 nm involve three hcp variants whose *c*-axes are lying in the film plane and rotated around the film normal by 120° each other. The transformation direction seems to be influenced by the strain caused by accommodation of the lattice misfit between the film and the substrate. The crystallographic orientation relationships are determined as follows,

$$\text{hcp}(0001)[01\bar{1}0] \parallel \text{bcc}(1\bar{1}0)[\bar{1}\bar{1}1],$$
$$\text{hcp}(0001)[01\bar{1}0] \parallel \text{bcc}(\bar{1}01)[\bar{1}1\bar{1}],$$
$$\text{hcp}(0001)[01\bar{1}0] \parallel \text{bcc}(01\bar{1})[1\bar{1}\bar{1}].$$

The crystallographic relationships are slightly different from the results reported for Co film growth on GaAs(111) substrate[10]. In the present study, two different incident electron beam directions are employed to accurately determine the relationships, since broad RHEED spots may include position errors.

Phase transformation in Ni film is also considered to occur through atomic displacements from the three close-packed planes of bcc(1$\bar{1}$0), bcc($\bar{1}$01), and bcc(01$\bar{1}$) to fcc(111) close-packed plane. However, there are two kinds of atomic stacking sequence of fcc(111) plane along the fcc[111] direction, ABCABC… and ACBACB…, for an fcc crystal, while that of hcp(0001) plane along the hcp[0001] direction is only ABAB… Figure 7 summarizes the crystallographic orientation relationships of bcc-fcc phase transformation. Figures 8(a) and 9(a) show the schematic diagrams of RHEED patterns simulated for fcc crystals with the atomic stacking sequence of ABCABC… transformed through atomic displacements from the bcc(1$\bar{1}$0), bcc($\bar{1}$01), and bcc(01$\bar{1}$) planes. Figures 8(b) and 9(b) show the schematic diagrams of RHEED patterns calculated for fcc crystals with the ACBACB… stacking sequence transformed through atomic displacements from the bcc(1$\bar{1}$0), bcc($\bar{1}$01), and bcc(01$\bar{1}$) planes. Figures 10(a) and (b) show the RHEED patterns observed for the 10-nm-thick Ni film [Figs. 1(e-3), 2(e-3)] overlapped with the simulated patterns of fcc crystals with stacking

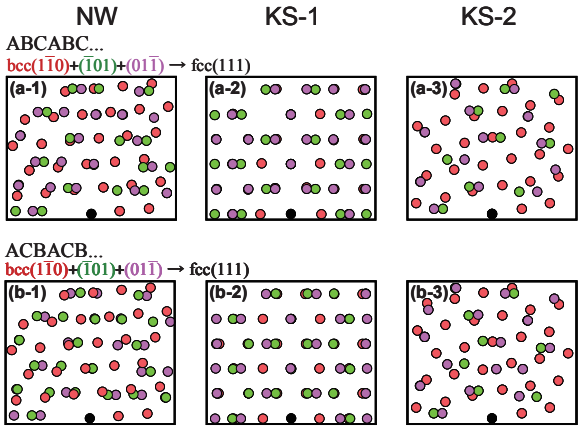

Fig. 8 Schematic diagrams of RHEED patterns simulated for fcc crystals with the atomic stacking sequences of (a) ABCABC… and (b) ACBACB… along fcc[111] transformed from a bcc(111) crystal epitaxially grown on GaAs(111) substrate through atomic displacements from bcc(1$\bar{1}$0), bcc($\bar{1}$01), and bcc(01$\bar{1}$) planes in [(a-1), (b-1)] the NW, [(a-2), (b-2)] the KS-1, and [(a-3), (b-3)] KS-2 relationships. The incident electron beam is parallel to GaAs[1$\bar{1}$0].

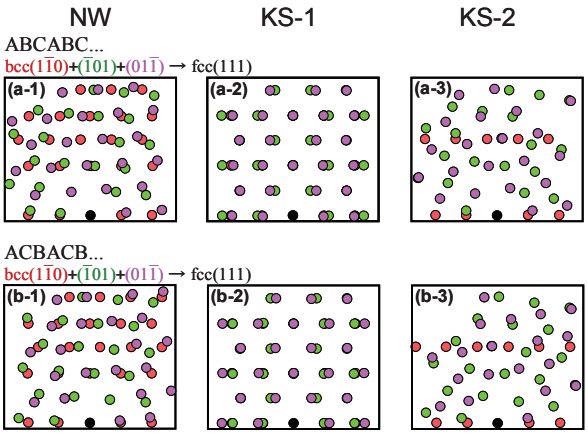

Fig. 9 Schematic diagrams of RHEED patterns simulated for fcc crystals with the atomic stacking sequences of (a) ABCABC… and (b) ACBACB… along fcc[111] transformed from a bcc(111) crystal epitaxially grown on GaAs(111) substrate through atomic displacements from bcc(1$\bar{1}$0), bcc($\bar{1}$01), and bcc(01$\bar{1}$) planes in [(a-1), (b-1)] the NW, [(a-2), (b-2)] the KS-1, and [(a-3), (b-3)] KS-2 relationships. The incident electron beam is parallel to GaAs[11$\bar{2}$].

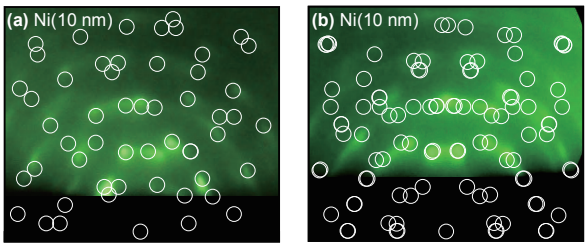

Fig. 10 RHEED patterns observed for a 10-nm-thick Ni film prepared on GaAs(111) substrate [Figs. 1(e-3), 2(e-3)] overlapped with reflection spots simulated for fcc crystals with the stacking sequences of ABCABC... and ACBACB... along fcc[111] transformed though atomic displacements from bcc(1$\bar{1}$0), bcc($\bar{1}$01) and, bcc(01$\bar{1}$) planes in the KS-2 relationship [Figs. 8(a-3), 8(b-3), 9(a-3), 9(b-3)]. The incident electron beam is parallel to (a) GaAs[1$\bar{1}$0] or (b) GaAs[11$\bar{2}$].

sequences of ABCABC... and ACBACB... which are transformed from the bcc(1$\bar{1}$0), bcc($\bar{1}$01), and bcc(01$\bar{1}$) planes in the KS-2 relationship [Figs. 8(a-3), 8(b-3), 9(a-3), 9(b-3)]. The observed RHEED patterns are well matched with the calculated patterns. The crystallographic orientation relationships are thus determined as follows,

$$\mathrm{fcc}(111)[01\bar{1}] \parallel \mathrm{bcc}(1\bar{1}0)[\bar{1}\bar{1}1],$$
$$\mathrm{fcc}(111)[01\bar{1}] \parallel \mathrm{bcc}(\bar{1}01)[\bar{1}1\bar{1}],$$
$$\mathrm{fcc}(111)[01\bar{1}] \parallel \mathrm{bcc}(01\bar{1})[1\bar{1}\bar{1}],$$
$$\mathrm{fcc}(111)[0\bar{1}1] \parallel \mathrm{bcc}(1\bar{1}0)[\bar{1}\bar{1}1],$$
$$\mathrm{fcc}(111)[0\bar{1}1] \parallel \mathrm{bcc}(\bar{1}01)[\bar{1}1\bar{1}],$$
$$\mathrm{fcc}(111)[0\bar{1}1] \parallel \mathrm{bcc}(01\bar{1})[1\bar{1}1].$$

The slide planes and the thickness, where the transformation from bcc to hcp or fcc phase starts, are similar between Co and Ni films. Furthermore, the critical thickness of around 2 nm is almost similar to those observed for Co and Ni films prepared on GaAs(100)[7,8] and GaAs(110)[9] substrates, though the crystallographic orientation relationships of hcp or fcc crystals with respect to bcc crystal are different in the cases of film deposition on GaAs(100), GaAs(110), and GaAs(111) substrates.

Figures 11(a) and 12(a) show the out-of-plane and the in-plane XRD patterns of 40-nm-thick Fe film formed on GaAs(111) substrate. Here, the scattering vector of in-plane XRD is parallel to GaAs[1 $\bar{1}$ 0]. Fe(222)$_{bcc}$ reflection is clearly observed in addition to GaAs (444) reflection in the out-of-plane pattern, whereas Fe(1 $\bar{1}$ 0)$_{bcc}$ reflection is recognized in the in-plane pattern. The out-of-plane and the in-plane XRDs confirm the epitaxial orientation relationship determined by RHEED. Figures 11(b) and (c) show the out-of-plane XRD patterns of 40-nm-thick Co and Ni films, respectively. Reflections from the hcp and the fcc crystals transformed from the bcc structure are not recognized for the Co and the Ni films, since the low index planes of transformed hcp-Co and fcc-Ni crystals are not parallel to the substrate surface. Figures 12(b) and (c) show the in-plane XRD patterns of 40-nm-thick Co and Ni films, respectively. hcp(0002) reflection is observed for the Co film, whereas fcc(111) reflection is recognized for the Ni film. The out-of-plane and the in-plane XRDs confirm that the transformations occur from the bcc(1$\bar{1}$0), bcc($\bar{1}$01) and, bcc(01$\bar{1}$) slide planes which are perpendicular to the substrate surface.

Figures 13(a)–(c) show the pole-figure XRD patterns of 40-nm-thick Fe, Co, and Ni films measured by fixing the diffraction angle of 2θB at 47.5°, where GaAs{220} and hcp{10$\bar{1}$1} reflections are expected to be detectable. The signals with the intensities smaller than 10 cps are subtracted. Figures 13(d) and (e), respectively, show the schematic diagrams of pole-figure XRD patterns simulated for a GaAs(111) substrate and the hcp crystals transformed from bcc structure in the orientation relationships determined by RHEED. The pole-figure XRD patterns of Fe and Ni films show three-fold symmetry, where GaAs{220} reflections are recognized at the tilt angle, α, of 55° and the rotation angles, β, of 120°, 240°, and 0°. The pole-figure XRD pattern of Co film shows six hcp{1$\bar{1}$01} reflections from

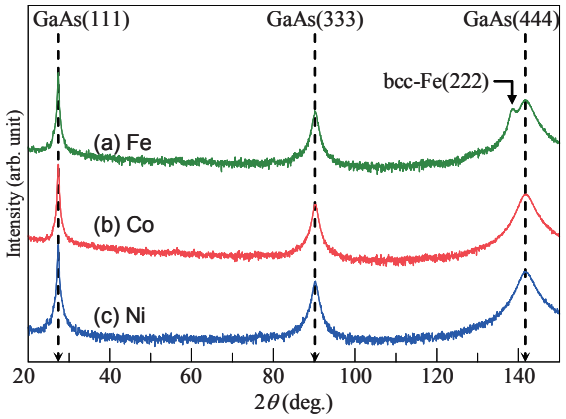

Fig. 11 Out-of-plane XRD patterns measured for (a) Fe, (b) Co, and (c) Ni films of 40 nm thickness formed on GaAs(111) substrates. The intensity is shown in logarithmic scale.

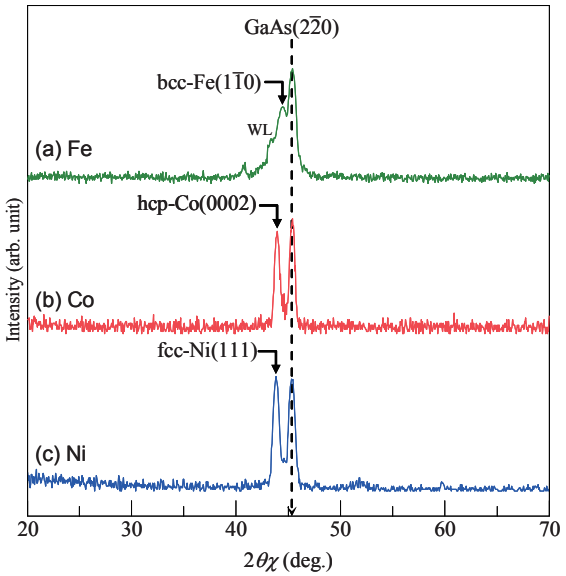

Fig. 12 In-plane XRD patterns of (a) Fe, (b) Co, and (c) Ni films of 40 nm thickness formed on GaAs(111) substrates measured by making the scattering vector parallel to GaAs[1 $\bar{1}$ 0]. The intensity is shown in logarithmic scale.

hcp crystals at the tilt angle, α, of 44°. The hcp reflections are not observed for the Ni film. Figures 14(a)–(c) show the pole-figure XRD patterns of 40-nm-thick Fe, Co, and Ni films measured by fixing the diffraction angle of 2θB at 51.8°, where GaAs{311} and fcc{001} reflections are expected to be detectable. The signals with the intensities smaller than 10 and 1 cps are subtracted for the respective films. Figures 14(d) and (e), respectively, show the schematic diagrams of pole-figure XRD patterns simulated for a GaAs(111) substrate and the fcc crystals transformed from bcc structure in the orientation relationships determined by RHEED. Reflections which originate from the GaAs substrate, are recognized around α = 10°, 32°, and 61° for all the films [Figs. 14(a-2), (b-2), and (c-1)]. Reflections, which originate from the fcc crystals, are observed around α = 9°, 38° and, 51° for the Ni film [Fig. 14(c-1)]. On the other hand, the fcc reflections are not

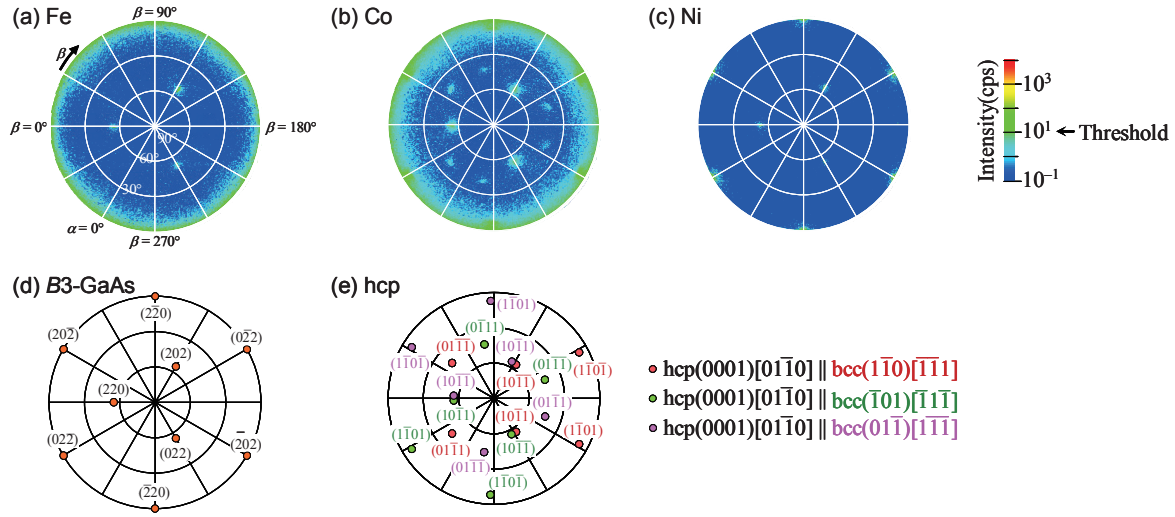

Fig. 13 (a)–(c) Pole-figure XRD patterns measured of (a) Fe, (b) Co, and (c) Ni films of 40 nm thickness prepared on GaAs(111) substrates measured by fixing the diffraction angle of $2\theta B$ at 47.5°, where signals with the intensities smaller than 10 cps are subtracted. [(d), (e)] Schematic diagrams of diffraction patterns simulated for (d) GaAs(111) substrate and (e) hcp crystals transformed from bcc structure in the crystallographic orientation relationships determined by RHEED.

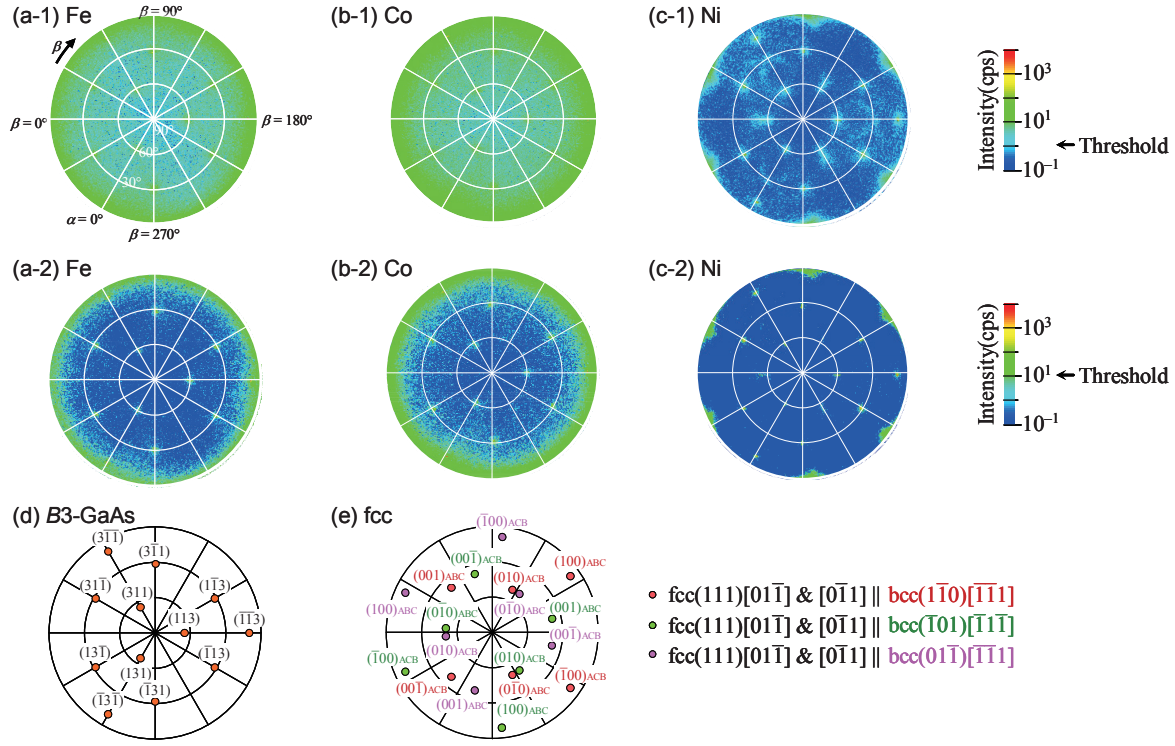

Fig. 14 (a)–(c) Pole-figure XRD patterns of (a) Fe, (b) Co, and (c) Ni films of 40 nm thickness prepared on GaAs(111) substrates measured by fixing the diffraction angle of $2\theta B$ at 51.8°, where signals with the intensities smaller than (a-1)–(c-1) 1 and (a-2)–(c-2) 10 cps are subtracted. [(d), (e)] Schematic diagrams of diffraction patterns simulated for (d) GaAs(111) substrate and (e) fcc crystals transformed from bcc structure in the crystallographic orientation relationships determined by RHEED.

observed for the Co film. Therefore, the bcc crystals in Co and Ni films are apparently transforming into hcp and fcc structures in the orientation relationships determined by RHEED, respectively.

Figure 15(a) shows the magnetization curves of 10-nm-thick bcc-Fe(111) single-crystal film measured by applying the magnetic field along GaAs[11$\bar{2}$], GaAs[10$\bar{1}$], GaAs[2$\bar{1}\bar{1}$], GaAs[1$\bar{1}$0], GaAs[1$\bar{2}$1], or GaAs[0$\bar{1}$1]. The magnetization curves are almost isotropic in the in-plane measurements. The easy magnetization axes of bcc[100], bcc[010], and bcc[001] are not parallel to the substrate surface but 35° canted from the substrate surface. Therefore, the effective easy magnetization directions are considered to be observed along bcc[2$\bar{1}\bar{1}$],

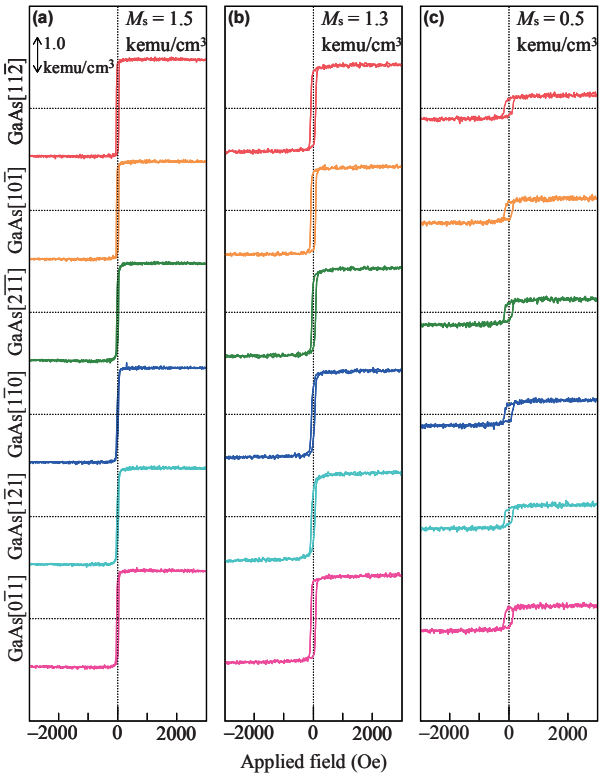

Fig. 15 Magnetization curves measured for (a) Fe, (b) Co, and (c) Ni films of 10 nm thickness prepared on GaAs(111) substrates.

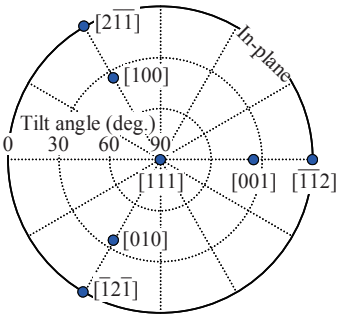

Fig. 16 Pole figure map of bcc(111) single-crystal film showing angles of typical crystallographic planes tilted from the film plane.

bcc[$\bar{1}$2$\bar{1}$], and bcc[$\bar{1}$$\bar{1}$2] due to the demagnetization field, as shown in Fig. 16. As a result, the in-plane magnetic anisotropy seems to show a six-fold symmetry. It should be noted that a contribution to in-plane magnetic anisotropy decreases with increasing the tilt angle, and that the angle of bcc<100> with respect to the film plane is as large as 35°. Therefore, the Fe(111) single-crystal film prepared in the present study is considered to show an almost isotropic in-plane magnetic property. The saturation magnetization value of Fe film is less than that of bulk Fe crystal (1.73 kemu/cm^3). The reason is possibly due to surface oxidation of the film sample with no overcoat.

Figures 15(b) and (c), respectively, show the magnetization curves measured for Co and Ni films of 10 nm thickness. The films, which include hcp and fcc crystals, show almost isotropic magnetic properties. The easy magnetization axes for hcp and fcc crystals are hcp[0001] and fcc<111>. These crystallographic directions correspond to the GaAs[10$\bar{1}$] and [1$\bar{1}$0], respectively. When the distributions of multiple easy axes and the three-fold crystallographic symmetries of Co and Ni films on GaAs(111) substrate are considered, the magnetic anisotropy of whole film will be observed as nearly isotropic. Such nearly isotropic magnetic properties observed in the present study indicate that the magnetocrystalline anisotropies of three hcp-Co and six fcc-Ni crystals are overlapped. The magnetization property is different from the cases of Co and Ni films formed on GaAs(110) substrates where the films consist of variants with two-fold symmetrical distributions[9].

4. Conclusion

Fe, Co, and Ni films are prepared by sputter deposition on GaAs(111) substrates at RT by varying the thickness in a range from 1 to 40 nm. Nucleation of crystal with metastable structure and phase transformation process into stable structure are investigated by RHEED and XRDs. bcc(111) single-crystals are formed in the early stages of film growth of not only Fe but also Co and Ni. The metastable structure is stabilized for Co and Ni films through hetero-epitaxial growth on GaAs(111) substrate. With increasing the thickness beyond 2 nm, the bcc-Co and the bcc-Ni crystals, respectively, start to transform into hcp and fcc structures through atomic displacements in the bcc(1$\bar{1}$0), bcc($\bar{1}$01) and bcc(01$\bar{1}$) close-packed planes.

Acknowledgements A part of this work was supported by Chuo University Grant for Special Research.

References

1) X. -G. Zhang and W. H. Butler: *Phys. Rev. B*, **70**, 172407 (2004).
2) S. Yuasa, A. Fukushima, H. Kubota, Y. Suzuki, and K. Ando: *Appl. Phys. Lett.*, **89**, 042505 (2006).
3) Y. U. Idzerda, W. T. Elam, B. T. Jonker, and G. A. Prinz: *Phys. Rev. Lett.*, **62**, 2480 (1989).
4) S. J. Blundell, M. Gester, J. A. C. Bland, C. Daboo, E. Gu, M. J. Baird, and A. J. R. Ives: *J. Appl. Phys.*, **73**, 5948 (1993).
5) E. Gu, M. Gester, R. J. Hicken, C. Daboo, M. Tselepi, S. J. Gray, J. A. C. Bland, and L. M. Brown: *Phys. Rev. B*, **52**, 14704 (1995).
6) C. S. Tian, D. Qian, D. Wu, R. H. He, Y. Z. Wu, W. X. Tang, L. F. Yin, Y. S. Shi, G. S. Dong, X. F. Jin, X. M. Jiang, F. Q. Liu, H. J. Qian, K. Sun, L. M. Wang, G. Rossi, Z. Q. Qiu, and J. Shi: *Phys. Rev. Lett.*, **94**, 137210 (2005).
7) M. Ohtake, S. Minakawa, and M. Futamoto: *Key Eng. Mater.*, **605**, 478 (2014).
8) S. Minakawa, M. Ohtake, D. Suzuki, N. Inaba, and M. Futamoto: *J. Magn. Soc. Jpn.*, **38**, 185 (2014).
9) T. Soda, S. Minakawa, M. Ohtake, M. Futamoto, and N. Inaba: *IEEE Trans. Magn.*, **51**, 2000904 (2015)
10) S. Minakawa, D. Suzuki, M. Ohtake, N. Inaba, and M. Futamoto: *EPJ Web Conf.*, **75**, 01004 (2013).
11) G. Wasserman: *Arch. Eisenhüttenwesen*, **16**, 647 (1933).
12) Z. Nishiyama: *Sci. Tohoku Univ.*, **23**, 638 (1934).
13) G. Kurdjumov and G. Sachs: *Z. Phys.*, **64**, 325 (1930).

Received Dec. 28, 2015; Accepted Dec. 21, 2017

J. Magn. Soc. Jpn., **42**, 37-40 (2018)

<Paper>

Theoretical study on magnetic tunneling junctions with semiconductor barriers $CuInSe_2$ and $CuGaSe_2$ including a detailed analysis of band-resolved transmittances

K. Masuda[1] and Y. Miura[1,2]

[1]Research Center for Magnetic and Spintronic Materials, National Institute for Materials Science (NIMS), *1-2-1 Sengen, Tsukuba 305-0047, Japan*

[2]Electrical Engineering and Electronics, Kyoto Institute of Technology, *Kyoto 606-8585, Japan*

We study spin-dependent transport properties in magnetic tunneling junctions (MTJs) with semiconductor barriers, Fe/$CuInSe_2$/Fe(001) and Fe/$CuGaSe_2$/Fe(001). By analyzing their transmittances at zero bias voltage on the basis of the first-principles calculations, we find that spin-dependent coherent tunneling transport of Δ_1 wave functions yields a relatively high magnetoresistance (MR) ratio in both the MTJs. We carry out a detailed analysis of the band-resolved transmittances in both the MTJs and find an absence of the selective transmission of Δ_1 wave functions in some energy regions a few eV away from the Fermi level due to small band gaps in $CuInSe_2$ and $CuGaSe_2$.

Key words: magnetic tunneling junctions, magnetoresistance ratios, semiconductors, *ab initio* calculations

1. Introduction

Both high magnetoresistance (MR) ratios and low resistance area products (*RA*) are required for MR devices to realize read heads of ultrahigh-density hard disk drives and Gbit-class spin transfer torque magnetic random access memories (STT-MRAMs) [1]. Although magnetic tunneling junctions (MTJs) with insulator MgO barriers have high MR ratios [2,3], these MTJs also have high *RA*. To reduce the *RA*, many studies have used ultrathin MgO barriers (~1nm), by which relatively low *RA* ~ 1 Ωμm^2 have been obtained [4-6]. However, MR ratios also decrease by reducing the thicknesses of the barriers. In addition, ultrathin barriers do not have sufficient controllability in fabrication processes. On the other hand, current-perpendicular-to-plane giant magnetoresistive (CPP-GMR) devices have quite low *RA* because metallic (not insulating) spacers are sandwiched between ferromagnetic electrodes. Although the MR ratio in CPP-GMR devices is increased up to 82% at room temperature (RT) by using Co-based Heusler alloys as electrodes [7], this value is still insufficient for applications. Recently, Kasai *et al.* used a compound semiconductor $CuIn_{0.8}Ga_{0.2}Se_2$ (CIGS) as a barrier layer of MTJs to achieve high MR ratios and low *RA* [8]. They obtained relatively high MR ratios ~ 40% at RT and low *RA* ranging from 0.3 to 3 Ωμm^2 in the MTJs where CIGS is sandwiched between $Co_2FeGa_{0.5}Ge_{0.5}$ (CFGG) Heusler compounds. Since the barrier thicknesses of these MTJs are twice as those of the above-mentioned MgO-based MTJs with low *RA*, we can expect high controllability in the fabrication processes.

In our previous work [9], we theoretically studied spin-dependent transport properties of two MTJs with different semiconductor barriers, $CuInSe_2$ (CIS) and $CuGaSe_2$ (CGS), to understand the origin of the high MR ratios observed in the CIGS-based MTJs [8]. By analyzing their complex band structures and $\mathbf{k}_{//}$ dependences of the transmittances, we found that spin-dependent coherent transport of Δ_1 wave functions occurs in both the CIS- and CGS-based MTJs, which can explain the high MR ratios in the CIGS-based MTJs. In our present study, we carry out a more detailed analysis of the CIS- and CGS-based MTJs to understand their transport properties more deeply. We provide the values of calculated conductances in both the MTJs for both the parallel and antiparallel magnetization cases of Fe electrodes. We also analyze the band-resolved transmittances in these MTJs, from which we find an absence of the selective transmission of Δ_1 wave functions in some energy regions a few eV away from the Fermi level due to the small band gaps in the CIS and CGS barriers.

2. Method

In this work, we analyzed CIS- and CGS-based MTJs with Fe electrodes: Fe/CIS/Fe(001) and Fe/CGS/Fe(001). Although Heusler alloys were used as electrodes in the experiments on the CIGS-based MTJs, we selected Fe electrodes to understand more simply the transport properties in CIS- and CGS-based MTJs. Since the *a*-axis lengths of CIS (CGS) is close to twice that of bcc Fe, the lattice mismatch between them is considered to be small. We first prepared supercells of Fe/CIS/Fe(001) and Fe/CGS/Fe(001), each of which has two unit cells of CIS (CGS) and one unit cell of Fe on both sides of the CIS (CGS) barrier. The in-plane lattice constant *a* of the supercell was fixed to 0.5782 nm (0.5614 nm), which is an *a*-axis length of the bulk CIS (CGS) [10]. In both the supercells, we optimized all the atomic positions and the distance between the barrier and electrode using the density-functional theory within the generalized

Table 1 Values of conductances per in-plane unit cell area (a^2), RA_P (RA in parallel magnetization states), and MR ratios in (a) Fe/CIS/Fe(001) and (b) Fe/CGS/Fe(001) for different Coulomb interactions U. The majority-spin (minority-spin) conductance in the parallel magnetization state is represented as $G_{P,maj.}$ ($G_{P,min.}$), and the total-spin conductance in the antiparallel magnetization state is represented as $G_{AP,tot}$.

(a) Fe/CIS/Fe(001)

U [eV]	$G_{P,maj.\text{-}spin}$ [e^2/h]	$G_{P,min.\text{-}spin}$ [e^2/h]	$G_{AP,tot}$ [e^2/h]	RA_P [Ωμm^2]	MR ratio [%]
0	1.923×10^{-2}	9.609×10^{-3}	1.885×10^{-2}	0.299	52.9
5	1.662×10^{-2}	4.540×10^{-3}	1.303×10^{-2}	0.408	62.3
10	1.427×10^{-2}	2.500×10^{-3}	9.322×10^{-3}	0.515	79.9

(b) Fe/CGS/Fe(001)

U [eV]	$G_{P,maj.\text{-}spin}$ [e^2/h]	$G_{P,min.\text{-}spin}$ [e^2/h]	$G_{AP,tot}$ [e^2/h]	RA_P [Ωμm^2]	MR ratio [%]
0	1.685×10^{-2}	5.796×10^{-4}	5.854×10^{-3}	0.467	197.7
5	1.168×10^{-2}	2.795×10^{-4}	2.983×10^{-3}	0.680	300.9
10	7.830×10^{-3}	1.643×10^{-4}	1.673×10^{-3}	1.018	377.8

gradient approximation implemented in the Vienna *ab initio* simulation program (VASP) [11),12)]. In the processes of such structure optimizations, we found that the Se layer is always energetically favored as the termination layer of the barrier in both the CIS- and CGS-based supercells. We studied transport properties of both the MTJs at zero bias voltage with the help of the quantum code ESPRESSO [13)]. This code was applied to the quantum open system composed of the above-mentioned supercell attached to the left and right semi-infinite electrodes of bcc Fe. In the present work, we considered the Coulomb interaction U in the Cu 3d states in the barrier. Since the band gap E_g of the barrier increases as U increases, considering U is useful to systematically study the relationship between the band gap and MR ratio. The detailed calculation conditions are the same as our previous study [9)].

Due to the two-dimensional periodicity of our systems in the plane parallel to the layers, the scattering states can be classified by an in-plane wave vector $\mathbf{k}_{//} = (k_x,k_y)$. For each $\mathbf{k}_{//}$ and spin index, we solved scattering equations derived from connection conditions of the wave functions and their derivatives at the boundaries between the supercell and electrodes. Transmittances T were obtained from the transmission amplitudes of the scattering wave functions [14),15)]. We obtained conductances G by substituting the transmittances T into the Landauer formula $G = (e^2/h) \times T$. In this work, we adopted the usual definition of the optimistic MR ratio: MR ratio (%) = $100 \times (G_P\text{-}G_{AP})/G_{AP}$, where G_P (G_{AP}) is the sum of the majority- and minority-spin transmittances averaged over $\mathbf{k}_{//}$ in the Brillouin zone in the case of parallel (antiparallel) magnetization of Fe electrodes. The values of RA in the parallel magnetization states, RA_P, were calculated using the in-plane lattice constants a of the supercells and conductances G_P per in-plane unit cell area (a^2) shown in Table 1.

3. Results and Discussion

Table 1 shows the values of conductances, RA_P, and MR ratios in the CIS- and CGS-based MTJs for different Coulomb interactions U. We obtained MR ratios over 50% (190%) for the CIS-based (CGS-based) MTJs. These relatively high MR ratios are due to the spin-dependent coherent transport of Δ_1 wave functions, which was directly confirmed by the $\mathbf{k}_{//}$ dependences of the transmittances [9)]. We also analyzed complex band structures of the CIS and CGS barriers [9)], which also indicated selective transmission of Δ_1 wave functions. The RA values in both the MTJs are much smaller than those of the well-known MgO-based MTJs [9)], which originates from the small band gaps in CIS and CGS barriers.

From Table 1, we see that the MR ratio and RA increase as the Coulomb interaction U increases in both the MTJs. As we mentioned in the previous section, the band gap $E_{g,CIS}$ ($E_{g,CGS}$) of CIS (CGS) increases by increasing U from 0 to 10 eV. Actually, we confirmed that $E_{g,CIS}$ = 0.31, 0.39, and 0.42 eV ($E_{g,CGS}$ = 0.71, 0.84, and 0.93 eV) for U = 0, 5, and 10 eV, respectively, by analyzing the local density of states of Fe/CIS/Fe(001) and Fe/CGS/Fe(001) [16)]. Thus, it is found that a semiconductor barrier with a larger band gap gives a higher MR ratio and a higher RA. This is also supported by the fact that the CGS-based MTJ has a higher MR ratio and a higher RA than the CIS-based one for the same value of U (see Table 1). From the viewpoint of tunneling transport, such an increase in E_g corresponds to an increase in the barrier height $\varphi = E_g - E_F$, where E_F is the Fermi level of the system. Using the above-mentioned band gaps ($E_{g,CIS}$ and $E_{g,CGS}$) and the Fermi levels in the Fe/CIS/Fe(001) and Fe/CGS/Fe(001), we obtained the following values of barrier heights: φ_{CIS} = 0.080, 0.100, and 0.111 eV (φ_{CGS} = 0.263, 0.301, and 0.330 eV) for U = 0, 5, and 10 eV, respectively. Note here that the transmittance through the barrier is approximately

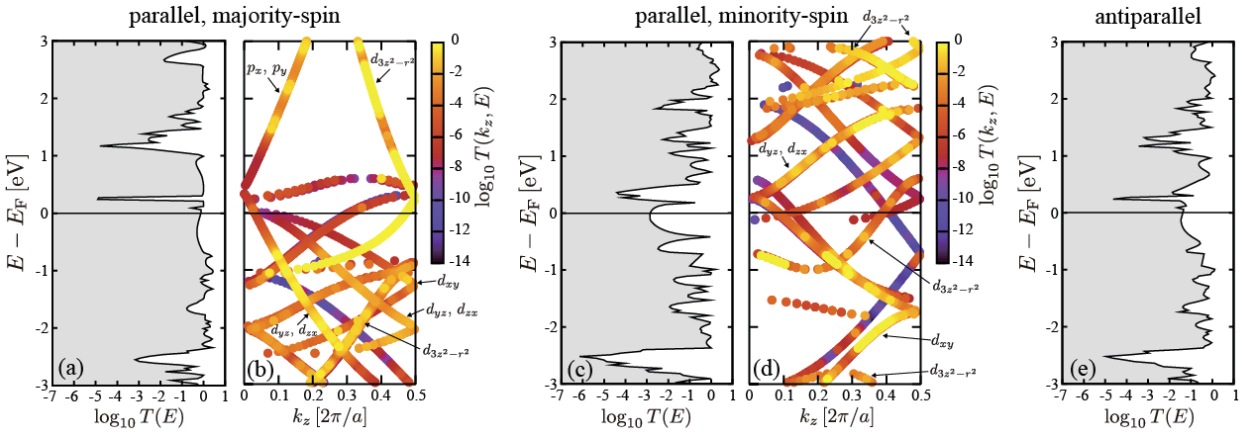

Fig. 1 Transmittances at $\mathbf{k}_{//}$=(0,0) in Fe/CGS/Fe(001) MTJ with U = 5 eV. (a) The energy dependence of the total transmittance and (b) the band-resolved transmittance in the [001] direction for the majority-spin channel in the parallel magnetization state. (c) and (d) The same as (a) and (b) but for the minority-spin channel in the parallel magnetization state. (e) The energy dependence of the total transmittance in the antiparallel magnetization state.

proportional to exp(-2κd), where $\kappa = (2m\varphi/\hbar^2 - |\mathbf{k}_{//}|^2)^{1/2}$ and d is the barrier thickness [17]. Therefore, increasing E_g (i.e., increasing φ) in the semiconductor barrier has roughly the same effect as increasing the barrier thickness d, both of which sharpen the tunneling feature and enhance the MR ratio.

In order to find characteristic features in the transmittances of the CIS- and CGS-based MTJs, we analyzed energy- and band-resolved transmittances at $\mathbf{k}_{//}$=(0,0) in the CGS-based MTJs [18]. Here, we show the results only for the CGS case, but qualitatively the same results were also obtained in the CIS case. Figures 1(a) and 1(c) show the energy-resolved transmittances for majority-spin and minority-spin channels, respectively, in the parallel magnetization state of the electrodes. At the Fermi level (E=E_F), the transmittance in the majority-spin channel is more than one order higher than that in the minority-spin channel. In Fig. 1(e), we also show the energy-resolved transmittance in the antiparallel magnetization state of the electrodes. The transmittance at the Fermi level is one order smaller than the majority-spin transmittance in the parallel magnetization case. From all these behaviors in the transmittances, we can understand naturally the high MR ratio (~300%) in this system (see Table 1). Figures 1(b) and 1(d) show the majority-spin and minority-spin transmittances resolved into each (k_z,E) contribution on the band structures of the Fe electrode. The energy-gap region is -0.539 eV $\leqq$ E-E_F $\leqq$ 0.301 eV for the CGS with U = 5 eV in our calculations [19]. In the majority-spin channel [Fig. 1(b)], the Δ_1 band mainly from $d_{3z^2-r^2}$ state gives high values of transmittance in the energy-gap region. Such a selective transmission of the Δ_1 wave functions is consistent with small imaginary wave vectors in the Δ_1 state obtained in our previous work [see Fig. 2(b) of Ref. 9]. The selective transmission of Δ_1 wave functions also occurs outside of the energy-gap region (0.3 eV $\lesssim$ E-E_F $\lesssim$ 1.1 eV and -1.0 eV $\lesssim$ E-E_F $\lesssim$ -0.54 eV), which is because the conduction and valence bands of CGS in these regions have Δ_1 symmetry. In some other regions (e.g., a region around E-E_F = 1.5 eV and that around E-E_F = 2.2 eV, etc.), the Δ_5 band mainly from p_x and p_y states gives higher transmittances than the Δ_1 band, which is in contrast to the case of the band-insulator barrier, Fe/$MgAl_2O_4$/Fe(001), where the selective transmission of the Δ_1 wave functions persists to high energies [see Fig. 3(b) of Ref. 20 for comparison]. Note again that such energy regions are outside of the band gap of the CGS barrier. Thus, in these regions, tunneling transport is not possible and selective transmission of Δ_1 wave functions do not necessarily occur. We confirmed that the conduction bands of CGS in these regions include Δ_5 component, which is consistent with the high transmittances of Δ_5 states (p_x and p_y states) mentioned above. The similar feature can also be seen in lower-energy regions with E-E_F < -1 eV, where the Δ_5 and Δ_2 bands from d_{yz} (d_{zx}) and d_{xy} states give relatively high transmittances. This is also supported by the fact that valence bands of CGS in these regions contain Δ_5 and Δ_2 components. Around the Fermi level in the minority-spin channel shown in Fig. 1(d), the Δ_5 and Δ_2 bands give similar values of transmittance as the $d_{3z^2-r^2}$-based Δ_1 band, i.e., clear selective transmission of Δ_1 wave functions does not occur unlike the majority-spin case. Since the in-plane lattice constant of CGS is set to be twice that of the bcc Fe as mentioned above, the original bands of bcc Fe is folded in the $\mathbf{k}_{//}$ Brillouin zone. Usually, in such a case, the folded minority-spin Δ_1 band crossing the Fermi level provides relatively large transmittances and decreases the MR ratio, as discussed in previous studies on Fe/$MgAl_2O_4$/Fe(001) [21),22]. However, in our present case, the folded minority-spin Δ_1 band crossing the Fermi

level does not give large transmittance compared to the other Δ_5 and Δ_2 bands and therefore does not decrease MR ratio drastically. The configurations of interfacial Se atoms in Fe/CGS/Fe(001) do not have fourfold rotational symmetry along the *c*-axis of the supercell, which is clearly different from the configurations of interfacial O atoms in Fe/$MgAl_2O_4$/Fe(001). Thus, in the case of Fe/CGS/Fe(001), although the bands are formally folded in the $\mathbf{k}_{//}$ Brillouin zone, the folded minority-spin band crossing the Fermi level has a different character from that of Fe/$MgAl_2O_4$/Fe(001), which may be the reason for the ineffectiveness of the band-folding effect in Fe/CGS/Fe(001).

The present analysis focused only on the transmittances at zero bias voltage. On the other hand, in actual experiments, a small bias voltage is applied to MTJs to obtain electron transmission. Since the band gaps in the present study are small ($E_{g,CIS} \lesssim 0.42$ eV and $E_{g,CGS} \lesssim 0.93$ eV), such a bias voltage gives a non-negligible spatial gradient in the semiconductor-barrier potentials, which can affect the transport properties in the CIS- and CGS-based MTJs. However, the small values of theoretical band gaps are artifacts due to the generalized gradient approximation used in this study. Although the present band gaps are small, we adopted them as alternatives of experimental band gaps of CIS and CGS ($E_{g,CIS} = 1.0$ eV and $E_{g,CGS} = 1.7$ eV), on which the effect of the spatial gradient from the small bias voltage is not so large.

4. Summary

We investigated spin-dependent transport properties of magnetic tunneling junctions with semiconductor barriers, Fe/CIS/Fe(001) and Fe/CGS/Fe(001). We clarified that spin-dependent coherent tunneling transport of Δ_1 wave functions leads to relatively high MR ratios in both the MTJs. From a detailed analysis of the band-resolved transmittances in both the MTJs, we found an absence of the selective transmission of Δ_1 wave functions in some energy regions a few eV away from the Fermi level, which is a characteristic feature of the MTJs with small band gaps in the barrier layers.

Acknowledgements The authors would like to thank K. Hono, S. Kasai, and K. Mukaiyama for giving us useful information about experimental results on the CIGS-based MTJs. KM also thanks K. Nawa for valuable discussion on theoretical aspects. This work was in part supported by Grants-in-Aid for Scientific Research (S) (Grant No. 16H06332) and (B) (Grant No. 16H03852) from the Ministry of Education, Culture, Sports, Science and Technology, Japan, by NIMS MI2I, and also by the ImPACT Program of Council for Science, Technology and Innovation, Japan.

References

1) B. Dieny, R. B. Goldfarb, and K. J. Lee: *Introduction to magnetic random-access memory* (John Wiley & Sons, 2016).
2) S. S. P. Parkin, C. Kaiser, A. Panchula, P. M. Rice, B. Hughes, M. Samant, and S.-H. Yang: *Nat. Mater.* **3**, 862 (2004).
3) S. Yuasa, T. Nagahama, A. Fukushima, Y. Suzuki, and K. Ando: *Nat. Mater.* **3**, 868 (2004).
4) Y. S. Choi, Y. Nagamine, K. Tsunekawa, H. Maehara, D. D. Djayaprawira, S. Yuasa, and K. Ando: *Appl. Phys. Lett.* **90**, 012505 (2007).
5) S. Isogami, M. Tsunoda, K. Komagaki, K. Sunaga, Y. Uehara, M. Sato, T. Miyajima, and M. Takahashi: *Appl. Phys. Lett.* **93**, 192109 (2008).
6) H. Maehara, K. Nishimura, Y. Nagamine, K. Tsunekawa, T. Seki, H. Kubota, A. Fukushima, K. Yakushiji, K. Ando, and S. Yuasa: *Appl. Phys. Express* **4**, 033002 (2011).
7) J. W. Jung, Y. Sakuraba, T. T. Sasaki, Y. Miura, and K. Hono: *Appl. Phys. Lett.* **108**, 102408 (2016).
8) S. Kasai, Y. K. Takahashi, P.-H. Cheng, Ikhtiar, T. Ohkubo, K. Kondou, Y. Otani, S. Mitani, and K. Hono: *Appl. Phys. Lett.* **109**, 032409 (2016).
9) K. Masuda and Y. Miura: *Jpn. J. Appl. Phys.* **56**, 020306 (2017).
10) J. E. Jaffe and A. Zunger: *Phys. Rev. B* **29**, 1882 (1984).
11) G. Kresse and J. Furthmüller: *Phys. Rev. B* **54**, 11169 (1996).
12) G. Kresse and D. Joubert: *Phys. Rev. B* **59**, 1758 (1999).
13) S. Baroni, A. Dal Corso, S. de Gironcoli, and P. Giannozzi, s: Quantum ESPRESSO package. For more information, see http://www.pwscf.org.
14) H. J. Choi and J. Ihm: *Phys. Rev. B* **59**, 2267 (1999).
15) A. Smogunov, A. Dal Corso, and E. Tosatti: *Phys. Rev. B* **70**, 045417 (2004).
16) Note that these values of band gaps are different from those of bulk CIS and CGS shown in Ref. 9, which is due to the hybridization between Se and Fe states at the interfaces of Fe/CIS/Fe(001) and Fe/CGS/Fe(001) supercells. These band gaps are more suitable than the bulk ones for understanding the transport properties in Fe/CIS/Fe(001) and Fe/CGS/Fe(001).
17) J. M. MacLaren, X.-G. Zhang, and W. H. Butler: *Phys. Rev. B* **56**, 11827 (1997).
18) Here, we focus only on the transmittances at $\mathbf{k}_{//} = (0,0)$, since these components provide dominant contributions to the total transmittance. Note, however, that MR ratios and *RA* are calculated from the transmittances integrated over $\mathbf{k}_{//}$ at the Fermi level ($E=E_F$).
19) In the case of CIS with $U = 5$ eV, the energy-gap region is $-0.290 \text{ eV} \leqq E-E_F \leqq 0.100$ eV.
20) K. Masuda and Y. Miura: *Phys. Rev. B* **96**, 054428 (2017).
21) Y. Miura, S. Muramoto, K. Abe, and M. Shirai: *Phys. Rev. B* **86**, 024426 (2012).
22) H. Sukegawa, Y. Miura, S. Muramoto, S. Mitani, T. Niizeki, T. Ohkubo, K. Abe, M. Shirai, K. Inomata, and K. Hono: *Phys. Rev. B* **86**, 184401 (2012).

Received Oct. 18, 2017; Accepted Jan. 18, 2018

J. Magn. Soc. Jpn., **42**, 41-48 (2018)

<Paper>

Evaluation of dispersibility in liquid and AC magnetization properties of polyion complex-coupled magnetic nanoparticles

Guannan Shi, Suko Bagus Trisnanto, Keita Nakai*, Shin-ichi Yusa*, Tsutomu Yamada, Satoshi Ota**, and Yasushi Takemura

Department of Electrical and Computer Engineering, Yokohama National University,
79-5 Tokiwadai, Hodogaya-ku, Yokohama 240-8501, Japan
*Department of Applied Chemistry, Graduate School of Engineering, University of Hyogo,
2167 Shosha, Himeji, Hyogo 671-2280, Japan
**Department of Electrical and Electronic Engineering, Shizuoka University,
3-5-1 Johoku, Naka-ku, Hamamatsu 432-8501, Japan

Medical applications such as those using magnetic nanoparticles (MNPs) for hyperthermia and magnetic particle imaging (MPI) require suitably designed particles with distinct characteristics. However, it is challenging to develop such particles with a high degree of biocompatibility. In this study, a cationic diblock copolymer ($PMPC_{100}$-*b*-$MMAPTAC_{100}$: $P_{100}M_{100}$) composed of poly(2-(methacryloyloxy)ethyl phosphorylcholine) (PMPC) and poly(3-(methacryloylamino)propyl trimethylammonium chloride) (PMAPTAC) was synthesized via a controlled radical polymerization technique to obtain particles with high biocompatibility and antithrombogenicity. Magnetic polyion complex (PIC) aggregate (M-300/$P_{100}M_{100}$) is an aggregate of magnetic Fe_3O_4 nanoparticles (M-300), in which their anionic surface is electrostatically coated with cationic $PMPC_{100}$-*b*-$MMAPTAC_{100}$ ($P_{100}M_{100}$). We investigated the stability of the magnetic PIC aggregate in an ionic solution by evaluating the relationship between the particle diameter and salt concentration. We then estimated the intrinsic loss power (ILP) from the areas of the alternating current (AC) hysteresis loops and measured the AC magnetization of the magnetic PIC aggregate. The peak frequencies from the Brownian relaxation of M-300 and M-300/$P_{100}M_{100}$ were 9 kHz and 245 Hz, respectively. When the third harmonic was evaluated for use in MPI, the signal intensity was found to be comparable to that of M-300 in a fixed state.

Keywords: magnetic nanoparticles, hyperthermia, magnetic particle imaging (MPI), biocompatibility, polyion complex (PIC), magnetic relaxation

1. Introduction

In recent years, several medical treatment applications have come to require magnetic nanoparticles with high biocompatibility. Research into magnetic nanoparticles coated with polyion complex (PIC) organic materials is ongoing due to their wide clinical applicability[1–3], and the sizes and characteristics of core-shell structures of PIC micelles have rendered them useful as carriers of oligonucleotides and plasmid DNA for human gene therapy[4].

In the medical field, magnetic nanoparticles (MNPs) are employed in a variety of applications including magnetic hyperthermia[5] and magnetic particle imaging (MPI)[6,7]. Magnetic relaxation loss is one of the heating mechanisms of MNPs used in the research of hyperthermia. In this regard, superparamagnetism in MNPs results from two distinct magnetic relaxation processes. The first occurs through a type of particle rotation called Brownian relaxation, whereas the other occurs through a magnetic moment rotation referred to as Néel relaxation. The Brownian (τ_B) and Néel (τ_N) relaxation times can be defined as follows[8,9]:

$$\tau_B = \frac{3\eta V_H}{k_B T}, \tag{1}$$

$$\tau_N = \tau_0 \exp\left(\frac{KV_M}{k_B T}\right), \tag{2}$$

where η is the viscosity, V_H is the hydrodynamic MNP volume, τ_0 is the attempt time of ~10^{-9} s associated with gyromagnetic procession, K is the magnetic anisotropic constant, $V_M$is the core particle volume, $k_B$is Boltzmann's constant (1.38×10^{-23} J/K), and T is the temperature in Kelvin[7]. In theory, Brownian and Néel relaxations occur in parallel, and the effective relaxation time, τ, can be expressed as[8]:

$$\frac{1}{\tau} = \frac{1}{\tau_B} + \frac{1}{\tau_N}. \tag{3}$$

The effective frequency for heat dissipation can be estimated from measuring the dependency of the intrinsic loss power (ILP) relative to the frequency. The ILP is the intrinsic heat dissipation independent of the applied field and is calculated from the specific loss power (SLP)[10], which is defined as:

Table 1. Concentration calculated from catalog data of M-300. Values in parentheses were used in calculations in this study.

	H_2O	Fe_3O_4	RSO_3Na	M-300
Composition (wt%)	55–66 (55)	30–40 (40)	5	100
Specific gravity (g/mL)	0.998 (1)	4.8–5.1 (5.1)	1	1.3–1.4 (1.4)
CAS No.	–	1309-38-2	1106-21-0	–
M.W. (g/mol)	–	231.53	298.42	–
Concentration (g/L)	–	560	70.0	–

$$\mathrm{SLP} = \frac{\Delta T}{\Delta t}\frac{c}{m_{Fe}}, \tag{4}$$

where $\Delta T/\Delta t$ is the time rate of change of temperature, c is the heat capacity of the fluid per unit mass of fluid, and m_{Fe} is the iron mass in the fluid per unit mass of fluid. Then, the ILP is given as[10]:

$$\mathrm{ILP} = \frac{SLP}{H^2 f}, \tag{5}$$

where H is the amplitude of the magnetic field.

In this study, we synthesized a diblock copolymer ($PMPC_{100}$-*b*-$PMAPTAC_{100}$:$P_{100}M_{100}$) composed of biocompatible poly(2-(methacryloyloxy)ethyl phosphorylcholine) (PMPC) and cationic poly(3-(methacryloylamino)propyl trimethylammonium chloride) (PMAPTAC) via a controlled radical polymerization technique. PMPC shows excellent biocompatibility and antithrombotic properties[4] because it has hydrophilic pendant phosphorylcholine groups, which are structurally identical to the hydrophilic surfaces of biological membranes. In our study, we characterized the chemical structure of the diblock copolymer and evaluated the dependence of particle size on salt concentration to confirm its stability in an ionic solution. We then measured the AC magnetization properties of a magnetic PIC aggregate (M-300/$P_{100}M_{100}$) comprising anionic Fe_3O_4 nanoparticles (M-300) electrostatically coated with cationic $P_{100}M_{100}$. Finally, we calculated the ILP and MPI signals from the AC hysteresis loops and compared the results with those of unmodified M-300.

2. Materials and Methods

2.1 Materials

The characteristics of M-300 used for particle synthesis in this study, along with its catalog data, are shown Table 1. As calculated from the catalog data, the concentrations of Fe_3O_4 and RSO_3Na in M-300 were 560 and 70.0 g/L, respectively. M-300 was subjected to dynamic light scattering (DLS), and the zeta potential of the solution diluted 100 times in pure water was measured (Fig. 1). After dilution, the concentrations of Fe_3O_4 (C_F) and RSO_3Na (C_S) were 5.60 and 0.700 g/L, respectively. In this case, the hydrodynamic radius (R_h) obtained from the DLS measurement was 21.2 nm and the zeta potential was −52.0 mV. M-300 had a very low scattering light intensity (SI) when diluted 1,000,000 times; although R_h was not calculated at this dilution level, it remained constant to 100,000 times dilution (C_F = 0.00560 g/L). In contrast, the zeta potential of the 10,000-fold diluted solution (C_S = 0.00700 g/L) was −47.4 mV. Overall, it is clear that M-300 exhibited high stability, as evidenced by constant value of R_h versus dilution in pure water.

$PMPC_{100}$-CTA (M_n = 29800, M_w/M_n = 1.08 (acetate buffer as the eluent), 1.50 g, 0.0503 mmol), MAPTAC (1.11 g, 5.03 mmol), and V-501 (4.59 mg, 0.0201 mmol) were dissolved in 5.03 mL of pure water, and the mixture was degassed by purging with Ar gas for 30 min. Polymerization was performed at 343.15 K for 5 h, and the diblock copolymer ($PMPC_{100}$-*block*-PMAPTAC, $P_{100}M_{100}$, 2.36 g, 90.4%) was recovered by freeze-drying after the reaction mixture was dialyzed against pure water for 2 days. The M-300/$P_{100}M_{100}$ complex was prepared by adding a $P_{100}M_{100}$ aqueous solution to an M-300 aqueous solution so that the mixing ratio (R = $P_{100}M_{100}$/M-300, v/v) was 0.0739. The concentration of Fe_3O_4 was 5.31 g/L (3.84 mg-Fe/mL) in the M-

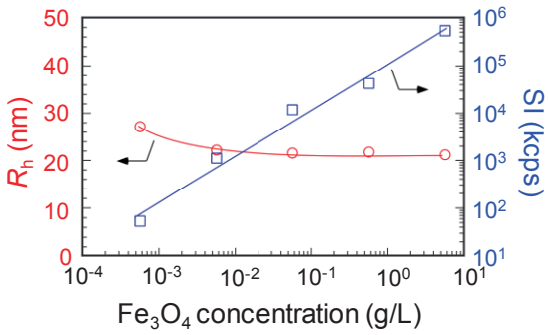

Fig. 1 Dependence of R_h (open circles) and SI (open squares) on concentration of Fe_3O_4 in water-based M-300.

Table 2. Degree of polymerization (DP), number-average molecular weight (M_n), and molecular weight distribution (M_w/M_n) of $P_{100}M_{100}$.

DP(theo)[a]	M_n(theo)[a]	DP(NMR)[b]	M_n(NMR)[b]	M_w/M_n[c]
99	51,700	100	51,900	1.10

[a]Theoretical values estimated from the feed ratio and conversion. [b]Estimated from ^{1}H NMR. [c]Estimated from GPC.

300/$P_{100}M_{100}$ complex. For comparison, we also diluted water-based Fe_3O_4-containing sodium α-olefin sulfonate-coated nanoparticles, which are commercially distributed as M-300 by Sigma Hi-Chemical Inc. (Chigasaki, Kanagawa, Japan), 100 times in pure water to give a concentration of 5.31 g/L. The core diameter was 11 ± 3 nm, which is identical to that of M-300/$P_{100}M_{100}$.

2.2 Methods

The physical properties of M-300/$P_{100}M_{100}$ were evaluated with nuclear magnetic resonance spectroscopy (NMR: Bruker, DRX500), dynamic light scattering (DLS), zeta potential measurements (Malvern, Zetasizer nanoZS), and transmission electron microscopy (TEM: Jeol, JEM-2100). During this process, we also evaluated the NaCl concentration dependence of M-300/$P_{100}M_{100}$.

The AC hysteresis loops were measured in the frequency range of 100 Hz–100 kHz at a field intensity of 4 kA/m, and the DC hysteresis loops were measured using a vibrating sample magnetometer (VSM: Toei Kogyo, TEM-WFR7) at 298.15 K. For these measurements, 0.2 mL of the sample encapsulated in cylindrical tubes with a diameter of 10 mm were used. MNPs dispersed in water were used as the liquid sample, and MNPs fixed with epoxy bonds were used as the solid sample. The ILP and MPI values of the samples were calculated, and the results were compared with those of M-300.

3. Results and Discussion

3.1 Synthesis, structure, and characterization

NMR spectroscopy was used to identify the chemical structure of $P_{100}M_{100}$ synthesized by the above method, and it was confirmed that the peaks of PMPC and PMAPTAC $P_{100}M_{100}$ were present (Fig. 2). On the basis of the consumption of the vinyl group before and after polymerization, the degree of polymerization (DP (theo)) of the monomer MAPTAC was determined to be 99. In addition, we determined that the degree of polymerization (DP (NMR)) from the integrated intensity ratio of the PMPC and PMAPTAC peaks in the NMR spectrum of $P_{100}M_{100}$ after recovery was 100. The molecular weight distribution (M_w/M_n) obtained from gel permeation chromatography (GPC) was as narrow as 1.10, and a structure-controlled polymer was obtained (Table 2). We therefore concluded that $P_{100}M_{100}$ was synthesized by the cationic monomer MAPTAC and the betaine monomer MPC, as observed from the ^{1}H NMR spectrum. We also confirmed the mixing ratio

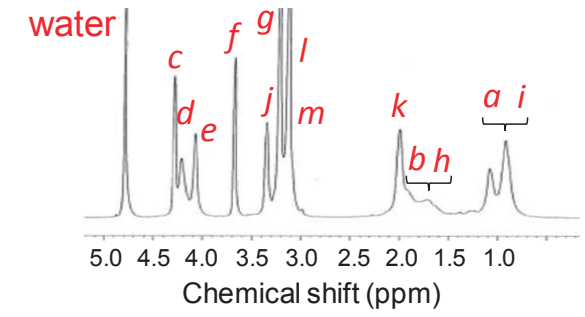

Fig. 2 ^{1}H NMR spectrum measured for $P_{100}M_{100}$ in D_2O at room temperature. The symbols indicate the states of ^{1}H corresponding to each peak of the spectrum.

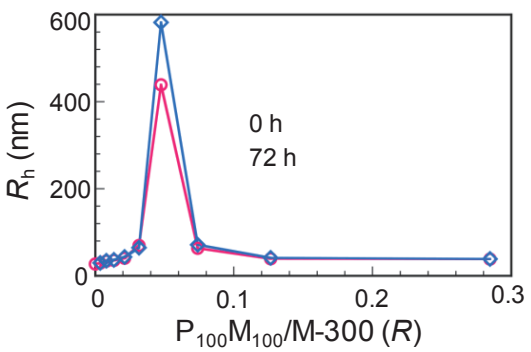

Fig. 3 Relationship of R_h with mixing ratio of M-300/$P_{100}M_{100}$ immediately after preparation and 72 h after preparation in pure water.

dependence of the M-300/$P_{100}M_{100}$ complex. The concentration of M-300 anions was identical to the concentration of the anionic surfactant sodium α-olefin sulfonate in solution, although the exact concentration of the anions is unknown. Therefore, in order to confirm the neutralization point of the complex, we investigated the changes in R_h and the zeta potential of the aggregate with respect to the mixing ratio of M-300 and P_{100} M_{100} in the complex. Figure 3 plots the R_h values obtained by DLS measurement versus the mixing ratio (R = $P_{100}M_{100}$ / M-300, v/v) of M-300 and P_{100} M_{100} in pure water after 72 h. When $P_{100}M_{100}$ was mixed with M-300, R_h increased as the value of R increased until it reached a maximum at R = 0.0474. Increasing R beyond this point decreased both R_h and SI. In addition, in M-300/$P_{100}M_{100}$ with R = 0.0474, the SI decreased sharply after 72 h, suggesting that precipitation had occurred.

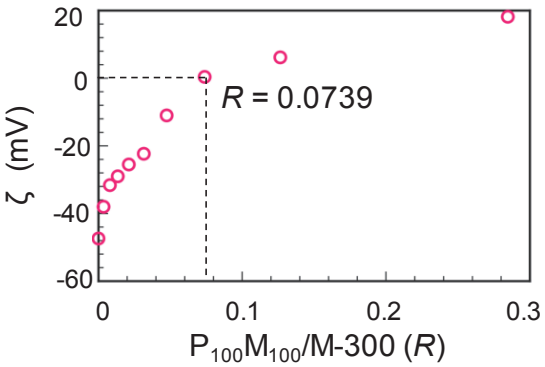

Fig. 4 Zeta potential for mixing ratio (R = $P_{100}M_{100}$/M-300, v/v) of water-based M-300/$P_{100}M_{100}$.

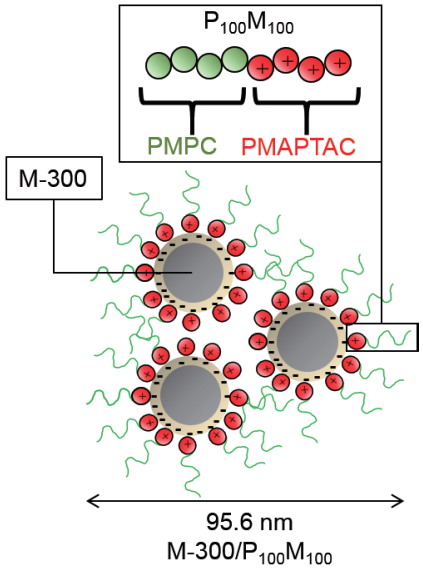

Fig. 5 Schematic representation of M-300/$P_{100}M_{100}$ preparation.

By comparison, we concluded that the aggregates were stable since M-300/$P_{100}M_{100}$, other than that for R = 0.0474, neither precipitated nor demonstrated a change in R_h over the course of 72 h. Figure 4 shows the zeta potential versus the mixing ratio of the synthesized M-300/$P_{100}M_{100}$ after 96 h. The M-300/$P_{100}M_{100}$ with R = 0.0474 precipitated; thus, the zeta potential of the supernatant was measured. As the R value of M-300/$P_{100}M_{100}$ increased, the zeta potential also increased as the solution concentration of $P_{100}M_{100}$ increased. Previously, it was thought that the charge would neutralize with a zeta potential of zero for M-300/$P_{100}M_{100}$ with R = 0.0739. It was also thought that larger absolute values of the zeta potential indicated stronger repulsive forces between the particles and hence higher particle stability. However, the results of this study indicate that the surface charges were neutralized to completion, and they were stably dispersed due to steric hindrance by the polymer material outside the particles. In this case, the Na^+ cations from sodium tetradecane sulfonate and the Cl^- anions from $P_{100}M_{100}$ were ionically bonded in water, while the N^+ cations from $P_{100}M_{100}$ and the O^- anions from tetradecane sulfonate were electrostatically bonded. In this way, the magnetic PIC aggregate was synthesized as shown in Fig. 5.

Moreover, we confirmed that the surface of the M-300/$P_{100}M_{100}$ complex (R = 0.0739) was covered by a PMPC shell based on the dispersion stability (i.e., the R_h and SI) versus the NaCl concentration in solution (Fig. 6). The R_h and SI values of M-300/$P_{100}M_{100}$ were independent of the NaCl concentration ([NaCl]); however, the R_h and SI values of M-300 increased when [NaCl] was increased to 0.2 M (mol/L). These results indicate that M-300/$P_{100}M_{100}$ was covered by a PMPC shell since the dispersion stability improved upon complexation, which was synthesized with $P_{100}M_{100}$. Further, aggregates appeared in M-300 for [NaCl] = 0.2 M when left overnight. In contrast, M-300/$P_{100}M_{100}$ did not precipitate but was maintained as a stable dispersion. For a NaCl concentration of 0.2 M, specific quantities of M-300/$P_{100}M_{100}$ and M-300 aqueous solutions were

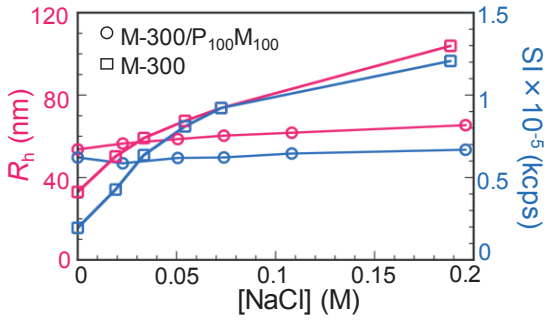

Fig. 6 Change in R_h and SI with respect to NaCl concentration of M-300 (open squares) and M-300/$P_{100}M_{100}$ (open circles).

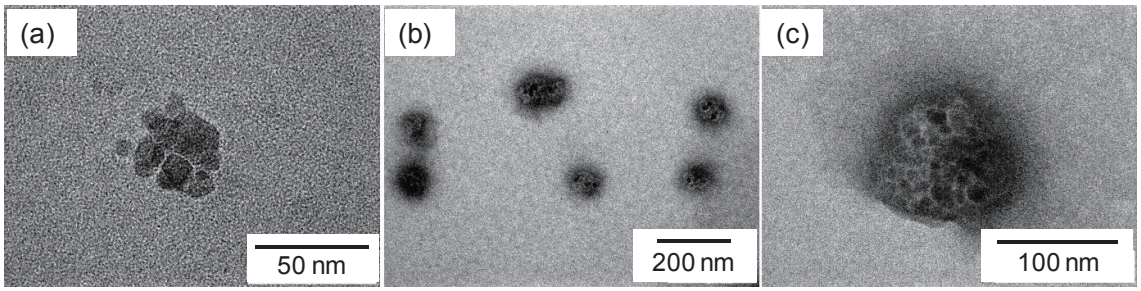

Fig. 7 TEM images of (a) M-300 and (b, c) M-300/$P_{100}M_{100}$. From TEM image, it was confirmed that M-300 and M-300/$P_{100}M_{100}$ are aggregates of Fe_3O_4.

allowed to stand still for one week to confirm the changes over time. The R_h value of M-300/$P_{100}M_{100}$ was 63.2 nm and remained unchanged over time, whereas that of M-300 increased to 144 nm. Furthermore, since M-300 precipitated by salting-out, we concluded that the PMPC shell of the complex inhibited this process. Based on these results, we inferred that as the sodium concentration in the solvent increased, the sodium ions on the M-300 surface ionically bonded with the chlorine ions, resulting in aggregation. However, the magnetic PIC aggregate surface was not affected by the salt concentration since it was charge-neutralized. From this property, we conclude that magnetic PIC aggregates can be stably dispersed in biological bodies.

Figure 7 shows the TEM images of M-300 and M-300/$P_{100}M_{100}$. On this basis, we confirmed that M-300 was an aggregate of Fe_3O_4 (Fig. 7 (a)) and that M-300/$P_{100}M_{100}$ was the same aggregate as M-300 (Fig. 7 (b, c)). Therefore, we concluded that M-300/$P_{100}M_{100}$ was packed with anionic M-300 by the cationic diblock copolymer $P_{100}M_{100}$, and the estimated radius of M-300/$P_{100}M_{100}$ was ~50 nm. Moreover, the hydrodynamic radii of M-300 and M-300/$P_{100}M_{100}$ were 20.2 nm and 47.8 nm, respectively, as determined by DLS measurements (Fig. 8). The characteristics of M-300 and M-300/$P_{100}M_{100}$ are listed in Table 3.

Table 3. Characterization of M-300 and M-300/$P_{100}M_{100}$.

	R_h (nm)	SI (kcps)	PDI
M-300	20.2	4.21×10^5	0.120
M-300/$P_{100}M_{100}$	47.8	1.70×10^6	0.119

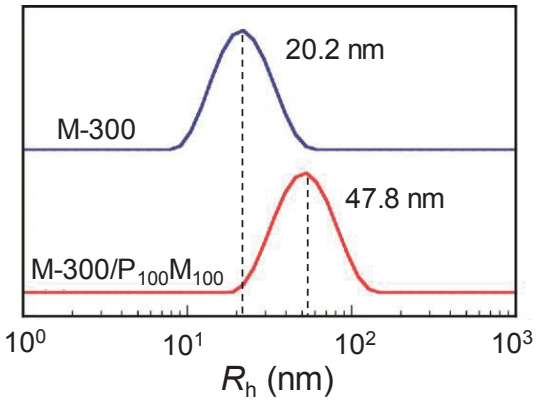

Fig. 8 Hydrodynamic radii of M-300 and M-300/$P_{100}M_{100}$.

3.2 Magnetic properties

Figure 9 shows the DC hysteresis loops of M-300 and M-300/$P_{100}M_{100}$ for the fixed and liquid samples at field intensities of 0–800 kA/m. We also measured the DC

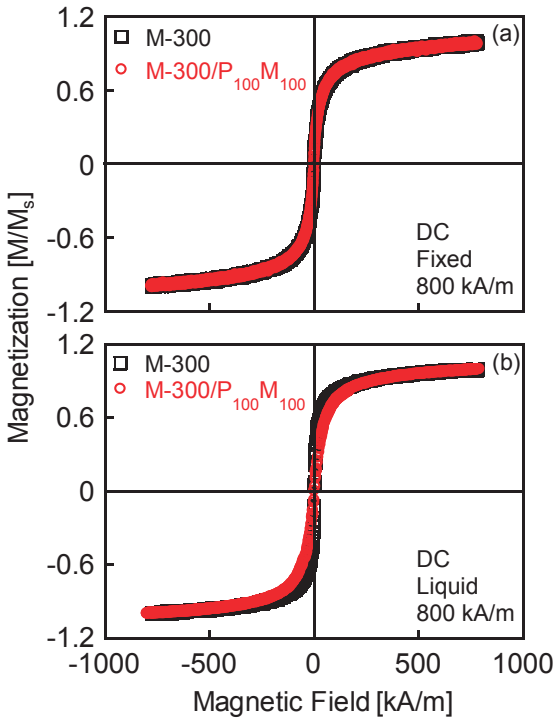

Fig. 9 DC hysteresis loops of (a) fixed sample and (b) liquid sample at magnetic field amplitude of 0–800 kA/m. Concentration of Fe was 3.84 mg/mL.

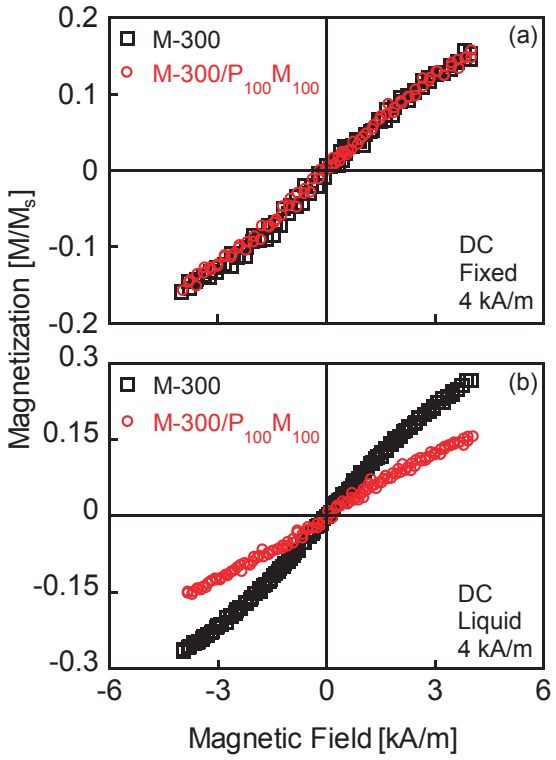

Fig. 10 DC hysteresis loops of (a) fixed sample and (b) liquid sample in magnetic field amplitudes ranging from 0–4 kA/m. Concentration of Fe was 3.84 mg/mL.

hysteresis loops for field intensities of 0–4 kA/m to better understand the magnetization process (Fig. 10). As observed from the results of DC measurements, the MNPs exhibited superparamagnetic characteristics because the coercive force and remanence magnetization could not be confirmed from the hysteresis loops. In this case, the fixed samples had the same magnetization because only the Néel relaxation from the magnetic moment rotation of the core particles operated in the fixed state. However, the magnetization of M-300 was higher than that of M-300/$P_{100}M_{100}$ in the liquid state. We concluded that the action of Brownian relaxation caused by particle rotation was very weak in M-300/$P_{100}M_{100}$ because their R_h value was larger than that of M-300.

Figure 11 shows the dependence of the AC hysteresis loops on frequency at 3.84 mg-Fe/mL for the fixed and liquid samples. As seen, the magnetization decreased as the frequency increased because the particle rotation and magnetic moments gradually became delayed. We also confirmed that the magnetization of M-300/$P_{100}M_{100}$ was lower than that of M-300 in the liquid samples under an AC magnetic field of 10 kHz (Fig. 12). Based on these results, we concluded that the influence of Brownian relaxation was small in the liquid state of the magnetic PIC aggregate due to the difference in the hydrodynamic particle size in M-300. The increase of the

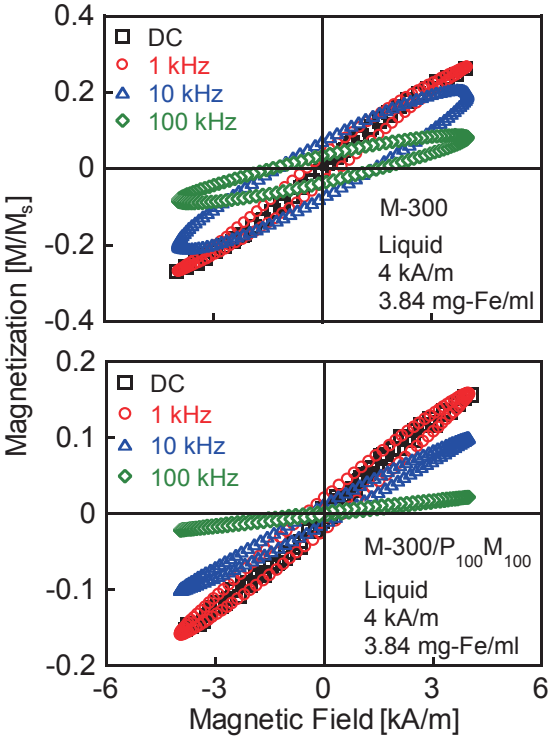

Fig. 11 AC hysteresis loops at 1, 10, and 100 kHz for M-300 and M-300/$P_{100}M_{100}$.

hydrodynamic particle size in M-300/$P_{100}M_{100}$ decreased the degree of particle rotation because of dipole interactions[11].

Figure 13 (a) shows the dependence of ILP on frequency in the liquid sample, as estimated from the areas of the AC hysteresis loops. Note that the observed ILP peaks derived from Brownian relaxation did not appear for the fixed sample (Fig. 13 (b))[12]. Furthermore, we calculated the theoretical Brownian relaxation time using Eq. (1), and determined the viscosities of M-300 and M-300/$P_{100}M_{100}$ at 297.15 K as 1.081 mPa·s and 1.037 mPa·s, respectively. The experimental Brownian

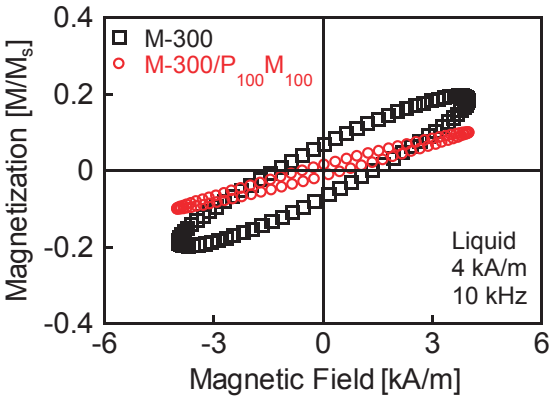

Fig. 12 AC hysteresis loops of liquid samples in applied magnetic field with amplitude of 4 kA/m. Frequency was 10 kHz.

relaxation frequencies of M-300 and M-300/$P_{100}M_{100}$ were 9.0 kHz and 250 Hz, respectively. The measured frequency of the Brownian relaxation peaks was in good agreement with the calculated frequency. The frequency of the Brownian relaxation peak in M-300 was significantly higher than that in M-300/$P_{100}M_{100}$. Thus, particle rotation derived from Brownian relaxation, which increases the degree of the magnetization rotation, clearly occurred in M-300 relative to M-300/$P_{100}M_{100}$ [13, 14]. A higher ILP was obtained for M-300 in the liquid state, whereas a comparable ILP was obtained in the fixed state. The frequency of the Néel relaxation peak, f_N, was not observed in the range of 0.1–100 kHz for the fixed samples. Note that the theoretical Néel relaxation peak was higher than 450 kHz [$K \leq 41$ kJ/m^3][15].

Finally, we assessed the suitability of the magnetic PIC aggregate for applications in MPI. Figures 14 and 15 show the third-harmonic intensities of M-300 and M-300/$P_{100}M_{100}$. The third harmonic signal intensity of M-300 decreased with increasing frequency. We concluded that this was due to a decrease in magnetization caused by magnetic relaxation[16]. In contrast, the magnetic PIC aggregate changed very little under the same conditions. However, it was confirmed that M-300 and M-

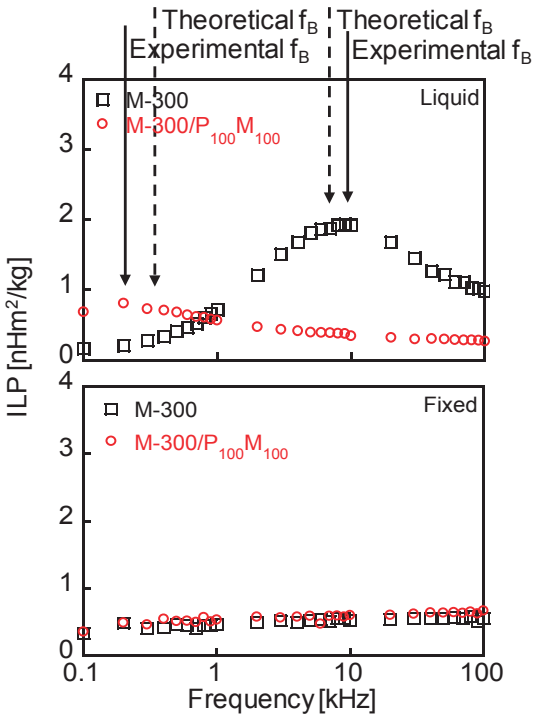

Fig. 13 Dependence of ILP on frequency for the liquid and fixed samples. Dotted lines indicate theoretical Brownian relaxation frequencies of f_B = 5.8 kHz (M-300) and f_B = 460 Hz (M-300/$P_{100}M_{100}$). Solid lines indicate experimental Brownian relaxation frequencies of f_B = 9.0 kHz (M-300) and f_B = 250 Hz (M-300/$P_{100}M_{100}$). No Néel relaxation peaks were observed.

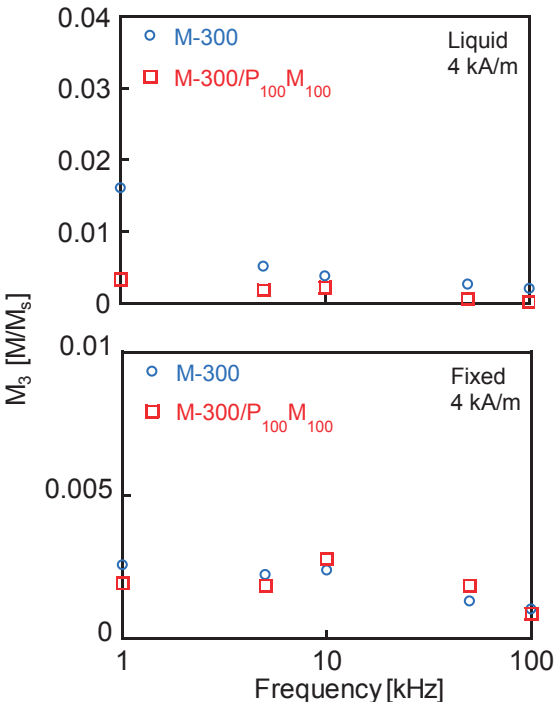

Fig. 14 Dependence of the third-harmonic signal on frequency in liquid and fixed samples.

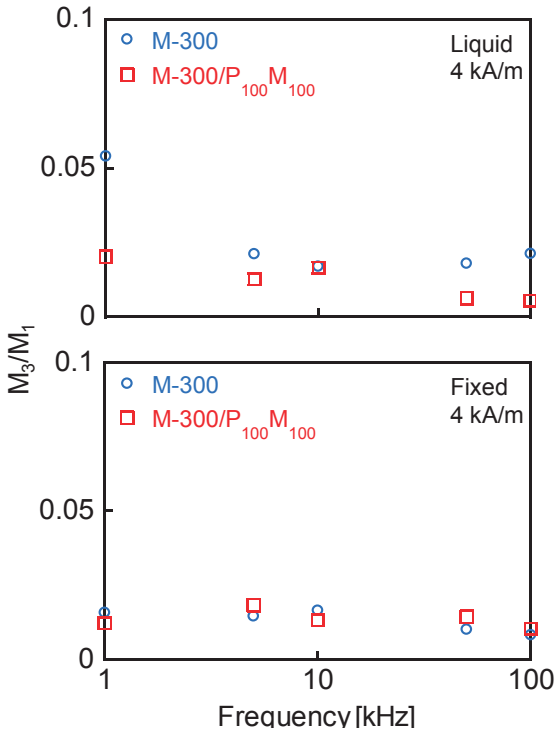

Fig. 15 Dependence of ratio of the third-harmonic signal to fundamental signal on frequency in liquid and fixed samples.

300/$P_{100}M_{100}$ had comparable MPI signal intensities in the fixed state, whereas stronger signal intensities were obtained for M-300 in the liquid state.

The harmonic signal used for MPI is normally concerned with the nonlinear component of magnetization property. The difference in this nonlinear component of magnetization with and without an applied DC bias field is significant for spatial resolution of the constructed image. As shown in Figs. 10 and 11, the nonlinear component of the magnetization loops is not very large. Although the surface modification using $P_{100}M_{100}$ was successfully achieved, optimization of the magnetic core is inevitable to lead to a higher ILP and harmonic signal.

4. Conclusion

In this study, we successfully fabricated $P_{100}M_{100}$ with a biological membrane structure and evaluated the salt concentration dependence of M-300/$P_{100}M_{100}$ when coated with $P_{100}M_{100}$. When the mixing ratio was 0.0739, the surface of the synthesized particles was neutralized by the charge, and the magnetic PIC aggregate was stable and dispersible in pure water and ionic solutions. Based on this result, we infer that the magnetic PIC aggregates can be stably dispersed in a biological body. The results of magnetization measurements allowed us to characterize the influence of different hydrodynamic radii on the magnetization. As the hydrodynamic particle size of the magnetic PIC aggregate increased, the influence of Brownian relaxation decreased due to magnetic interactions. Further, the ILP was measured to investigate the applicability of M-300 and M-300/$P_{100}M_{100}$ to hyperthermia. The particles had comparable ILP values in the fixed state, but that of M-300 was higher in the liquid state. In addition, comparable MPI signal intensities were confirmed in the fixed state by evaluating the third harmonic.

Acknowledgments This work was partially supported by the JSPS KAKENHI Grant Numbers 15H05764, 17H03275, and 17K14693.

Reference

1) M. Arruebo, R. Fernández-Pacheco, M. R. Ibarra, and J. Santamaría, *Nano Today*, **2**(3), 22–32 (2007).
2) Y. Anraku, A. Kishimura, A. Kobayashi, M. Oba, and K. Kataoka, *Chem. Commun.*, **47**, 6054–6056 (2011).
3) D. Kokuryo, Y. Anraku, A. Kishimura, S. Tanaka, M. R. Kano, J. Kershaw, N. Nishiyama, T. Saga, I. Aoki, and K. Kataoka, *J. Controlled Release*, **169**, 220–227 (2013).
4) K. Nakai, M. Nishiuchi, M. Inoue, K. Ishihara, Y. Sanada, K. Sakurai, and S. Yusa, *Langmuir*, **29**, 9651–9661 (2013).
5) A. Jordan, R. Scholz, P. Wust, H. Fähling, and R. Felix, *J. Magn. Magn. Mater.,* **201,** 413–419 (1999).
6) Q. A. Pankhurst, J. Connolly, S. K. Jones, and J. Dobson, *J. Phys. D: Appl. Phys.*, **36**, R167–R181 (2003).
7) B. Gleich, and J. Weizenecker, *Nature,* **435**, 1214–1217 (2005).
8) R. E. Rosensweig, *J. Magn. Magn. Mater.*, **252**, 370–374 (2002).
9) W. T. Coffey and Y. P. Kalmykov, *J. Appl. Phys.,* **112**, 121301 (2012).
10) M. Kallumadil, M. Tada, T. Nakagawa, M. Abe, P. Southern, and Q. A. Pankhurst, *J. Magn. Magn. Mater.*, **321**, 1509–1513 (2009).
11) J. G. Ovejero, D. Cabrera, J. Carrey, T. Valdivielso, G. Salas, and F. J. Teran, *Phys. Chem. Chem. Phys.,* **18**, 10954–10963 (2016).
12) S. H. Chung, A. Hoffmann, S. D. Bader, C. Liu, B. Kay, L. Makowski, and L. Chen, *J. Appl. Phys.,* **97,** 10R101 (2005).
13) S. Ota, R. Kitaguchi, R. Takeda, T. Yamada, and Y. Takemura, *Nanomaterials*, **6**, 170 (2016).
14) T. Yoshida, S. Bai, A. Hirokawa, K. Tanabe, and K. Enpuku, *J. Magn. Magn. Mater.*, **380**, 105–110 (2015).
15) S. Ota, T. Yamada, and Y. Takemura, *J. Appl. Phys.*, **117**, 17D713 (2015).
16) S. Ota, R. Takeda, T. Yamada, I. Kato, S. Nohara, and Y. Takemura, *Int. J. Magn. Part. Imag.*, **3**, 1703003 (2017).

Received Oct. 13, 2017; Accepted Dec. 21, 2017

J. Magn. Soc. Jpn., **42**, 49-54 (2018)

<Paper>

Power supply for medical implants by Wiegand pulse generated from magnetic wire

Katsuki Takahashi, Akitoshi Takebuchi, Tsutomu Yamada, and Yasushi Takemura

Department of Electrical and Computer Engineering, Yokohama National University,

79-5 Tokiwadai, Hodogaya-ku, Yokohama 240-8501, Japan

Implantable medical devices are utilized in the human body for maintaining good health. As these devices are becoming increasingly functionalized, supplying power to them has become very important. Instead of batteries, technologies for wireless power supplies are being developed, such as inductive coupling or piezoelectric elements. However, we propose the use of magnetic wires for this purpose. Inside these wires, a fast magnetization reversal, called a "large Barkhausen jump," occurs due to an applied magnetic field. This reversal induces a large pulse voltage in pick-up coils, which is called a "Wiegand pulse." By applying this pulse as an electric source, a higher electric power is expected compared with the conventional method using a sinusoidal excitation field. A wire core coil was prepared, and open-circuit voltage was measured. In addition, DC voltage and electric power were measured by connecting the wire core coil to a rectifier. The experimental results confirmed the superiority of using a Wiegand pulse at an applied magnetic field intensity of 60 Oe and a frequency of lower than 10 kHz.

Keywords: magnetization reversal, large Barkhausen jump, FeCoV wire, Wiegand pulse, implantable medical device

1. Introduction

A large Barkhausen jump, which is known as the Wiegand effect[1], is a fast magnetization reversal in a magnetic wire that has bistable states. It induces a large pulse voltage, called a Wiegand pulse, in the pick-up coil when a magnetic field is applied. In this study, a twisted FeCoV wire made from an optimum material yielding this effect was used. The Wiegand effect has certain advantages: it does not need any external power supply, and the amplitude of the pulse voltage is still large at both high and low frequencies, while an ordinary sinusoidal electromotive force depends on the frequency of the applied magnetic field. This phenomenon has been used in many sensor applications, such as rotation sensors and speed sensors[2,3]. Further, vibration-type energy-generating elements by exciting the magnetic wire through a single magnet are being developed[4,5].

In this study, a magnetic wire and Wiegand pulse were used as the power source, which provides DC voltage to the implant inside the human body. Ordinary inductive power transfer systems typically use excitation frequency ranging from hundreds of kilohertz to several megahertz. At such high frequency, the excitation voltage, current, and size of the coil tend to be too large for applying enough magnetic field to deep the human body. Further, unexpected heating of the body surface caused by the eddy currents cannot be ignored. To eliminate these problems, we proposed the use of a magnetic wire. Using the wire as the core of the pick-up coil and generating a large Wiegand pulse by applying a magnetic field, enough electric power can be achieved at low excitation frequency. Then, reduction of not only the size of both excitation coil and pick-up coil, but also the required excitation voltage, can be realized.

2. Structure of Electricity Generation

2.1 FeCoV wire

An 11-mm-long FeCoV ($Fe_{0.4}Co_{0.5}V_{0.1}$) wire was used in this study. When torsion stress was applied to the wire, the outer shell near the surface became magnetically soft. When the stress was released, two layers appeared: the outer layer, called soft layer, which had a coercive force of 20 Oe, and the inner layer, called the hard core, which had a coercive force of 80 Oe. Details on the magnetic properties of twisted FeCoV wires and torsion stress dependence have been reported by Abe *et al.*[6,7]. This magnetic wire exhibits a uniaxial magnetic anisotropy along its length direction.

Figure 1 shows schematic diagrams of magnetic structure and magnetization process of the soft layer in the FeCoV wire used in this study. These characteristics

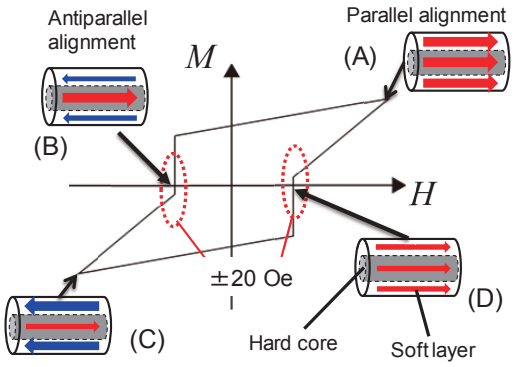

Fig. 1 Schematic diagrams of magnetic structure and minor hysteresis loop of FeCoV wire.

are essentially same with those reported in Ref. 5), in which both of measured full and minor loops have been shown. The magnetization alignment of the soft layer and the hard core can be either in a parallel state or an antiparallel state, as shown in Fig. 1. The magnetization alignment takes a parallel state when an external magnetic field of larger than 20 Oe is applied in the right direction along its length, as shown in Fig. 1(A). When a magnetic field with an opposite direction to that of magnetization is applied and reaches −20 Oe, the magnetization of the soft layer is reversed steeply and takes an antiparallel state, as indicated in Fig. 1(B). This magnetization reversal, called the large Barkhausen jump, is due to a fast domain wall propagation. Thereby, a large pulse voltage, called a Wiegand pulse, is induced in the pick-up coil around the wire. The strength of magnetization of the soft layer along the left direction increases with the magnetic field applied in the left direction from −20 Oe at (B). Then, the direction of the magnetic field switches at (C), and the wire starts receiving the right magnetic field. On reaching 20 Oe, magnetization reversal again occurs rapidly in the soft layer, shown by (D) (from antiparallel state to parallel state), and a Wiegand pulse is induced. If the maximum value of the applied field intensity is within 80 Oe, the magnetization of the hard core does not reverse.

2.2 Wiegand pulse in wire core coil

By using the wire as a coil core and applying a magnetic field larger than 20 Oe, a Wiegand pulse is induced in the pick-up coil wound around the wire. Figure 2 shows a waveform of the measured Wiegand pulse during magnetization reversal of the soft layer excited by approaching a magnet in extremely slow movement. When the wire is excited by an AC magnetic field, sinusoidal electromotive force is also induced in the pick-up coil. Therefore, the waveform of the wire core coil by AC excitation combines these two waveforms, as shown in Fig. 3. The pick-up coil of 3000 turn was used in this measurement. Unlike the sinusoidal electromotive force, the width of a Wiegand pulse does not vary according to the excitation frequency. As seen in the figure, positive and negative Wiegand pulses are

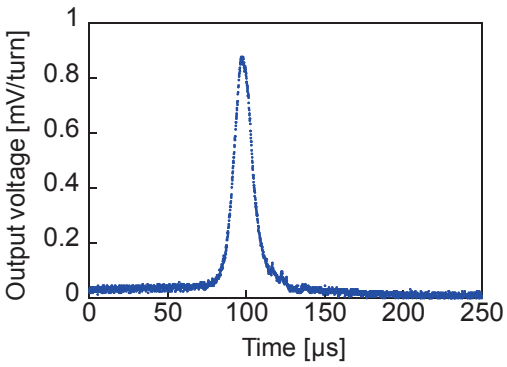

Fig. 2 Wiegand pulse generated by magnet excitation.

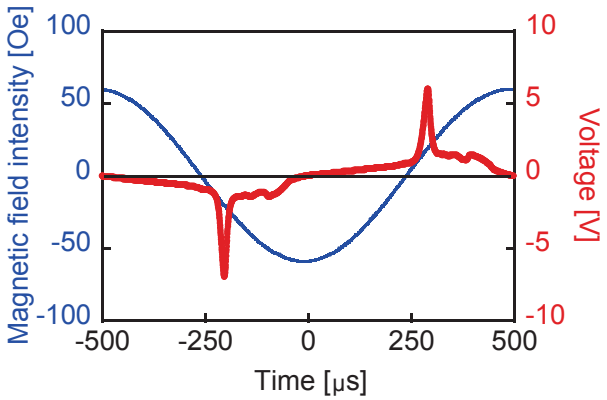

(a) Excitation frequency of 1 kHz.

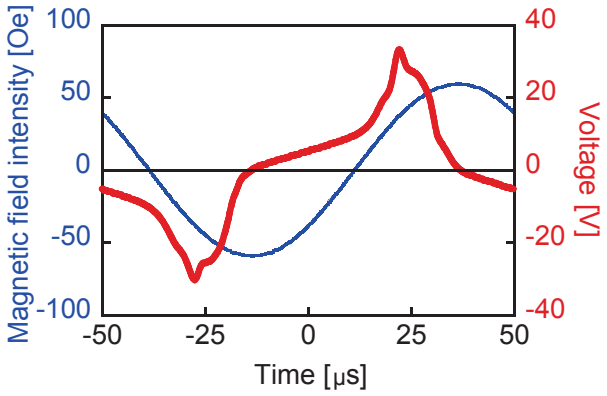

(b) Excitation frequency of 10 kHz.

Fig. 3 Waveforms of applied AC magnetic field of 60 Oe and induced voltage of wire core coil at field frequencies of (a)1 kHz and (b)10 kHz.

observed in one period, each of which results from two reversals of the soft layer: parallel to antiparallel and antiparallel to parallel. In the 1 kHz waveform shown in Fig. 3(a), only a Wiegand pulse is mostly observed, while in the 10 kHz waveform shown in Fig. 3(b), sinusoidal components can be slightly seen, but are still much less dominant compared to a Wiegand pulse.

In this study, a voltage-double rectifier was used, and a Wiegand pulse was converted to DC voltage assuming the electric power supplied to capsule endoscopy or many other implantable medical devices. Enough electric power at a low frequency was aimed using a Wiegand pulse generation. The excitation frequency was set to lower than 10 kHz in all experiments.

3. Experiment

3.1 Comparison of open-circuit voltage in wire and air core coil

A pick-up coil of 9 mm length and 3000 turns was wound around the FeCoV wire (length: 11 mm). The diameter of the wire was a few tenth of a millimeter. Its magnetic properties were essentially same with those of

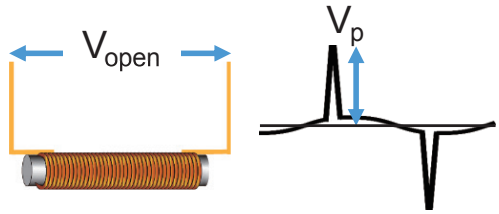

(a) Configuration of wire core coil and measurement of Wiegand pulse.

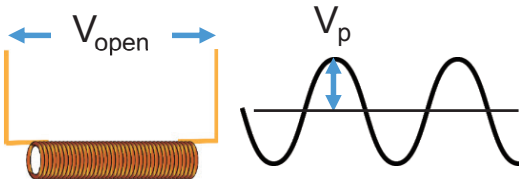

(b) Configuration of air core coil and measurement of sinusoidal electromotive force.

Fig. 4 Open-curcuit voltage of wire core coil (Wiegand pulse) and air core coil (sinusoidal electromotive force).

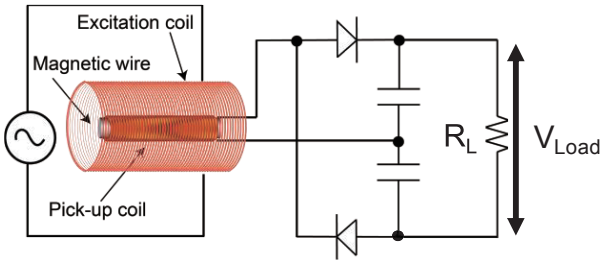

(a) Configuration of wire core coil, excitation coil, voltage rectifier circuit, and load resistor.

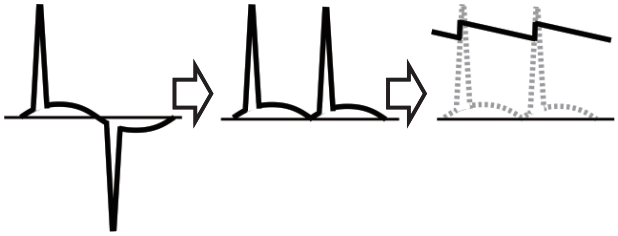

(b) Process through which Wiegand pulse is rectified and smoothed by circuit above.

Fig. 5 Conversion of Wiegand pulse into DC voltage: configuration and process.

the FeCoV wire of 0.25 mm diameter[4,5]. The volumes of the soft and hard core were 23% and 77%, respectively. The excitation coil, with 25 mm length and 22 mm diameter, applied the AC magnetic field to the entire wire core coil. Each end of the core coil was connected to an oscilloscope and the peak of the open-circuit voltage was measured; subsequently, this peak was compared with that of the air coil. In the measurement of magnetic field intensity dependence, the field intensity ranged from 0 Oe to 100 Oe and the excitation frequency was set to 1 kHz. In the measurement of excitation frequency dependence, the frequency ranged from 100 Hz to 10 kHz and the field intensity was set to 60 Oe. As shown in Fig. 4, the peak of the Wiegand pulse was measured in the wire core coil, and the amplitude of the sinusoidal electromotive force was measured in the air coil.

3.2 Measurement of electric power obtained from Wiegand pulse

As shown in Fig. 5(a), the wire core pick-up coil was connected to a voltage-double rectifier, which consisted of two Schottky diodes and 1 μF capacitors and a load resistor. The excitation coil was arranged around the pick-up coil, and the size and number of turns of each coil were the same as those mentioned in the previous section. The Wiegand pulse was rectified and smoothed as shown in Fig. 5(b). Then, the load voltage and its ripple components were measured with the resistance value varying from 100 Ω to 1 MΩ, and electric power was calculated. Intensity of the AC magnetic field for excitation was set to 60 Oe, and two frequencies were used: 1 kHz and 10 kHz. The ripple rate was calculated using the following equation.

$$Ripple = \frac{V_{max} - V_{min}}{V_{ave}} \times 100 \qquad (1)$$

3.3 Comparison of electric power obtained from the wire and ferrite core coil

To confirm the usefulness of the Wiegand pulse at low frequency, a high-permeability magnetic material, MnZn ferrite, was used for the coil core and compared with the wire core coil. The ferrite core strengthened the magnetic flux around the pick-up coil, and the sinusoidal electromotive force itself increased. The size of the ferrite core used in this experiment was 1 × 1 × 10 mm^3. The ferrite core and the wire were each wound by a pick-up coil of 400 turns. Each core coil was connected to the voltage-double rectifier and load resistor, as described in the previous section. Then, the load voltage was measured and electric power generated from the wire and the ferrite core was calculated and compared. Because the ferrite core and wire had different sizes, the measured data were normalized with their cross-sectional area. Load resistance was 1 MΩ and capacitance was 1 μF. The excitation magnetic field intensity was set to 60 Oe, which is enough to generate a Wiegand pulse. The excitation frequency ranged from 100 Hz to 10 kHz.

4. Results and Discussion

4.1 Comparison of open-circuit voltage with changing applied field intensity or frequency

Figure 6 shows the dependence of open-circuit voltage

on magnetic field intensity at 1 kHz of excitation frequency and that of excitation frequency on 60 Oe of applied field intensity.

As shown in Fig. 6(a), when the excitation field was 20 Oe or more, the peak value of the wire core was far larger than that of the air coil. This implies that the Wiegand pulse was generated due to magnetization reversal in the soft layer; its peak value increased with the applied field intensity. When the applied field was within 20 Oe, because the Wiegand pulse was not generated, ordinary electromotive force was measured. At an applied field of 10 Oe, the peak value of the wire core was 84.2 mV, which was slightly larger than that of the air core (28.4 mV). It was found that because of the magnetic permeability of the wire, magnetic flux around the pick-up coil strengthened, and the electromotive force increased to a certain degree. The magnetization of the hard core was also reversed by the applied field above 80 Oe, which resulted in lower output voltage from the wire[6]. The voltage was expected to be saturated or more decreasing even though the magnetic field exceeded 100 Oe. Magnetization reversal of the hard core is not necessary for generating the Wiegand pulse, and the field intensity should not be excessively strong. Then, the ideal intensity for generating the Wiegand pulse is around 60–80 Oe. Therefore, in this study, the applied field was set to 60 Oe, which fixed the field intensity.

In Fig. 6(b), at all measured frequencies, the peak value of the Wiegand pulse was far larger than the electromotive force of the air coil. As the frequency increased, the amplitude of the wire core coil also increased. We assumed that the sinusoidal component increased at higher frequency, and then, the peak value of the Wiegand pulse was increased.

From these results, higher electric power is expected to be secured at lower excitation frequency during conversion to DC voltage.

4.2 Electric power obtained from wire core coil

Figure 7 shows the results of the measured voltage

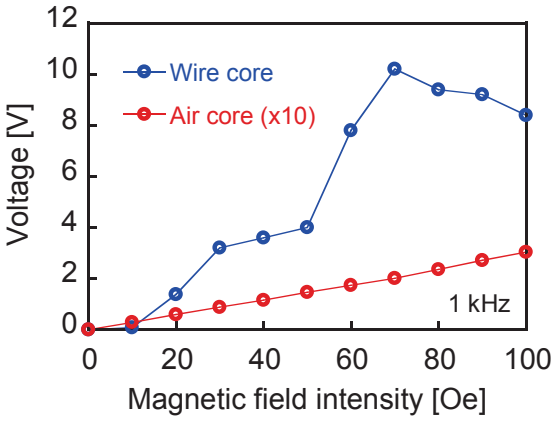

(a) Dependence of 1 kHz of excitation frequency on field intensity.

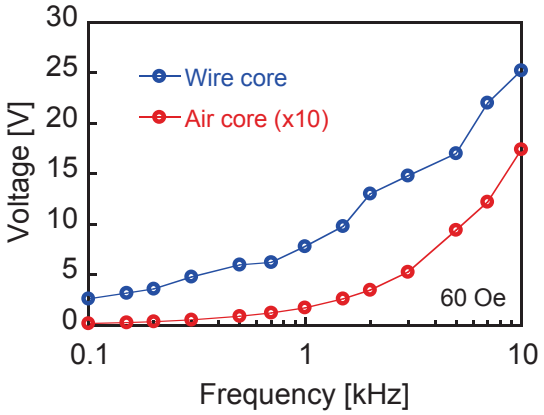

(b) Dependence of 60 Oe of applied field intensity on excitation frequency.

Fig. 6 Dependence of open-curcuit voltage of wire core coil and air core coil on applied field intensity and excitation frequency.

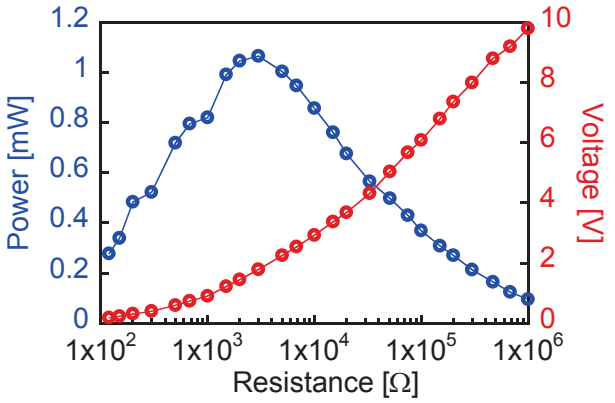

(a) DC voltage and electric power with change in resistance.

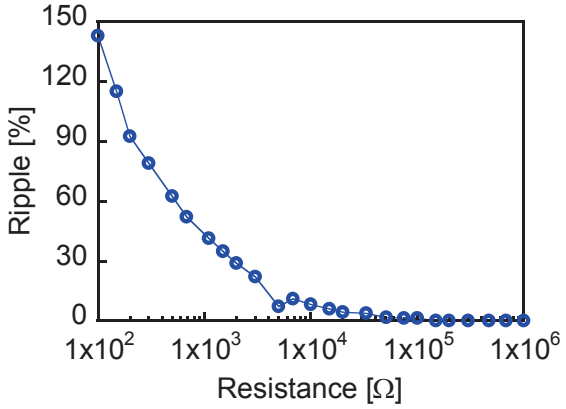

(b) Ripple rate of load voltage.

Fig. 7 Dependence of DC voltage (average value) and electric power on resistance and its ripple rate, at 60 Oe of applied field intensity and 1 kHz of excitation frequency.

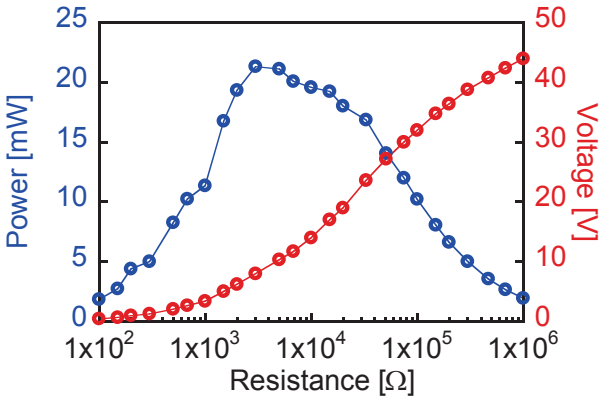

(a) DC voltage and electric power with change in resistance.

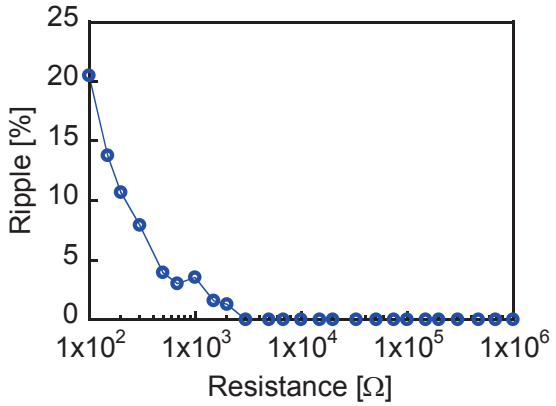

(b) Ripple rate of load voltage.

Fig. 8 Dependence of DC voltage (average value) and electric power on resistance, and its ripple rate at 60 Oe of applied field intensity, and 10 kHz of excitation frequency.

and electric power of load resistance (a) at 1 kHz excitation frequency, and its ripple (b). The maximum obtained electric power was 1.2 mW. The ripple rate deteriorated at lower resistances. In the case where the wire core coil receives power from the excitation coil and provides voltage to the implant device throughout operation in the human body, the fluctuation in the load voltage should be less, and thus, the capacitor should be optimized.

Figure 8 shows same results as Fig. 7 but at an excitation frequency of 10 kHz. The maximum electric power was approximately 21 mW. Under this excitation condition, there is enough possibility of feeding the power required to operate implantable medical devices (for example, power consumption of capsule endoscopy is 25 mW[8]), and is expected to lessen in the future). Further, the load voltage at the highest electric power was 1.56 V at 1 kHz and 8 V at 10 kHz excitation. Considering that the voltage of a button battery, the main power source of implantable medical devices, is around 1.5 V, DC voltage from the Wiegand pulse was also sufficient.

4.3 Comparison of electric power generated from wire core and ferrite core

Figure 9 shows a comparison of the electric power generated from the wire core coil and the ferrite core coil. The excitation frequency was 1 kHz. The ripple almost disappeared because the circuit parameters (capacitance and load resistance) and the time constant were large enough. Electric power from the Wiegand pulse increased significantly from the applied field intensity of 20 Oe or more. Even considering the demagnetizing field inside the ferrite, the power from the ferrite core coil remained smaller at almost all intensity values. The tendency of the wire core coil resembles that in Fig. 6(a), in that the peak of the applied field intensity was in the range of 70–80 Oe.

Figure 10 shows a comparison of the electric power generated from the wire core and ferrite core with changing excitation frequency. In frequencies lower than 10 kHz, the wire core coil had an advantage. Thus, the

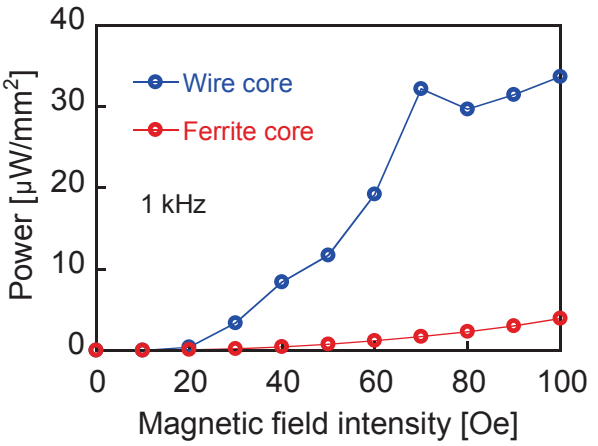

Fig. 9 Comparison of electric power generated from wire core and ferrite wire coil with change in applied field intensity at 1 kHz.

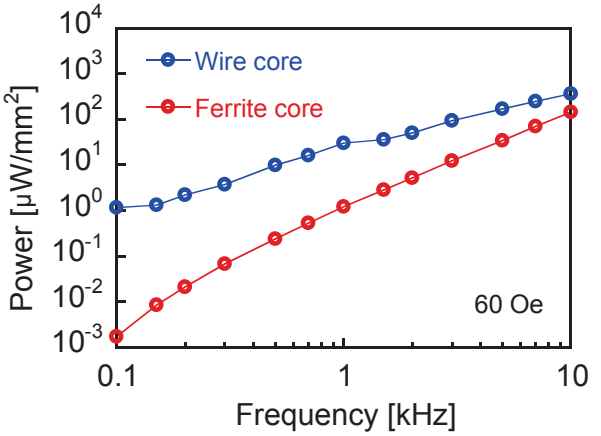

Fig. 10 Comparison of electric power generated from wire core and ferrite wire coil with change in excitation frequecncy at 60 Oe.

usefulness of the Wiegand pulse and wire core coil at lower excitation frequency was confirmed. If the excitation frequency is increased beyond 10 kHz, the sinusoidal electromotive force will increase, and the ferrite core coil may become superior to the wire core coil.

5. Conclusion

This paper proposes a new method of power supply using an 11-mm-long FeCoV wire. A Wiegand pulse was induced in a pick-up coil wound around the wire by an AC magnetic field of the excitation coil. A comparison of the open-circuit voltage with the air core coil showed that the Wiegand pulse has much larger peak than the sinusoidal electromotive force at frequencies lower than 10 kHz. Subsequently, the Wiegand pulse was rectified and smoothed by a voltage-double rectifier, and it was confirmed that the wire core coil can provide enough electric power to implantable medical devices. Further, the wire core coil was compared to the ferrite core coil, which had high permeability, and higher electric power was obtained by the Wiegand pulse, even though the electromotive force was amplified by the ferrite core at the measured frequency. In addition, it was found that reduction in the size of pick-up and excitation coils, and reduction in the excitation frequency were expected.

Acknowledgments The authors express their gratitude to Nikkoshi Co., Ltd., Japan, for supplying FeCoV wires.

References

1) J. R. Wiegand and M. Velinsky: U.S. Patent #3, 820, 090 (1974).
2) R. Malmhall, K. Mohri, F. B. Humphrey, T. Manabe, H. Kawamura, J. Yamasaki, and I. Ogasawara, *IEEE Trans. Magn.*, **23**, 3242 (1987).
3) M. Vázquez, C. Gómez-Polo, D.-X. Chen, and A. Hernando, *IEEE Trans. Magn.*, **30**, 907 (1994).
4) A. Takebuchi, T. Yamada, and Y. Takemura, *J. Magn. Soc. Jpn.*, **41**, 34 (2017).
5) Y. Takemura, N. Fujinaga, A. Takebuchi, and T. Yamada, *IEEE Trans. Magn.*, **53**, 4002706, (2017).
6) S. Abe, T. Ikenaga, K. Suwa, and A. Matsushita, *IEEE Trans. Magn.*, **32**, 4971 (1996).
7) S. Abe, A. Matsushita and M. Naoe, *IEEE Trans. Magn.*, **33**, 3916 (1997).
8) J. Thone, S. Radiom, D. Turgis, R. Carta, G. Gielen, and R. Puers, *Sensors and Actuators A: Physical*, **156**, 43 (2009).

Received Oct. 13, 2017; Accepted Dec. 21, 2017

J. Magn. Soc. Jpn., **42**, 55-61 (2018)

<Paper>

Dynamic hysteresis measurement of magnetic nanoparticles with aligned easy axes

Ryoji Takeda, Satoshi Ota*, Tsutomu Yamada, and Yasushi Takemura

Department of Electrical and Computer Engineering, Yokohama National University,
79-5 Tokiwadai, Hodogaya-ku, Yokohama 240-8501, Japan
*Department of Electrical and Electronic Engineering, Shizuoka University,
3-5-1 Johoku, Naka-ku, Hamamatsu 432-8501, Japan

Magnetic particle imaging (MPI) is a novel diagnostic imaging technique based on the use of magnetic nanoparticles (MNPs). Investigating the magnetic properties of magnetic nanoparticles is important for achieving a high spatial and temporal resolution in MPI. In this study, γ-Fe_2O_3 nanoparticles (core diameter: d_c = 4 nm), Fe_3O_4 nanoparticles (d_c = 20–30 nm), and Resovist® were immobilized in a DC magnetic field with their easy axes aligned. DC and AC magnetization curves were measured for the prepared MNPs. The measurements were performed by applying fields parallel and perpendicular to the easy axis and evaluating the magnetic properties of the MNPs for the easy and hard axes. The direction of magnetic moments under the AC magnetic field applied to the direction of the easy axis or hard axis was evaluated by using both experimental results and numeric simulation using the Landau–Lifshitz–Gilbert equation to reveal magnetic relaxation property at wide frequency range and the effect of core size distribution of oriented MNPs. The effect of anisotropy in superparamagnetic nanoparticles, the relaxation property depending on the anisotropy energy barrier, and the fast magnetization process of Néel relaxation were successfully observed.

Keywords: magnetic nanoparticle, magnetic particle imaging, magnetic relaxation, magnetic easy axis, magnetization curve

1 Introduction

Magnetic nanoparticles (MNPs) are promising candidates for biomedical applications such as cancer treatment and diagnostic imaging[1]. In particular, magnetic nanoparticle imaging (MPI) is attracting attention owing to its potential for novel diagnostic applications[2]. MPI is an imaging technique that detects MNPs directly through the nonlinearity of their magnetization. *In vivo* cancer imaging using MPI has been reported with characteristic spatial resolution of approximately 1 mm[3]. The MPI signal is strongly dependent on the size or structure of the used particle[4,5], so the resolution of MPI can be improved by optimizing these parameters. To achieve high spatial and temporal resolution of MPI, the magnetic properties of MNPs should be investigated, and optimal conditions related to the applied field and the MNP parameters should be determined. In this study, we fabricated samples from MNPs with aligned easy axes and measured their magnetic properties.

Orientation of the easy axes of MNPs in an AC field obtained by simulations and experiments has been reported previously[6–8]. The orientation of the easy axes should be considered in MPI, which uses an AC magnetic field for diagnosis. It is important to clarify the magnetic properties of MNPs in an AC field with regard to the degree of anisotropy. Magnetization measurement at 20 kHz and its harmonic signal of oriented MNPs have been reported by Yoshida *et al.*[9]. We measured magnetization curves for superparamagnetic and ferromagnetic iron-oxide nanoparticles with aligned easy axes under an AC magnetic field with a frequency up to 500 kHz considering their relaxation properties, and observed clear anisotropy of the MNPs in this study. As magnetic properties certainly depend on the core size of MNPs[4], the effect of core size distribution was also studied with using the oriented MNPs.

The energy of an MNP placed in an external magnetic field consists of the anisotropy energy and the energy associated with the external magnetic field, as given by the Stoner–Wohlfarth model:

$$E = K_u V_M \sin^2\theta - \mu_0 MH\cos(\phi - \theta). \quad (1)$$

where K_u, V_M, θ, μ_0, M, H, and ϕ are the magnetic anisotropy constant, the volume of the primary particle, the angle between the easy axis and the magnetic field, the permeability of free space, the magnetization of the MNP, the intensity of the external field, and the angle between the easy axis and the magnetization, respectively[10]. Magnetic moments tend to align with the direction of the magnetic easy axis and the magnetic field to minimize the anisotropy energy and the energy associated with the external magnetic field, respectively. The anisotropy energy depends on the size of the MNP. In a superparamagnetic nanoparticle, the orientation of the magnetic moment is randomized by the thermal energy, and the magnetic properties show no coercivity or remanence because the anisotropy energy is smaller than the thermal energy.

When an AC field is applied to the MNPs, magnetic relaxation occurs owing to the delay of magnetization in the AC field. Néel relaxation time τ_N derived from the

rotation of the magnetic moment is given by the following equation:

$$\tau_N = \tau_0 \exp\left(\frac{K_u V_M}{k_B T}\right), \quad (2)$$

where τ_0, k_B, and T are the attempt time, the Boltzmann constant, and the temperature, respectively[11,12].

2 Materials and methods

2.1 Materials and samples

Water-dispersed γ-Fe_2O_3 nanoparticles supplied from Meito Sangyo Co. Ltd. with core diameters (d_c) of 4 nm were used as superparamagnetic nanoparticles. They were coated with carboxymethyl-diethylaminoethyl dextran. In addition, Fe_3O_4 nanoparticles purchased from Nanostructured and Amorphous Materials Inc. with d_c of 20–30 nm were used as ferromagnetic nanoparticles. They were coated with polyethylenimine to achieve better dispersion in the solution.

Two types of solid samples were prepared for either type of MNPs. One solid sample contained MNPs fixed with epoxy bond in the absence of magnetic fields, and the other solid sample contained MNPs fixed in a DC magnetic field applied with an electromagnet for 8 h. Thus, the easy axes of MNPs in the first sample were oriented randomly. In contrast, in the second sample, the magnetic easy axes of the MNPs were aligned. The intensity of the DC field during the preparation of the sample with aligned easy axes was 575 kA/m. The concentration of MNPs in both types of samples was adjusted to 2 mg-Fe/ml.

We also prepared samples with the aligned easy axes using Resovist®, a contrast agent generally used in MRI. Resovist® is a commercially available MNP that indicates superparamagnetic behavior[5] and is generally used for experiments on MPI[2] and hyperthermia[13]. It has been reported that Resovist® consists of multi core particles with their certain size distribution[14]. The magnetic property of Resovist® was compared with those of the γ-Fe_2O_3 (4 nm) samples which exhibited smaller core size distribution[5].

2.2 Magnetization measurements

DC magnetization curves were measured with a vibrating sample magnetometer (VSM), and AC magnetization curves were measured with a pickup coil at a frequency of 1–100 kHz under the amplitudes of the applied field of 4 kA/m and 16 kA/m[15]. For the solid sample with aligned easy axes, DC and AC hysteresis measurements were performed by applying magnetic fields parallel and perpendicular to the easy axis, which we defined as the easy axis sample and the hard axis sample, respectively. All measurements were taken at 298 K. The saturation magnetization of the sample was estimated by fitting the measured DC magnetization curve at the field intensity of 800 kA/m to calculate the magnetization curve from the Langevin function.

2.3 Numerical simulation

In the magnetization measurement, the results indicate the total magnetization of MNPs in the sample. Therefore, the magnetic states and magnetization distribution of individual MNPs were evaluated by numerical simulations. Numerical simulations were performed using the Landau–Lifshitz–Gilbert (LLG) equation[7, 16]:

$$\frac{d\boldsymbol{m}}{dt} = -\frac{\gamma}{1+\alpha^2}\{\boldsymbol{m}\times[\boldsymbol{H}+\alpha\boldsymbol{m}\times\boldsymbol{H}]\}, \quad (3)$$

where $\boldsymbol{m}$, γ, α, and $\boldsymbol{H}$ are the magnetization, gyromagnetic ratio, damping parameter (α = 0.1), and effective field, respectively. The magnetization was calculated as the value normalized by the saturated magnetization according to Eq. (3) using the Runge–Kutta algorithm. The gyromagnetic ratio is estimated by

$$\gamma = \frac{\mu_0 M_s V_M (1+\alpha^2)}{2\alpha\tau_N k_B T}, \quad (4)$$

where M_s is the saturated volume magnetization of 351 kA/m. The effective field is given by

$$\boldsymbol{H} = \boldsymbol{H}_{ex} + \boldsymbol{H}_{ani} + \boldsymbol{H}_{th} \quad (5)$$

In this equation,

$$\boldsymbol{H}_{ani} = \frac{K_u(\boldsymbol{m}\cdot\boldsymbol{n})}{\mu_0 M_s}\boldsymbol{n}, \quad (6)$$

where $\boldsymbol{H}_{ex}$, $\boldsymbol{H}_{ani}$, $\boldsymbol{H}_{th}$, and $\boldsymbol{n}$ are the excited field, the magnetic anisotropy field, the fluctuating field due to thermal noise, and a unit vector along the easy axis, respectively. The thermal fluctuating field is satisfied by the following equations:

$$\langle H_{th,i}(t)\rangle = 0 \quad (7)$$

$$\langle H_{th,i}(t)H_{th,j}(t')\rangle = \frac{2\alpha}{1+\alpha^2}\frac{k_B T}{\gamma\mu_0 M_s V_M}\delta_{ij}\delta(t-t'). \quad (8)$$

In these equations, i and j are Cartesian indices of different particles. δ_{ij} is the Kronecker delta function, and δ is the Dirac delta function. The AC field of 16 kA/m at 100 kHz was applied parallel and perpendicular to the easy axis as in the experiments. In the numerical simulations, 28,672 particles were set with core diameters of 5±2 nm (mean±SD) and magnetic anisotropy constants of 20±1 kJ/m^3, which followed the Gaussian distribution. There was no relation between the core diameters and the magnetic anisotropy constants. The easy axes of MNPs were completely oriented to same direction. Distributions of the number of particles were evaluated according to their dependence on the orientation of magnetization.

3 Results and discussion

3.1 DC magnetization curves

Figure 1 and Figure 2 show the DC magnetization curves of both samples at field intensities of 800 kA/m and 4 kA/m, respectively. The magnetization was

normalized by saturation magnetization and represented in the unit of M/M_s. At the intensity of 575 kA/m, which corresponds to the intensity of the DC field during the preparation of the sample with aligned easy axes, magnetization greater than 85% of the saturation magnetization is observed in the sample with randomly oriented MNPs. For γ-Fe_2O_3 (4 nm) nanoparticles (Fig. 2 (a)), the coercivity of the DC magnetization curves in all samples is marginal. This is because the anisotropy energy is smaller than the thermal scattering energy at 298 K owing to the small volume of the measured γ-Fe_2O_3 (4 nm) nanoparticles. Therefore, the magnetic moments are randomly oriented, and the total magnetization at zero field is zero, which is characteristic of superparamagnetic nanoparticles. The magnetizations in the easy axis sample and hard axis sample were larger and smaller than that in the random sample, respectively. Clear anisotropy of the superparamagnetic nanoparticles at 298 K is observed. The distribution of the magnetic moments is shown in Fig. 3. When the magnetic field is applied to the MNPs, the magnetic moments tend to align with the easy axis owing to the energy associated with the applied field, and then the easy axis and the hard axis indicate the directions of large and small magnetization, respectively. In the absence of the magnetic field, the magnetic moments tend to align with the easy axis, but because they are randomly oriented owing to the thermal energy, the total magnetization is zero at zero field.

On the other hand, Fe_3O_4 (20–30 nm) nanoparticles exhibit large magnetization and coercivity when the magnetic field is applied parallel to the easy axis and small magnetization and coercivity when the magnetic field is applied along the hard axis, as shown in Fig. 2 (b). This is because the anisotropy energy barrier is large for the easy axis sample and small for the hard axis sample.

3.2 AC magnetization curves

Figure 4 and Figure 5 show the DC magnetization curves and AC magnetization curves of Fe_3O_4 (20–30 nm) nanoparticles at field frequencies of 1–100 kHz and intensities of 4 kA/m and 16 kA/m, respectively. The coercivities of the DC and AC magnetization curves are very similar at the field intensity of 4 kA/m regardless of the easy axis direction. It can be concluded that the magnetic moment does not exhibit detectable rotation at such small field intensities as 4 kA/m owing to the large diameters of the particles. In contrast, at large field intensities such as 16 kA/m, the coercivities of the DC and AC magnetization curves are very similar for the field applied along the hard axis. However, the coercivity of the DC magnetization curve is smaller

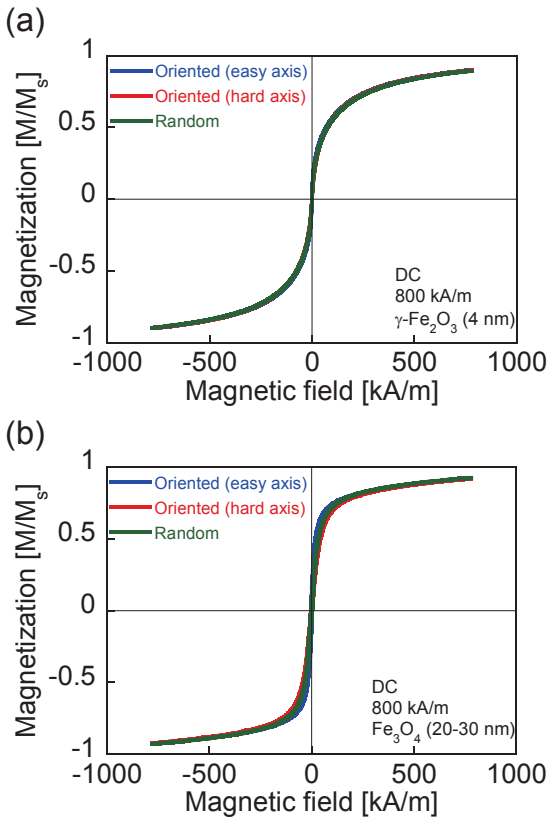

Fig. 1 DC magnetization curves of (a) γ-Fe_2O_3 (4 nm) and (b) Fe_3O_4 (20–30 nm) at field intensity of 800 kA/m.

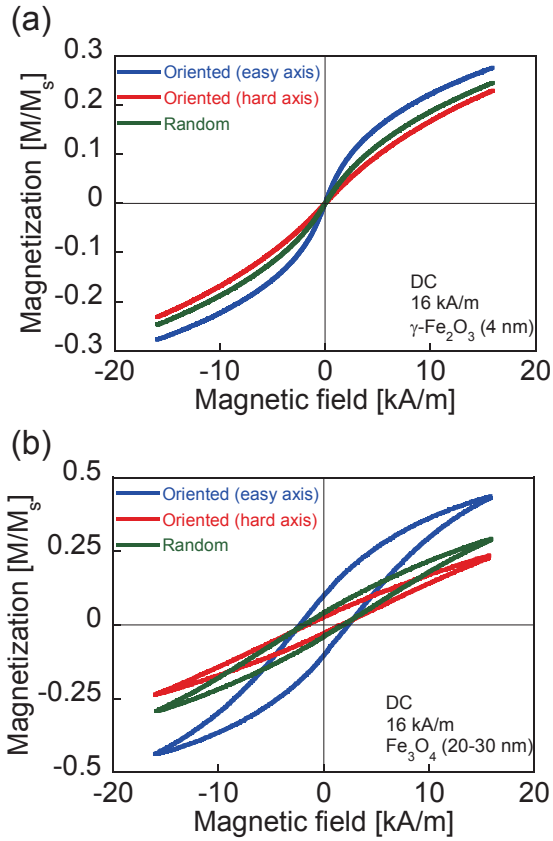

Fig. 2 DC magnetization curves of (a) γ-Fe_2O_3 (4 nm) and (b) Fe_3O_4 (20–30 nm) at field intensity of 16 kA/m.

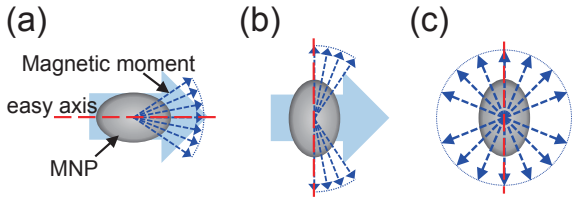

Fig. 3 Distribution of magnetic moments when magnetic field is applied to (a) easy axis and (b) hard axis. Distribution of magnetic moments at zero field (c).

than that of the AC magnetization curve for the field applied along the easy axis. We can conclude that magnetization reversal occurs at 16 kA/m. The coercivity remains constant for the frequency range of 1–100 kHz. This is because the peak frequency of Néel relaxation for the Fe_3O_4 (20–30 nm) nanoparticles calculated from Equation (2) is less than 0.01 Hz (K_u = 23 kJ/m^3)[17] and lies almost outside of the measured frequency range.

Figure 6 shows a comparison between the AC magnetization curves for the samples of γ-Fe_2O_3 (4 nm) nanoparticles with easy axis sample, hard axis sample, and random sample at a frequency of 10 kHz and intensity of 16 kA/m. As the DC magnetization, the easy axis sample shows the highest value, whereas the hard axis sample shows the lowest. The harmonic signal in MPI can be increased by applying an AC field along the easy axis due to larger magnetization of the MNP[9]. Although the coercivities of the DC magnetization curves are marginal in all samples, the easy axis sample shows the highest coercivity, whereas the hard axis sample shows the lowest. This behavior indicates that there is a delay between the magnetization and the applied field associated with the angle between the applied field and the easy axis, which implies a difference in the anisotropy energy barrier. Similar results for superparamagnetic nanoparticles and ferromagnetic nanoparticles have been obtained previously from both numerical simulations and experiments[18–20].

Figure 7 shows the distribution of the number of particles for the 5±2 nm particles obtained from numerical simulations at a frequency of 100 kHz and intensity of 16 kA/m. The horizontal and vertical axes indicate the magnetization of MNP and the percentage distribution of particles, respectively. The maximum value of the distribution, which describes the percentage of particles with reversed magnetization, is

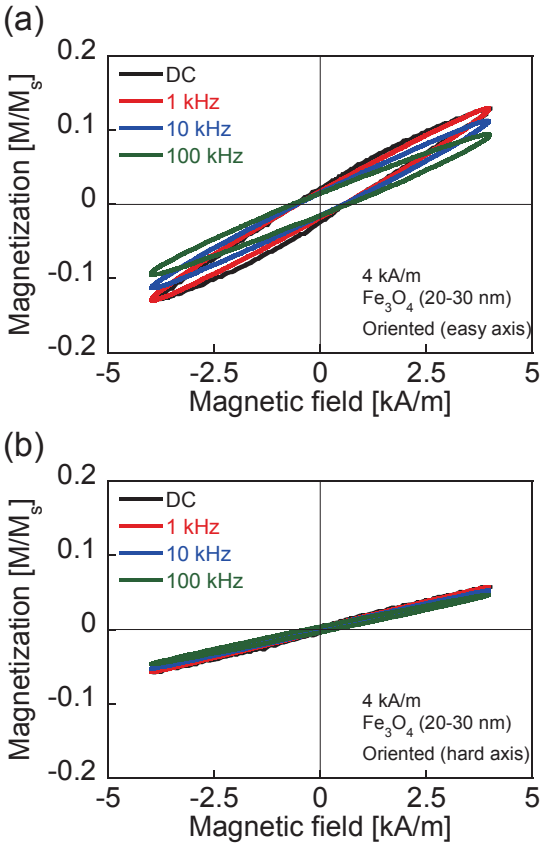

Fig. 4 DC and AC magnetization curves of Fe_3O_4 (20–30 nm) nanoparticles at field intensity of 4 kA/m. Direction of applied field was along (a) easy axis and (b) hard axis.

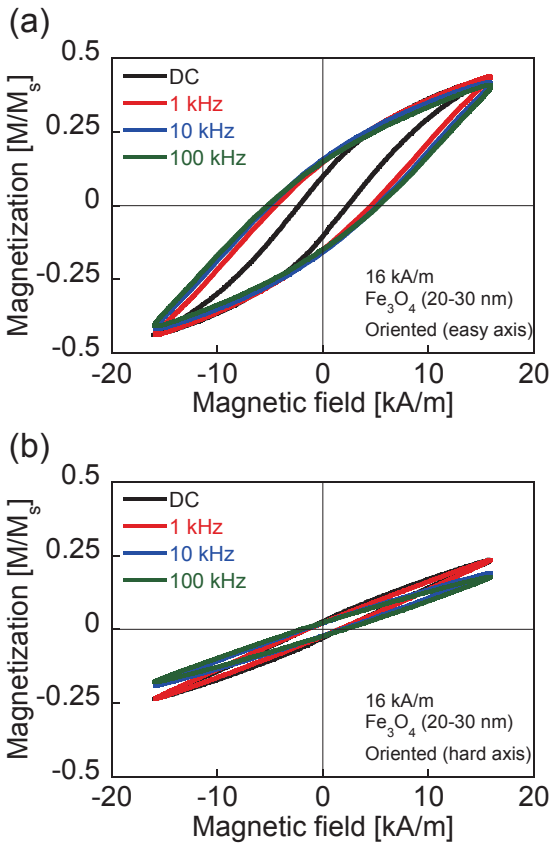

Fig. 5 DC and AC magnetization curves of Fe_3O_4 (20–30 nm) nanoparticles at field intensity of 16 kA/m. Direction of applied field was along (a) easy axis and (b) hard axis.

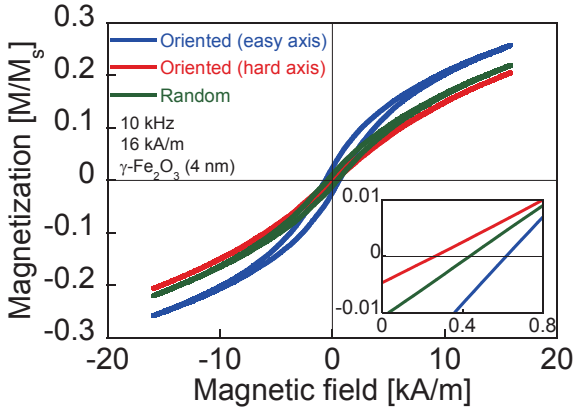

Fig. 6 AC magnetization curves of γ-Fe_2O_3 (4 nm) nanoparticles at frequency of 10 kHz. Intensity of field was 16 kA/m.

greater in the easy axis sample than in the randomly oriented sample. However, there are some particles whose magnetization is opposite to the applied field in the easy axis sample owing to the strong binding force associated with the large anisotropy energy barrier. In the hard axis sample, the maximal value of the distribution is observed at approximately ±0.2 M/M_S. This indicates that the magnetic moments are predominantly aligned along the easy axis rather than magnetization reversal.

The DC and AC magnetization curves of the γ-Fe_2O_3 (4 nm) nanoparticles at frequencies of 1–100 kHz and intensity of 16 kA/m are shown in Fig. 8. In Fig. 8 (a), the coercivity of the easy axis sample clearly increases with increasing frequency. In contrast, the coercivity of the hard axis sample is marginal up to 100 kHz, as shown in Fig. 8 (b). According to the results of numerical simulations (Fig. 7), magnetic relaxation occurs with a large delay relative to the applied AC magnetic field in the easy axis sample. In contrast, magnetic reversal does not occur in the AC field with the oscillation of the magnetic moment on the easy axis in the hard axis sample. Thus, hysteresis is not observed in the magnetization curves of the hard axis sample even at high frequencies. This manifests an experimental observation of the fast Néel relaxation process.

The magnetization (M/M_S) under the applied field of 16 kA/m during the magnetization reversal at 100 kHz was calculated by summation of distributed magnetization shown in Fig. 7. The magnetizations of random, easy axis, and hard axis samples were derived as 0.21, 0.30, and 0.11 M/M_S from Figs. 7(a), (b), and (c), respectively. The calculated values of magnetizations of easy axis and hard axis samples were compared with the measured magnetization shown in Fig. 8. As indicated by the arrows in the figure, the measured magnetization under the applied field of 16 kA/m at 100 kHz were 0.25 and 0.20 M/M_S for the easy axis and hard axis samples, respectively. The difference between 0.25

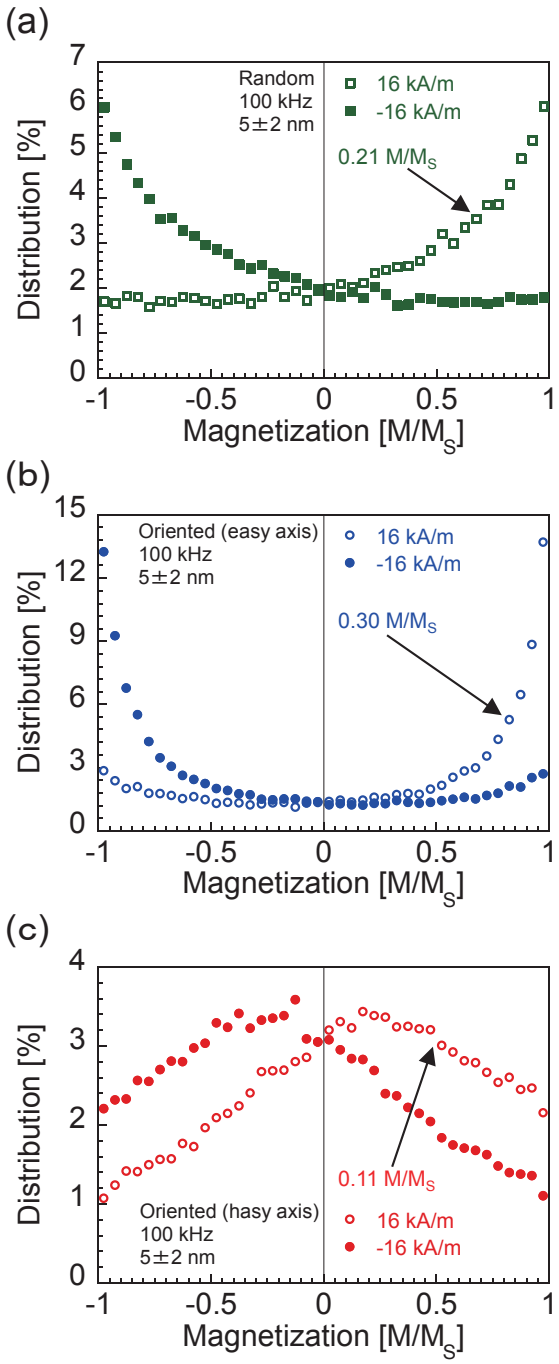

Fig. 7 Calculated results for distribution of number of particles when magnetic field was applied to (a) random sample, (b) easy axis sample, and (c) hard axis sample.

and 0.20 M/M_S is smaller than that between calculated values of 0. 30 and 0.11 M/M_S, which can be explained by imperfection of particle orientation in the prepared samples. In spite of this quantitative analysis, the simulated magnetization agreed well qualitatively with the measured AC magnetization curves in terms of characterization of difference in the easy axis and hard axis samples.

Figure 9 compares the AC magnetization curves of

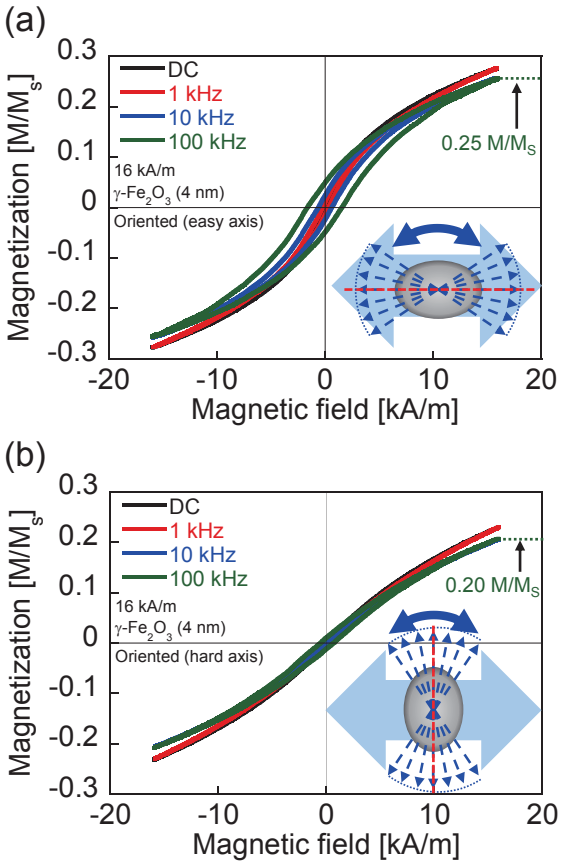

Fig. 8 DC and AC magnetization curves of γ-Fe_2O_3 (4 nm) at frequencies of 1–100 kHz and intensity of 16 kA/m with model of magnetic moment distribution. Direction of applied field was along (a) easy axis and (b) hard axis.

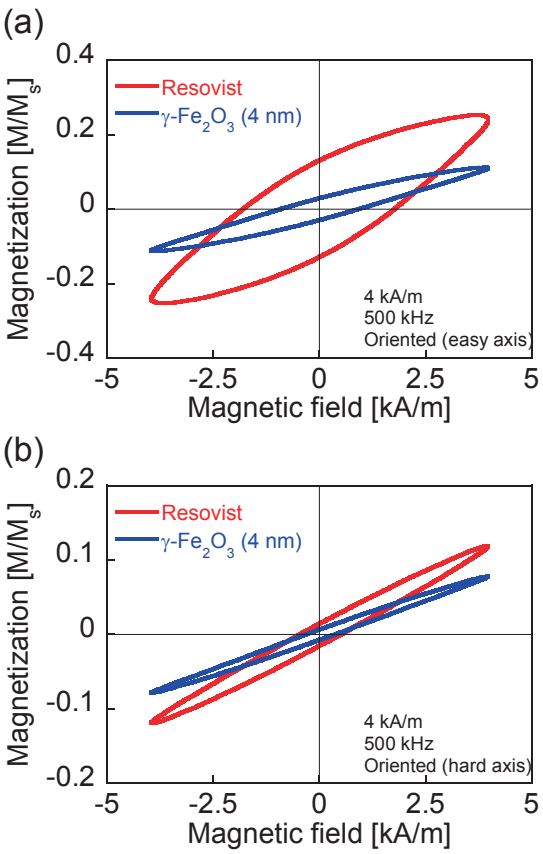

Fig. 9 AC magnetization curves of γ-Fe_2O_3 (4 nm) nanoparticles and Resovist® at field intensity of 4 kA/m and frequency of 500 kHz. Direction of applied field was along (a) easy axis and (b) hard axis.

the γ-Fe_2O_3 (4 nm) nanoparticles with those of Resovist® at a field intensity of 4 kA/m and frequency of 500 kHz. The core size distribution of Resovist® has been estimated by Yoshida *et al.*, and the size distribution of 6.1–21.6 nm has been reported[14]. Thus, the particles of large diameters with longer Néel relaxation time than that of γ-Fe_2O_3 (4 nm) exhibit large coercivity in both the easy axis and the hard axis samples.

4 Conclusions

In this study, samples of immobilized particles of γ-Fe_2O_3 (d_c = 4 nm), Fe_3O_4 (d_c = 20–30 nm), and Resovist®, whose easy axes were aligned or randomly oriented, were prepared. Their DC and AC magnetization properties up to 500 kHz were analyzed, and the effect of easy axis orientation on superparamagnetic nanoparticles and ferromagnetic nanoparticles was evaluated. In both superparamagnetic γ-Fe_2O_3 (d_c = 4 nm) and ferromagnetic Fe_3O_4 (d_c = 20–30 nm) nanoparticles, the DC and AC magnetization curves indicated larger and smaller magnetization due to anisotropy energy, when the field was applied to the easy axis and hard axis of the samples, respectively. The increase of magnetization under an applied AC field along the easy axis is expected to increase the harmonic signal in MPI. In the case of γ-Fe_2O_3 (4 nm) nanoparticles, the superparamagnetic feature was clearly observed with random orientation of the easy axis, regardless of the alignment of immobilized particles. In the AC magnetization curves of the γ-Fe_2O_3 (4 nm) nanoparticles, there was an increase in coercivity with increasing field frequency applied to the easy axis direction. In contrast, when the field was applied to the hard axis, the coercivity was almost marginal up to 100 kHz so that magnetization could follow the applied magnetic field even at high frequency. Thus, the fast magnetization process of Néel relaxation was experimentally observed. The AC magnetization curve of Resovist®, measured at a frequency of 500 kHz, indicated larger coercivity than that of the γ-Fe_2O_3 (4 nm) nanoparticles. This is because Resovist® has a longer Néel relaxation time owing to the larger core size of the particles compared to γ-Fe_2O_3 (4 nm). The frequency characteristics and effect of core size distribution of MNPs both in the easy axis and hard axis

directions were clearly revealed.

In addition, numeric simulation using the LLG equation was performed to understand magnetization distribution of individual MNPs, and the results agreed well qualitatively with the experimental results. The calculated results successfully demonstrated that a large proportion of magnetization was reversed by the application of an AC field to the easy axis and that there remained particles whose magnetization direction was opposite to the applied field owing to the strong binding force associated with the large anisotropy energy barrier. When the AC field was applied to the hard axis, the magnetization, which was predominantly aligned to the easy axis, was oscillated by the applied field.

Acknowledgments The authors wish to acknowledge Dr. Takashi Yoshida at Kyushu University for his advice in numerical simulation. This work was partially supported by the JSPS KAKENHI Grant Number 15H05764, 17H03275, and 17K14693.

References

1) Q. A. Pankhurst, N. K. T. Thanh, S. K. Jones, and J. Dobson: *J. Phys. D Appl. Phys.*, **42**, 224001–224015 (2009).
2) B. Gleich and J. Weizenecker: *Nature*, **435**, 1214–1217 (2005).
3) E. Y. Yu, M. Bishop, B. Zheng, R. M. Ferguson, A. P. Khandhar, S. J. Kemp, K. M. Krishnan, P. W. Goodwill, and S. M. Conolly: *Nano Letters*, **17**, 1648–1654 (2017).
4) T. Yoshida, T. Sasayama, and K. Enpuku: *Int. J. Magn. Part. Imaging*, **3**, 1703002 (2017).
5) S. Ota, R. Takeda, T. Yamada, I. Kato, S. Nohara, and Y. Takemura: *Int. J. Magn. Part. Imaging*, **3**, 1703003 (2017).
6) H. Mamiya and B. Jeyadevan: *Sci. Rep.*, **1**, 157 (2011).
7) T. Yoshida, S. Bai, A. Hirokawa, K. Tanabe, and K. Enpuku: *J. Magn. Magn. Mater.*, **380**, 105–110 (2015).
8) S. Ota and Y. Takemura: *Appl. Phys. Express*, **10**, 085001 (2017).
9) T. Yoshida, Y. Matsugi, N. Tsujimura, T. Sasayama, K. Enpuku, T. Viereck, M. Schilling, and F. Ludwig: *J. Magn. Magn. Mater.*, **427**, 162 (2017).
10) E. C. Stoner and E. P. Wohlfarth: *Philos. Trans. R. Soc. London. Ser.* A, **240**, 599–642 (1948).
11) L. Néel: *Ann. Geophys.*, **5**, 99 (1949).
12) W. F. Brown, Jr.: *Phys. Rev.*, **130**, 1677 (1963).
13) X. L. Liu, Y. Yang, C. T. Ng, L. Y. Zhao, Y. Zhang, B. H. Bay, H. M. Fan, and J. Ding: *Adv. Mater.*, **27**, 1939–1944 (2015).
14) T. Yoshida, N. B. Othman, and K. Enpuku: *J. Appl. Phys.*, **114**, 173908 (2013).
15) H. Kobayashi, A. Hirukawa, A. Tomitaka, T. Yamada, M. Jeun, S. Bae, and Y. Takemura: *J. Appl. Phys.*, **107**, 09B322 (2010).
16) W. T. Coffey, and Y. P. Kalmykov: *J. Appl. Phys.*, **112**, 121301 (2012).
17) R. E. Rosensweig: *J. Magn. Magn. Mater.*, **252** 370–374 (2002).
18) S. A. Shah, D. B. Reeves, R. M. Ferguson, J. B. Weaver, and K. M. Krishnan: *Phys. Rev. B*, **92**, 094438 (2015).
19) N. A. Usov: *J. Appl. Phys.*, **107**, 123909 (2010).
20) K. Simeonidis, M. P. Morales, M. Marciello, M. Angelakeris, P. de la Presa, A. Lazaro–Carrillo, A. Tabero, A. Villanueva, O. Chubykalo–Fesenko, and D. Serantes: *Sci. Rep.*, **6**, 38382 (2016).

Received Oct. 13, 2017; Accepted Jan. 18, 2018

Journal of the Magnetics Society of Japan

Vol. 42 No. 2 (通巻第 296 号) 2018 年 3 月 1 日発行

Vol. 42 No. 2 Published Mar. 1, 2018
by the Magnetics Society of Japan
Tokyo YWCA building Rm207, 1–8–11 Kanda surugadai, Chiyoda-ku, Tokyo 101–0062
Tel. +81–3–5281–0106 Fax. +81–3–5281–0107

Printed by JP Corporation Co., Ltd.
2–3–36, Minamikase, Saiwai-ku, Kanagawa 212–0055
Advertising agency: Kagaku Gijutsu-sha

発行：（公社）日本磁気学会 101–0062 東京都千代田区神田駿河台 1–8–11 東京YWCA会館 207 号室
製作：ジェイピーコーポレーション 212–0055 神奈川県川崎市幸区南加瀬 2–3–36 Tel.（044）571–5815
広告取扱い：科学技術社 111–0052 東京都台東区柳橋 2–10–8 武田ビル 4F Tel.（03）5809–1132